



DISSERTATION

Validation of Monte Carlo physics models for application in radiotherapy

ausgeführt zum Zwecke der Erlangung des akademischen Grades
eines Doktors der technischen Wissenschaften
unter der Leitung von

Em. Univ.Prof. O. Univ.Prof. Dipl.-Ing. Dr.techn. Hannes Aiginger
E141
Atominstitut der Österreichischen Universitäten

eingereicht an der
Technischen Universität Wien
Fakultät für Physik
von

Dipl.-Ing. Anton Lechner
Matrikelnummer: 0025263
Mankerstrasse 5, 3232 Bischofstetten

Wien, am 21. Dezember 2011

Diese Arbeit wurde vom österreichischen Bundesministerium für Wissenschaft und Forschung (BMWf) und dem CERN unterstützt.

Abstract

Steady advances in radiotherapy treatment modalities simultaneously yield a demand for more accurate dose calculation techniques. Owing to the stochastic nature of particle interactions, transport problems can naturally be addressed by means of Monte Carlo methods. Monte Carlo simulations represent one of the most rigorous modalities to obtain spatial fluence and dose distributions accompanying the penetration of particles into matter. General-purpose Monte Carlo packages have gained an increasing importance in medical physics simulations. One such Monte Carlo code system is Geant4 – a versatile toolkit for simulating the coupled transport of a large variety of particles. The toolkit is developed by an international collaboration under participation of CERN.

This thesis presents a comprehensive and detailed examination of Geant4 physics algorithms pertinent to radiotherapy simulations. Available physics options are partly extended. The accuracy of Monte Carlo models embedded in Geant4 is assessed by means of a series of radiation transport benchmarks covering different aspects of electron and ion transport.

A significant part of the thesis is dedicated to the validation of electron condensed history algorithms. Monte Carlo predictions are systematically benchmarked against experimental data reported in the literature, including dose distributions, backscatter coefficients, energy albedos, as well as angular distributions of electrons backscattered from solid targets. Obtained simulation predictions are evaluated for their ability to describe the variation of experimental data with kinetic energy, angle of incidence, and atomic number of materials. Energies relevant to applications in radiotherapy are covered. Different multiple scattering and energy loss models are compared and their accuracy and limitations are discussed.

Complementing the electron transport studies, the thesis addresses light-ion transport in matter. Physics options in Geant4 are extended by incorporating a parameterization model, based on ICRU 73 stopping powers, to describe the electronic energy loss of ions. With particular attention paid to the recent developments, the accuracy of current Geant4 models is examined

for simulating dose profiles of ^{12}C ions in phantom materials. Obtained distributions are validated against experimental data available in the literature. A quantitative analysis is performed addressing the precision of the Bragg peak position and proportional features of dose distributions. In addition, the effect of different generators for ion fragmentation on dose profiles is evaluated.

Kurzfassung

Die stetigen Fortschritte in der Strahlentherapie und fortwährende Verbesserungen in den damit verbundenen Behandlungsmethoden führen gleichzeitig zu einer gesteigerten Nachfrage nach genaueren Verfahren zur Dosisberechnung. Strahlentransportrechnungen können aufgrund des stochastischen Charakters der Wechselwirkungen von Teilchen mit Materie auf natürliche Art und Weise mittels der Monte Carlo-Methode beschrieben werden. Derartige Strahlentransportsimulationen stellen eines der genauesten Verfahren zur Bestimmung räumlicher Fluenz- und Dosisverteilungen dar. Insbesondere nehmen Monte Carlo-gestützte Allzweckcodes eine immer wichtigere Stellung in der medizinischen Physik ein. Ein derartiger Simulationscode ist Geant4, welcher von einer internationalen Kollaboration unter Teilnahme des CERN entwickelt wird. Geant4 ist ein vielseitiges Programm zur Simulation der Wechselwirkung und des Transports von Teilchen in Materie.

In der vorliegenden Arbeit werden, in umfangreichen und detaillierten Ausmaß und mit Hauptaugenmerk auf Anwendungen in der Strahlentherapie, Transportmodelle des Geant4-Simulationsprogrammes untersucht. Vorhandene Wechselwirkungsmodelle werden zum Teil erweitert. Um die Genauigkeit von Simulationsalgorithmen zu bestimmen, wird eine Reihe von Vergleichstests durchgeführt, wobei verschiedene Aspekte hinsichtlich des Transports von Elektronen und Ionen behandelt werden.

Ein signifikanter Teil der Arbeit beschäftigt sich mit der Untersuchung von “condensed-history”-Algorithmen zur Beschreibung von Elektronenwechselwirkungen mit Materie. Monte Carlo-Berechnungen werden auf systematische Art und Weise mit experimentellen Daten aus der Literatur verglichen, wobei verschiedene physikalische Größen wie Dosisverteilungen, Rückstreuoeffizienten sowie Winkelverteilungen von rückgestreuten Elektronen untersucht werden. Die Vergleiche umfassen jenen Energiebereich, welcher für Anwendungen in der Strahlentherapie von Relevanz ist. Im Zuge der Benchmark-Tests wird das Vermögen der Transportmodelle untersucht, die Abhängigkeit experimenteller Größen von der Elektronenenergie, dem Einfallswinkel sowie von der Kernladungszahl des Absorbermaterials wiederzu-

geben. Verschiedene Modelle zur Beschreibung der Vielfachstreuung sowie zur Berechnung des Energieverlusts werden miteinander verglichen und die Genauigkeit und Anwendbarkeit der Modelle wird diskutiert.

Ergänzend zu den obigen Untersuchungen werden Betrachtungen zu Ionen-transportsimulationen angestellt. Im Zuge dieser werden in Geant4 verfügbare Algorithmen um ein parametrisiertes Modell zur Beschreibung des Energieverlusts von Ionen in Materie erweitert. Die Parametrisierungen beruhen auf im ICRU-Bericht 73 publizierten Werten des Ionenbremsvermögens. Des weiteren wird, unter besonderer Berücksichtigung der neuesten Entwicklungen, die Genauigkeit von Ionen-transportmodellen zur Dosisberechnung untersucht. Simulierte Dosisprofile von Kohlenstoffionen in Phantommaterialien werden mit experimentellen Daten aus der Literatur verglichen. Als Teil der Modellvalidierung wird eine quantitative Analyse hinsichtlich der Genauigkeit der berechneten Kurven, insbesondere bezüglich der Position des Bragg-Peaks und der Halbwertsbreite, durchgeführt. Zusätzlich werden verschiedene Fragmentierungsmodelle und deren Auswirkungen auf Dosisprofile untersucht.

Contents

Abstract	iii
Kurzfassung	v
1 Introduction	1
1.1 Monte Carlo-based dosimetry	1
1.2 Scope of this thesis	3
2 Monte Carlo simulations in radiotherapy	5
2.1 Concepts of Monte Carlo-based particle transport	7
2.1.1 The analogue particle transport scheme	8
2.1.2 The condensed particle transport scheme	12
2.2 Electron and photon transport simulations	16
2.2.1 Radiotherapy applications	17
2.2.2 Common general-purpose Monte Carlo codes: coupled electron/photon transport systems	19
2.3 Hadron and ion transport simulations	21
2.3.1 Applications in particle therapy	23
2.3.2 Common general-purpose Monte Carlo codes: hadron and ion transport systems	23
3 Transport methods and models in Geant4	27
3.1 Particle transport	27
3.2 Physics models	30
3.2.1 Electromagnetic interactions	30
3.2.2 Hadronic interactions	32
4 Comparative study of electron dose distributions in solid tar- gets	35
4.1 Previous studies and outline	36
4.2 Materials and methods	36

4.2.1	Experimental data	36
4.2.2	Monte Carlo simulation	37
4.2.3	Transport parameter settings	40
4.3	Results and discussion	41
4.3.1	Comparison of different Geant4 versions and transport parameter configurations	41
4.3.2	Evaluation of the simulation accuracy with different physics models	48
4.3.3	Comparison of data at 30° and 60° electron beam in- cidence	55
4.4	Conclusions	56
5	Simulation benchmark of electron backscattering from solid targets	59
5.1	Previous studies and outline	60
5.2	Materials and methods	61
5.2.1	Experimental data	61
5.2.2	Monte Carlo simulation	63
5.2.3	Secondary particle production	65
5.2.4	Transport parameter settings	65
5.2.5	Bremsstrahlung correction	66
5.3	Results and discussion	67
5.3.1	Backscattering of electrons with energies between 0.1 and 1 MeV	68
5.3.2	Backscattering of electrons with energies between 3 and 14 MeV	71
5.4	Conclusions	74
6	Validation study of ion dose distributions in phantom mate- rials	75
6.1	Introductory aspects, previous studies and outline	76
6.2	Electronic energy loss of ions	77
6.2.1	Geant4 “Standard” stopping power algorithms	77
6.2.2	Implementation of a new parameterization model	78
6.2.3	Stopping powers in the literature and their use in Geant4	80
6.2.4	The <i>I</i> -value of water and revised ICRU 73 tables	81
6.3	Materials and methods	82
6.3.1	Experimental depth-dose profiles	82
6.3.2	Monte Carlo simulation	84
6.3.3	Secondary electron production and stepping limitation	88
6.3.4	Normalization of dose profiles	88

6.4	Results and discussion	89
6.4.1	Carbon ion Bragg peak in water	89
6.4.2	Carbon ion Bragg peak in polyethylene	96
6.5	Conclusions	101
7	Summary and conclusions	103
	Appendix	105
A.1	Geant4 material data	105
	Bibliography	107
	Acknowledgements	133
	Curriculum vitae	135

Chapter 1

Introduction

Radiotherapy is the curative or palliative treatment of malignant or, in less frequent cases, other diseases by means of ionizing radiation [1]. As a cancer treatment modality – often applied concurrently with surgery and chemotherapy [2] – it has the advantage of being a non-invasive method to control or even eradicate tumours. Recent estimates [2, 3] suggest that a treatment with ionizing radiation would be beneficial to more than half of all cancer patients. In radiotherapy, one generally aims in maximising the tumour control probability with the least level of normal-tissue morbidity [4]. This is usually achieved by selectively delivering a high radiation dose to malignant cells while concurrently preventing high exposure of adjacent and distant healthy tissues [1]. The accurate planning and delivery of tumour dose is a highly complex task. In clinical practice, the uncertainty of tumour and normal-tissue dose cumulatively results from different sources like patient set-up, organ motion, calibration of the therapy unit, and dose calculations [5, 6]. To optimize the clinical outcome, treatment procedures require a precise dose administration due to strongly varying dose–effect relationships [5, 6, and references therein]. As reported by Papanikolaou et al. [5], clinical studies with electron and photon beams showed that a 7% difference in dose can lead to observable effects with regard to both, tumour remission and normal-tissue response.

1.1 Monte Carlo-based dosimetry

In the last decades, significant progress in radiotherapy has been achieved through the advent of highly conformal treatment modalities, such as intensity-modulated x-ray therapy [7] or proton and ion beam irradiation [8–11]. The advances in delivery techniques and the concurrent gain in clinical efficacy

are closely intertwined with the invention and maturation of other key technologies, in particular three-dimensional anatomical [12] and biological [13] imaging techniques, accelerator designs [14, 15], and radiobiology. The overall improvement of radiotherapy treatment methodologies concurrently yields a demand for more accurate dose calculation techniques [5, 16]. Currently, calculated dose values are recommended to have an uncertainty of less than a few percent. A challenging aspect of dose calculations is the accurate description of perturbation effects resulting from particle scattering in heterogeneous media and the formation of secondary particle fields. Many efforts have been dedicated to the development of more sophisticated, computer-aided dose algorithms [16, 17]. Among these, Monte Carlo radiation transport simulations are one of the most rigorous modalities to calculate spatial dose and fluence distributions accompanying the penetration of particles into matter. Such simulations are generally considered a suitable means for dosimetry in radiotherapy (see, for example, [4, 6, 18–21]).

The Monte Carlo method is a statistical technique, using random number sequences to obtain an estimate of a physical or mathematical quantity under study [22]. The propagation of particles in media, being inherently probabilistic in its nature, can naturally be addressed by means of Monte Carlo methods. The invention of computer-based Monte Carlo sampling dates back to neutron diffusion studies by John von Neumann and Stanislaw Ulam in the 1940s [23]. Based on stochastic models describing particle interactions with absorber atoms, Monte Carlo transport simulations generate sequences of individual trajectories, aiming to describe phenomena associated with the behaviour of a large number of tracks. A limiting factor is the intrinsic statistical uncertainty, often necessitating lengthy computation times, however rapid advances in computing technology, both in hardware and software, have led to a steady increase of Monte Carlo-based applications [24]. Nowadays, Monte Carlo codes represent a powerful tool in medical dosimetry, with great potential to accurately compute three-dimensional energy deposition pattern in heterogeneous media and to describe the mixed radiation fields produced as a result of particle interaction with beam-shaping devices, monitoring systems, and human tissues or tissue-equivalent phantoms alike. Monte Carlo codes are employed in a variety of use cases, ranging from beam-machine interaction studies and hardware design to quality assurance and dose verifications.

General-purpose Monte Carlo packages have gained an increasing importance in medical physics simulations. One such Monte Carlo code system is Geant4 [25, 26] – a versatile, object-oriented toolkit for simulating the coupled transport of a large variety of particles such as photons, electrons, positrons, hadrons, and ions. The simulation package accounts for electro-

magnetic and nuclear interactions particles experience along their track [25]. It covers a broad energy range, from a few hundred electronvolt to the high-energy regime of interest for accelerator or cosmic ray physics [25]. In particular, the Geant4 code system offers a comprehensive set of physics models with recourse to both, theoretical and data-driven approaches [25–27]. Since its initial production release in 1998, Geant4 has been developed and extended by an international collaboration formed by research centers, national institutes and universities, with new toolkit versions being delivered in a semiannual release cycle [25]. The code system is applied in a diversity of fields, spanning from high-energy physics [27] to experimental nuclear physics [28], space science [29, 30], and medical physics [18, 19, 31–33].

1.2 Scope of this thesis

In view of the high level of accuracy pursued in medical dosimetry, it is an important prerequisite to assess the ability of Monte Carlo simulation models to yield a reliable and accurate prediction of relevant physical quantities. This thesis presents a comprehensive and systematic evaluation of Monte Carlo algorithms in Geant4, covering different aspects of particle transport pertinent to medical dosimetry. In part, existing modelling approaches are extended. A brief outlook is given below. The work presented in this thesis was performed at the European Organization for Nuclear Research (CERN). In particular, presented results emerge from research activities conducted within the Geant4 Collaboration.

A significant part of the thesis is dedicated to electron transport in matter. Describing the propagation of electrons, independently if they are primary particles or secondary products, is of considerable importance in medical dosimetry. Electrons are produced by kilovoltage and megavoltage x-ray beams used in diagnostic medicine and radiotherapy; they are employed in external beam therapy for the treatment of superficial diseases; they form secondary components in proton and ion therapy; and they are emitted by radioisotopes adopted in brachytherapy or targeted radionuclide therapy. Monte Carlo codes employed in electron transport problems commonly adopt the condensed history technique [34], where sets of successive interaction events are summarized by means of multiple collision theories. The incentive for condensed history simulations lies in the very nature of charged particle interactions, effectively rendering single scattering schemes inefficient for many applications involving fast electrons either as primaries or secondaries [35]. This thesis presents a comprehensive validation of Geant4 condensed history electron transport algorithms, addressing particle energies

typically encountered in radiotherapy applications. Monte Carlo predictions are systematically benchmarked against experimental data reported in the literature, including dose distributions, backscatter coefficients, energy albedos as well as angular distributions of electrons backscattered from solid targets. Obtained simulation predictions are evaluated for their ability to describe the variation of experimental data with beam energy, angle of incidence, and atomic number of target samples. Different multiple scattering and energy loss models are compared and their accuracy and limitations are discussed.

Complementing the electron transport studies, the thesis addresses light-ion transport in matter. Physics options in Geant4 are extended by incorporating a parameterization model, based on ICRU 73 [36] stopping powers, to describe the electronic energy loss of ions. For a few materials, revised ICRU 73 stopping power tables recently published by Sigmund et al. [37] were included, also affecting media like water which are of importance in radiotherapeutical applications. With particular attention paid to the recent developments, the accuracy of current Geant4 models is examined for simulating Bragg peak profiles of ^{12}C ions incident on phantom materials. Simulated dose distributions are validated against experimental data available in the literature, where the focus is on beam energies relevant to ion therapy applications (90–400 MeV/u). A quantitative analysis is performed which addresses the precision of the Bragg peak position and proportional features of the dose distribution. In addition, the effect of different generators for ion fragmentation on dose profiles is evaluated.

The thesis is organized as follows. Chapter 2 presents concepts of Monte Carlo-based transport schemes and reviews common applications of Monte Carlo simulations in radiotherapy. Chapter 3 provides a brief overview of the Geant4 toolkit, discussing transport methods and physics models included in the simulation package. Chapters 4 and 5 are dedicated to the validation of electron transport algorithms, respectively covering spatial dose distributions and backscattering phenomena. Chapter 6 presents the integration of ICRU 73 stopping powers into Geant4 and presents corresponding validation studies. Finally, Chapter 7 gives a summary of the thesis as well as concluding remarks.

Chapter 2

Monte Carlo simulations in radiotherapy

Monte Carlo radiation transport simulations are based on sequences of random samples drawn from probability distribution functions (PDFs) which characterize particle interactions with matter. In this way, by creating random tracks, Monte Carlo simulations emulate the stochastic nature of particle propagation in media and allow to describe accompanying transport phenomena. Owing to the explicit modelling of physical processes of individual particles, Monte Carlo transport schemes inherently account for local scattering characteristics, i.e. they adapt naturally to varying geometry and material properties along the particle's path, and, in addition, they enable the production (and subsequent transport) of secondary particles. The natural way of describing radiation transport, including the generation of particle cascades, renders Monte Carlo simulations a powerful tool for particle physics and radiation dosimetry [38]. The potential to improve accuracy, largely due to full three-dimensional transport capabilities, was a major incentive to employ Monte Carlo simulations in medical disciplines. Particularly in complex scenarios, where particles travel in heterogeneous media or across material boundaries, the strength of Monte Carlo simulations becomes evident [6, 16, 18, 21, 38].

In the last decades, Monte Carlo code systems have gained an increasing importance in external photon [18, 19, 21] and electron [18, 20, 21] beam radiotherapy, brachytherapy [39], diagnostic radiology and therapeutic [31] and diagnostic [40, 41] nuclear medicine. More recently, Monte Carlo simulations have also become a fundamental tool for newer treatment modalities involving beams of heavy, charged particles like protons or ions. In a review paper on Monte Carlo simulations in medical physics, Rogers [24] pointed out that the number of Monte Carlo-related publications in two major medical

physics journals (“Medical Physics” and “Physics in Medicine and Biology”) has doubled every 5 years from 1967 to 2000. Apart from being used as an approach to radiation transport, the Monte Carlo technique has been extensively applied to miscellaneous physical or mathematical problems in medical, biomedical and other health-related disciplines. It is interesting to note that a search for “Monte Carlo” in the PubMed [42] database of the US National Library of Medicine (NLM) currently (November 2011) yields 29 559 articles, compared to the 14 452 hits reported by Rogers [24] in early 2006.

The Monte Carlo method is, as indicated above, a stochastic technique and results are obtained by averaging scores, i.e. values of a random variable, over a large number of simulated particle tracks. In this way, the expected value of the random variable, which can be equivalent to a macroscopic physical quantity like fluence or dose, is estimated by the sample mean [43]. According to the Central Limit Theorem (CLT) [44], the rate of convergence is proportional to $1/\sqrt{N}$ as $N \rightarrow \infty$, where N indicates the number of histories [21] (in Monte Carlo terminology, a history encompasses a primary particle trajectory and all secondary trajectories resulting from induced particle cascades [45]). Although being an accurate tool for radiation dosimetry, larger-scale Monte Carlo simulations have long been unfeasible due to the lengthy execution times needed to cope with inherent statistical uncertainties. Owing to the advances in computing technology and due to the development of more user-friendly software packages, Monte Carlo codes are increasingly used in more complex medical use cases [18, 21, 24]. Examples are the simulation of electron or photon transport through detailed models of linear accelerator treatment heads [19, 20], or the transport of protons through entire beam lines including nozzles of passive scatter therapy units (see, e.g., Refs. [46, 47]); in particular, Monte Carlo codes are also employed for accompanying dose calculations in patient voxel geometries imported from computed tomography (CT) images (see, for instance, the Refs. [18, 21, 47]). Modern general-purpose Monte Carlo packages, often emerging from other domains like reactor physics or high energy physics, play a significant role in the evolution of Monte Carlo particle transport simulations in medical physics, and most research studies are based upon such code systems (cf. Refs. [19, 20, 24, 31, 48]).

In this chapter, concepts of Monte Carlo-based transport simulations are briefly outlined (Section 2.1) and an overview of Monte Carlo applications and their benefits in radiotherapy is given, focusing separately on electron/photon transport problems (Section 2.2) and on hadron and ion transport simulations (Section 2.3). The two latter sections also provide an overview of general-purpose Monte Carlo codes most commonly used in

radiotherapeutical applications.

2.1 Concepts of Monte Carlo-based particle transport

Monte Carlo particle transport simulations involve the sequential generation of random particle trajectories based on physical interaction models and the simultaneous calculation of relevant quantities by averaging the contributions from individual tracks. The elemental ingredients of Monte Carlo code systems are (loosely based on Zaidi and Sgouros [31], Pawlicki and Ma [45]): (i) a (pseudo-)random number generator (random number generation is generally based on deterministic methods and obtained numbers are therefore pseudo-random [49]), (ii) algorithms producing a set of primary particles and primary vertices, (iii) stochastic models describing physical mechanisms of particle interactions with matter, (iv) algorithms enabling the navigation of particles in the tracking geometry, and (v) scoring methods allowing to record relevant physical quantities and the associated statistical uncertainty. In general, the simulation of a single track proceeds by determining the primary particle type and initial properties, like energy, position and momentum direction, and, secondly, by propagating the particle through matter. The tracking is based on random variables sampled from the PDFs describing the occurrence and final state of physical interactions, i.e. energy loss and angular deflection of incoming particles as well as type, initial energy and direction of secondaries [50].

A straightforward approach to the simulation of particle transport is the analogue Monte Carlo scheme (cf. [21, 35, 38, 50–52]), where individual interactions are explicitly accounted for. Such an approach is suitable if the interaction probability is reasonably small [50, 51]. In general, the analogue scheme is applied to the Monte Carlo transport of photons and neutrons [43]. It is also employed in microdosimetry simulations of charged and neutral particles, where individual track structures can be important. However, the very nature of electromagnetic interactions which charged particles experience along their track renders analogue schemes inefficient for most applications involving fast charged projectiles [35]. As often discussed in the literature, this gave incentive to the invention of the condensed history technique [34], where charged particle encounters are clustered such that the simulation mimics only the net effect along macroscopic track segments.

This section presents basic concepts of Monte Carlo particle transport simulations, focusing on aspects related to the simulation of physical inter-

actions and the resulting random walk: the principles of analogue (Section 2.1.1) and condensed (Section 2.1.2) transport schemes are briefly discussed, however without referring to specific interaction laws or their mathematical description. It is beyond the scope of the current section to describe details of random number generation and sampling methods. For more information, particularly concerning common sampling techniques like the inverse-transform, composition and rejection methods, the reader is referred to references like the book of Rubinstein and Kroese [49]. Additional aspects specifically related to Monte Carlo-based radiation transport may also be found in the Refs. [41, 52–54].

Besides the generation of particle tracks, an essential element of Monte Carlo transport simulations is the retrieval of information, i.e. the calculation of physical quantities and associated standard deviations (or variances). Probabilistic aspects related to this topic are common to many problems addressed by statistical methods. Basic definitions and theorems, like the previously mentioned Central Limit Theorem, are discussed in a range of publications (see, e.g., the book of James [55] or the review paper of James [22]) and are not repeated here. Further, it is out of the scope of this section to give a description of variance reduction techniques. For more information on this topic, the reader is referred to references like [21, 54].

2.1.1 The analogue particle transport scheme

The analogue Monte Carlo transport technique, commonly also known as discrete, detailed or microscopic Monte Carlo simulation, models individual particle interactions in sequential order. In this sense, by following each interaction event, the analogue technique provides – as results converge to the estimate of the expectation value – an exact solution to the transport equation [35, 51, 56]. Analogue schemes are therefore a rigorous rendering of nature within established physical principles guiding interactions of particles with matter [21, 35].

A particle penetrating into a medium may interact through different, competing mechanisms with atoms or molecules composing the material. Photons, for example, can be subject to coherent and Compton scattering processes, pair production and photoelectric and photonuclear effects. The probability that a particle interacts through a mechanism of type k is determined by the corresponding cross section σ_k , which generally depends on the particle energy E and the absorber atom or molecule species [43]. The dimension of cross sections is equal to an area, commonly expressed in terms of barns ($1 \text{ barn} = 10^{-24} \text{ cm}^2$) [54]. Assuming the projectile survives an interaction, the energy loss $\varepsilon = E - E'$ and the angular deflection Ω suffered by

the particle in the physical process are governed by the respective differential cross section (DCS),

$$\frac{d^2\sigma_k}{d\varepsilon d\Omega}(E; \varepsilon, \Omega). \quad (2.1)$$

The deflection angle is commonly expressed as $\Omega = (\theta, \phi)$, where θ and ϕ are the polar and azimuthal angle relative to the incident direction. Depending on the type of process, cross sections may not always be available in closed analytical form. Hence, for some interaction mechanisms, Monte Carlo simulations incorporate numerical tabulations. A typical example are neutron reaction cross sections from the ENDF/B-VI evaluated data library [57] used in several major Monte Carlo codes.

For particles propagating in a homogeneous material composed of a single atom or molecule species, the mean free path between two interactions of type k is given by [43]

$$\lambda_k(E) = \frac{1}{\mathcal{N}\sigma_k(E)}, \quad (2.2)$$

where \mathcal{N} represents the number of atoms or molecules per volume, i.e. $\mathcal{N} = \rho N_A/M$, with ρ being the material density, N_A the Avogadro constant ($6.022045 \times 10^{23} \text{ mole}^{-1}$), and M the molar mass of atoms or molecules, respectively. The denominator, $\mathcal{N}\sigma_k(E)$, is generally referred to as the macroscopic cross section Σ_k of a particle [58]. Conversely, σ_k is called the microscopic cross section [43]. Supposing the particle undergoes different processes, the mean free between any type of interaction is

$$\lambda(E) = \frac{1}{\mathcal{N}\sum_k \sigma_k(E)}, \quad (2.3)$$

where the index k accounts for all types of processes.

The random walk of a particle propagating in an infinite, homogeneous medium can be described in two steps, which are successively repeated until the particle is absorbed (in flight) or has lost all its energy (alternatively, a projectile may be disregarded if its energy falls below a defined threshold, often called *tracking cut*). The basics of this transport scheme are outlined below. For simplicity, no particular attention is given to the creation process of the projectile and no specific assumption is made concerning the particle type. Between two interactions the particle is assumed to travel with constant energy along a straight line segment. Starting from an arbitrary interaction point on the particle's trajectory, the analogue Monte Carlo transport proceeds as follows:

- (i) **Sampling the spatial distance to the next interaction** The first step consists of transporting the projectile along a path length s to

the next point of interaction. The distance to the next interaction is determined by the smallest of different path lengths s individually calculated for each competing process. The path length imposed by an interaction mechanism k is determined as follows:

- (a) Assuming the previous interaction was due to a process of type k , then s is randomly sampled. It can be shown that the path length to the next interaction event of the same type is distributed according to [43]

$$p(s) = \frac{1}{\lambda_k} \exp\left(-\frac{s}{\lambda_k}\right), \quad (2.4)$$

where λ_k is the mean free path defined in (2.2). The distance s can then be determined from the cumulative distribution function of $p(s)$,

$$P(s) = \int_0^s p(s') ds', \quad (2.5)$$

by using the inverse transform method (also called direct method). This method implies that, if ξ is a random number uniformly distributed between 0 and 1, $s = P^{-1}(\xi)$ is a path length randomly distributed according to the probability distribution $p(s)$ [58]. Inverting the cumulative distribution $P(s)$ leads to the following relation [43]:

$$s = -\lambda_k \log(\xi - 1). \quad (2.6)$$

- (b) If, in the previous event, the particle was not subject to a process of type k , the path length corresponding to the interaction mechanism k is updated according to

$$s = s' - s_{prev}, \quad (2.7)$$

where s' is the path length previously prescribed by the process k , and s_{prev} is the actual path length of previous step.

Once path lengths were determined for all competing interaction mechanisms by means of the expressions (2.6) and (2.7), the shortest path length s is selected, and the particle is transported along its initial direction, i.e. along the direction resulting from the previous interaction event.

- (ii) **Final state calculation** The second step encompasses the sampling of the final state of the projectile interaction. If the particle was not absorbed in the process, changes in energy and direction are determined from the DCS (see (2.1)) corresponding to the process k , which dictated

the step length. The DCS serves, after being normalized, as the joint probability distribution $p_k(\varepsilon, \Omega)$ with respect to the variables ε and Ω . As discussed by Bielajew [54], a common procedure is to sample first the energy loss from the marginal probability distribution of ε ,

$$p_k(\varepsilon) = \int p_k(\varepsilon, \Omega) d\Omega, \quad (2.8)$$

and, as a second step, to determine the angular deflection from the conditional probability distribution function of Ω given the obtained ε ,

$$p_k(\Omega|\varepsilon) = p_k(\varepsilon, \Omega)/p(\varepsilon). \quad (2.9)$$

Once energy and deflection were sampled, the transport continues with step (i).

It should be emphasized that the transport scheme described above presents only the essentials of analogue Monte Carlo simulations. Some aspects like the generation of secondary particles were neglected. In particular, the calculation of step (ii) can rest upon sophisticated final state models (e.g. event generators used in the description of nuclear collisions). Moreover, the tracking of particles becomes more complex if they penetrate into heterogeneous media. In this case, the spatial variation of the mean free path needs to be taken into account, and hence the probability distribution of s in (2.4) becomes [43, 54]

$$p(s) = \frac{1}{\lambda_k} \exp\left(-\int_0^s ds'/\lambda_k(s')\right). \quad (2.10)$$

Applying the inverse transform method and reformulating the sampling equation gives (cf. Equation 2.6) [54]

$$\int_0^s ds'/\lambda_k(s') = -\log(\xi - 1). \quad (2.11)$$

This demonstrates that s cannot be determined analytically in all cases. To account for absorber heterogeneities, some Monte Carlo codes adopt an altered sampling procedure [25, 59, 60], based on the number of mean free paths

$$n_{\lambda_k} = \int_0^s ds'/\lambda_k(s'). \quad (2.12)$$

Assuming the particle travels in an absorber of piecewise constant composition and density, the path length can then be calculated as $s = \lambda_{0k} n_{\lambda_k}$,

where λ_{0_k} is the mean free path of the layer currently containing the particle and n_{λ_k} is sampled according to

$$n_{\lambda_k} = -\log(\xi - 1). \quad (2.13)$$

If the particle reaches a boundary, s is recalculated using the mean free path λ_{1_k} of the consecutive absorber slab, i.e. $s = \lambda_{1_k} n_{\lambda_k}$. This procedure exploits the fact that n_{λ_k} is independent of the specific absorber. More details about Monte Carlo transport in heterogeneous media can be found, for example, in references like [43, 54].

As a final remark, it is emphasized that the outlined two-step scheme is not a unique approach to execute analogue Monte Carlo simulations. In particular, strategies of selecting the type of interaction can vary among Monte Carlo code systems.

2.1.2 The condensed particle transport scheme

Describing the transport of charged particles, independently if they are primary projectiles or secondary products, is of considerable importance in clinical dosimetry. This includes, for example, the tracking of electrons produced by kilovoltage or megavoltage x-ray beams, or the transport of primary protons and ions as well as accompanying charged fragments in particle therapy. However, the large number of interaction events energetic charged particles experience along their tracks (e.g. elastic Coulomb scattering, ionization and Bremsstrahlung processes) demands other techniques than analogue ones [35, 38] (it must be emphasized that nuclear processes of charged hadrons and ions are much less likely and are hence not affected by this restriction).

The publication of Berger [34], which introduces the concept of condensed history simulations, is generally considered as the foundation of the modern Monte Carlo transport. Berger describes charged particle propagation by summarizing the effect of a large, but finite number of inelastic and elastic collisions in a final state considering net changes in particle energy, momentum direction and lateral displacement. This means, in the condensed approach the transport technique does no longer mimic all individual particle collision events as described in the previous section, but treats sets of events as a new entity in particle tracking (hence, in Monte Carlo terminology, charged particle “steps” are usually condensed steps). As a direct consequence, a significant decrease in execution time can be achieved as particles can be followed with fewer, condensed steps.

The condensed approach has several implications on Monte Carlo simulations. For example, the description of particle transport is based on multiple

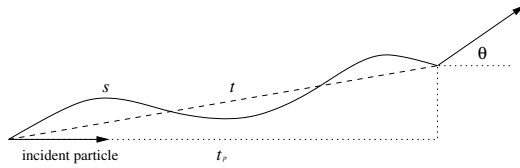


Figure 2.1: Condensed history step, including multiple scattering angle θ , curved path length s , straight line step length t , and the projection of t onto the direction of the incoming particle. Reproduced from Ref. [61].

collision models [52], which introduce, in contrast to the analogue scheme, some approximations to Monte Carlo transport simulations. Due to their physical nature, one generally treats elastic scattering and energy loss processes independently from each other:

- **Elastic scattering.** As a consequence of condensed particle transport the geometrical size of a simulation step differs from the actual path length s . The correlation between the straight line step size t and the length of the curved path is usually referred to as *path length correction*, which is given by [61, 62]

$$t_p = \int_0^s \langle \cos \theta(s') \rangle ds', \quad (2.14)$$

where t_p is the projection of t on the axis representing the initial direction of the particle, and θ is the multiple scattering angle (see Fig. 2.1). Path length corrections as well as the net angular deflection and the net lateral displacement along condensed steps need to be modelled by means of according multiple scattering (MSC) theories, taking into account the correlation between the different quantities.

Monte Carlo codes often employ multiple scattering angular distributions by Molière [63] and Goudsmit and Saunderson [64, 65]. Molière's distribution is valid in the approximation of small scattering angles, whereas the Goudsmit-Saunderson theory also applies to large-angle scattering. Longitudinal and lateral spatial distributions and their correlation with the multiple scattering angle generally vary amongst Monte Carlo code systems [35]. As shown by Kawrakow and Bielajew [35], different codes reproduce the exact first and second order spatial moments (derived by Lewis [62] from the transport equation) and the spatial-angular correlation to a varying degree of accuracy.

In the proximity of absorber boundaries, conditions for the applicability of multiple scattering theory break down [54]. Monte Carlo codes therefore often adopt a single scattering scheme if the particle propagates near boundaries.

- **Energy loss.** The cumulative energy loss suffered along a condensed history step can be obtained by calculating the average value $\langle \varepsilon \rangle$ and, secondly, by superimposing fluctuations, which account for the stochastic nature of energy loss events.

For a process k , the mean rate of energy loss or *stopping power*¹ is given by [60, 67]

$$S_k(E) = \mathcal{N} \int_0^{\varepsilon_{max}} \varepsilon \frac{d\sigma_k}{d\varepsilon}(E; \varepsilon) d\varepsilon, \quad (2.15)$$

where \mathcal{N} represents, as above, the number of atoms or molecules per unit volume, $d\sigma_k/d\varepsilon$ is the differential cross section for an energy transfer ε to a secondary in an inelastic interaction, and ε_{max} is the maximum energy transferable to a secondary in a single interaction event. The total stopping power results from the sum over all contributing processes, i.e.

$$S(E) = \sum_k S_k(E). \quad (2.16)$$

The average energy loss $\langle \varepsilon \rangle$ along a condensed step of path length s can then be obtained by

$$\langle \varepsilon \rangle = E(R) - E(R - s) \quad (2.17)$$

where $E(R)$ is the inverse function of

$$R(E) = \int_0^E \frac{1}{S(E')} dE'. \quad (2.18)$$

Above expression describes the particle range in continuous slowing down approximation (CSDA), which assumes a non-stochastic energy loss during particle penetration into matter.

Stochastic aspects of energy loss are described by means of *straggling functions* $f(s, \varepsilon)$. Straggling functions are often based on Landau and

¹Controversy exists [66] as to whether stopping power is an adequate nomenclature for a quantity having the dimension of a force. Despite this, the designation stopping power is well established in the scientific community and is hence used throughout this work.

Vavilov distributions or, for sufficiently long path lengths s , on Gaussian distributions.

In condensed Monte Carlo particle transport, the emission of secondaries (electrons, photons) is usually restricted to those particles having energies above a defined threshold T_{cut} . Secondary electrons with a kinetic energy exceeding T_{cut} are usually referred to as *knock-on* electrons or δ -electrons (see e.g. [52]). The energy transferred in sub-threshold collisions is then treated as local energy deposition. Secondary particle emission, and its direct impact on the primary particle's dynamic state, also gives rise to distinguish between Monte Carlo algorithms [21]. As often described in the literature (see, for example, [18, 21, 52]), it was Berger [34] who introduced the basic concept of categorizing condensed transport schemes. Code systems are referred to as Class I codes if primaries are propagated within a selected step size grid; at the same time, secondary particle emission is treated separately from the primary particle transport, i.e. changes in the state of primary particles due to secondary particle production are modelled in a stochastic manner (e.g. by means of straggling functions), but no interrelation between changes in the primary's state and the initial state of secondaries exists on a step-by-step basis [18, 21, 52]. In contrast, transport codes are Class II codes if the transport algorithm considers an explicit correlation between a projectile's final state and the initial properties of generated secondaries at each step [18, 21, 52]. In Class II codes the alteration of a primary particle's state along a step is therefore twofold, i.e. consisting of a *continuous* part considering the condensed transport and a *discrete* part simulating the analogue effects of secondary generation above T_{cut} [38, 52, 67]. The discrete collisions are often called *catastrophic* events, whereas sub-threshold interactions are commonly referred to as *soft* collisions (see, for example, Refs. [38, 52, 54]). Evidently, the impact of the different parts is guided by the production threshold. The discrete part generally follows a similar transport scheme as described in the previous section, where the probability of a catastrophic interaction of type k (see Equations (2.2) and (2.10)) is determined by the following cross section [67]:

$$\sigma_k(E, T_{cut}) = \int_{T_{cut}}^{\varepsilon_{max}} \frac{d\sigma_k}{d\varepsilon}(E; \varepsilon) d\varepsilon. \quad (2.19)$$

Here, ε_{max} denotes again the maximum energy that can be transferred to a secondary in a single collision, T_{cut} is the lower production cut, and $d\sigma_k/d\varepsilon$ is the DCS described above (in the case, k represents target ionization, the binding energy of electrons is, for simplicity, assumed to be much smaller than ε and is hence neglected in the current formulation). By treating catastrophic

interactions in an analogue manner, Class II codes interrupt, in contrast to Class I schemes, a primary particle’s path at real collision points. A conceptual constraint arises, however, from the fact that the energy of projectiles cannot be considered constant between two catastrophic collisions due to the accompanying continuous energy loss [54]. Hence, the corresponding variation of the cross section in (2.19) along path segments needs to be taken into account. Beyond that, a Class II step proceeds as follows: If, based on the cross section in (2.19), a step is limited by a process of type k , a secondary is created and its initial kinetic energy and momentum is considered in the energy/momentum balance of the projectile. Conversely, the mean energy loss of the projectile due to soft collisions along the path is derived from *restricted stopping powers*

$$S_k(E, T_{cut}) = \mathcal{N} \int_0^{T_{cut}} \varepsilon \frac{d\sigma_k}{d\varepsilon}(E; \varepsilon) d\varepsilon, \quad (2.20)$$

where, in contrast to Equation (2.15), the upper integration limit is T_{cut} . Similarly, the straggling function, which now models sub-threshold energy loss fluctuations, explicitly depends on T_{cut} .

2.2 Electron and photon transport simulations

Photons, as they penetrate into matter, produce secondary electrons and may be converted into electron–positron pairs (at photon energies >1.022 MeV). Conversely, electrons and positrons impart energy to secondary electrons in ionization processes and create Bremsstrahlung photons in the electric field of nuclei. In addition, photons are emitted when positron–electron annihilation occurs. Beyond that, induced shell vacancies can give rise to relaxation radiation. These physical interactions cause a coupling of electron and photon fields, where, depending on energy and material, certain processes can dominate secondary particle production. Monte Carlo transport methods outlined in the previous section are particularly suitable to provide a quantitative description of such cascade developments.

In particular, Monte Carlo simulations allow to describe certain aspects of coupled electron/photon transport² and their impact on particle fluences and spatial dose distributions, which are difficult to incorporate in deterministic dose algorithms. As outlined by Fraass et al. [6], this includes, for example, electron/photon field perturbations due to varying scattering characteristics

²Positrons are not explicitly mentioned as their transport is similar to those of electrons.

in heterogeneous materials; the absence of electronic equilibrium at interfaces of media with largely differing properties (partly due to electron backscatter); and the occurrence of lateral electronic disequilibrium for photon fields with small field size, particularly in low-density media. The consideration of such effects can be crucial for calculations related to machine–beam interaction or transport in tissues.

As a consequence, the Monte Carlo technique is widely used to address electron and photon transport problems in medical physics, especially coupled electron/photon applications. A brief overview of the use of corresponding Monte Carlo simulations in radiotherapy, as well as a summary of common general-purpose Monte Carlo packages, is presented in the following. It is however out of the scope of this section to give a complete discussion of the topic; instead, applications in radiotherapy are highlighted by means of a few illustrative examples. Where available, topical review articles are cited as a source of further information.

2.2.1 Radiotherapy applications

Early review articles, discussing therapy-related electron/photon Monte Carlo transport problems of the pre-1990s, were published by Raeside [53] and Andreo [52]. Since then, electron/photon Monte Carlo-based applications strongly evolved concurrently with technological advances in treatment modalities like external x-ray and electron therapy, brachytherapy, and targeted radionuclide therapy.

External photon and electron beam therapy Monte Carlo radiation transport techniques have been used extensively to study clinical beams from linear accelerator therapy units, in particular for the examination of photon and electron field interaction with treatment machine heads. The corresponding literature was summarized in dedicated review articles [19, 20]. Based on detailed treatment head models, Monte Carlo simulations enable the description of different aspects of clinical irradiation procedures, like Bremsstrahlung generation (for x-ray therapy), field interaction with monitor chambers and beam-shaping devices (e.g. wedges, multi-leaf collimators), and the production of contaminant particle fields [19, 20]. As a consequence, Monte Carlo-based beam phase space distributions commonly serve, together with Monte Carlo pre-calculated dose kernels, as input for conventional treatment planning (TP) algorithms employed in external beam radiotherapy [17, 68]. A literature review further demonstrates (see, for example, the Refs. [69–72]) the role of Monte Carlo generated data as widely established dosimetric reference in the verification of conventional TP software. As such, Monte

Carlo codes have become an important quality assurance (QA) tool [45], for example, in the verification of monitor unit calculations for IMRT treatment planning (see, e.g., the Refs. [73, 74]). In recent years, first steps have been made to explicitly incorporate the Monte Carlo technique into TP systems [18, 21, 24]. In particular, commercial solutions based on specialized Monte Carlo codes have become available for both, photon and electron beam radiotherapy (see, for example, Table 2 in Ref. [18]). Currently, such Monte Carlo dose engines do however not fully replace conventional dose algorithms in the entire planning process. A comprehensive summary, addressing the current status of Monte Carlo treatment planning (MCTP) in external beam radiotherapy, may be found in the review articles by Reynaert et al. [18] and Chetty et al. [21]. A more compact overview of MCTP is available in the publication of Spezi and Lewis [48].

Brachytherapy Besides external beam radiotherapy, electron/photon Monte Carlo simulations are commonly employed in other treatment modalities like brachytherapy. Widely adopted dosimetry protocols [75–77] of the American Association of Physicists in Medicine (AAPM) and the European Society for Therapeutic Radiology and Oncology (ESTRO) recognize Monte Carlo transport techniques as reference methods to obtain consensus datasets for the clinical application of photon-emitting brachytherapy sources. Following these recommendations, a vast amount of literature has been published (see, e.g., the Refs. [78–83] and citations in [76, 77]) describing both, low- and high-energy brachytherapy source models, by means of Monte Carlo-based dosimetry data. Such Monte Carlo studies often disregard electrons as their transport is only relevant in the absence of electronic equilibrium, like in the proximity of the source, and in the case of β -electron emissions with sufficient energy to penetrate the source capsules (see, e.g., Ref. [84]). Monte Carlo transport methods are also used for various other aspects relevant to brachytherapy, like applicator design [85], radiation shielding calculations [86], or the dosimetric evaluation of new candidate radioisotopes [87]. Similarly as for external beam therapy, Monte Carlo-based techniques are considered a viable option in brachytherapy treatment planning [88, 89]. Monte Carlo dose algorithms allow to incorporate effects (e.g. inter- and intrasource attenuation, impact of high- Z shields, heterogeneous scattering characteristics due to the individual human anatomy) neglected by the current brachytherapy standard TP formalism [39, 88–90]. Specialized Monte Carlo-based systems for brachytherapy treatment planning have been presented in the literature (see citations in Ref. [89]), however no commercial MCTP software is currently available [88].

Targeted radionuclide therapy Nuclear medicine was among the first medical domains experiencing a trend towards Monte Carlo-based dosimetry [31, 52, 53]. Electron/photon Monte Carlo systems have been used for various aspects in associated fields like targeted radionuclide therapy; examples are the examination of radionuclide mixtures for disseminated malignancy [91], the calculation of point dose kernels for β -emitters (see, e.g., Refs. [92, 93]), and patient-specific treatment planning [94]. A comprehensive summary of therapy-related Monte Carlo simulations in nuclear medicine can be found in the book of Zaidi and Sgouros [31].

Diagnostic medicine Like in radiotherapy, Monte Carlo-based dosimetry is also of significant interest in diagnostic disciplines, particularly nuclear imaging. For more information on this topic, the reader is referred to references like [40, 41].

2.2.2 Common general-purpose Monte Carlo codes: coupled electron/photon transport systems

Monte Carlo particle transport systems commonly used in medical physics can broadly be categorized into a) general-purpose codes and b) codes specifically developed for application in Monte Carlo treatment planning [18, 21, 24, 48, 88]. Some Monte Carlo systems of the first category originate from other physics domains (e.g. nuclear physics, high-energy physics), but provide accurate electron and photon transport capabilities and have consequently been exploited in radiotherapy studies. In contrast, the development of codes of category b) was primarily driven by the need to cope with time constraints in patient treatment planning. Such codes, which appeared more recently than general-purpose Monte Carlo software, typically apply sophisticated variance reduction techniques and their tracking mechanisms are often optimized for particle transport in CT-based voxel geometries which requires efficient scoring and boundary crossing algorithms [18, 21]. General-purpose codes are primarily, but not exclusively, used in less time-critical applications. They play, however, a significant role in medical dosimetry, from basic research to treatment head output calculations and quality assurance. The current section briefly summarizes general-purpose Monte Carlo code systems widely used for coupled electron/photon transport problems in radiotherapy; overviews of such codes were also given in several previous publications [18, 21, 31]. Descriptions of specialized medical physics codes for TP can be found elsewhere [18, 21, 24, 48, 88].

The electron/photon transport packages most commonly employed in

Code	Description	Affiliated Institution(s)	First release	Latest version ^a (release date)
EGS:	Coupled electron/photon transport code, applicable at kinetic energies above a few keV. Electron transport follows a Class II condensed history scheme. The EGS4/PRESTA variant improved electron transport with respect to the original EGS4 release. EGSnrc builds on EGS4, introducing, for example, new electron elastic scattering and stepping features. EGS5 is based on EGS4; it adopts, for instance, the random hinge method [51], however excludes PRESTA.	NRCC and SLAC	1985 (EGS4)	V4-2.3.1 (EGSnrc,
EGS4 [59, 61]			2000 (EGSnrc)	2010) ^b egs5-1.0.4
EGSnrc [95, 96]			2005 (EGS5)	(EGS5, 2010) ^c
EGS5 [97]				
Geant4 [25, 26]	Object-oriented toolkit for simulating the coupled transport of photons, leptons, hadrons and ions in matter. Dedicated low-energy physics package included. Electron and photon physics algorithms are applicable above 250 eV. Employs a Class II scheme, using an original multiple scattering algorithm. Simulation code for coupled photon/electron/neutron transport in matter. Electron transport algorithms are largely based on the ITS 3.0 code. Ionization is modelled in a Class I scheme; in contrast, Bremsstrahlung production follows a Class II scheme.	CERN, ESA, Fermilab, HIP, IN2P3, INFN, KEK, Lebedev Institute, LIP, SLAC, TRIUMF, and UK/STFC LANL	1998	9.3 (2009) ^d
MCNP:	Simulation code for coupled photon/electron/neutron transport in matter. Electron transport algorithms are largely based on the ITS 3.0 code. Ionization is modelled in a Class I scheme; in contrast, Bremsstrahlung production follows a Class II scheme.	Universitat de Barcelona and Universitat Politècnica de Catalunya	1977	5.1.40 (2005) ^e
MCNP4 [98]				
MCNP5 [99]				
PENELOPE [56, 58, 100]	Code for coupled electron/photon transport simulations in matter. Applicable at energies between a few hundred eV and 1 GeV. Adopts a mixed Class II algorithm, which treats hard collision events in a detailed scheme. Applies random hinge [51] transport mechanics.		1996	2008.1 (2009) ^f

Table 2.1: General-purpose Monte Carlo code systems (in alphabetical order) commonly employed for coupled electron/photon transport problems in radiotherapy. The description primarily outlines details on code-specific electron transport methods.

^aAs of July 2010. Beta releases are not considered.

^bSource: <http://irs.inms.nrc.ca/software/egsnrc/>

^cSource: <http://rcwww.kek.jp/research/egs/egs5.html>

^dSource: <http://geant4.web.cern.ch/geant4/>

^eSource: <http://mcnp-green.lanl.gov/>

^fSource: <http://www.nea.fr/tools/abstract/abstract/detail/nea-1525>

medical applications are the Class II condensed history codes EGSnrc [95, 96] and its predecessor EGS4 [59], as well as the EGS4/PRESTA variant [61] (EGS is an acronym for Electron Gamma Shower). EGSnrc incorporates sophisticated electron scattering and stepping algorithms and is considered one of the most accurate codes for electron transport problems, in particular ionization chamber simulations [24]. EGS4 was the first version of the EGS high-energy Monte Carlo code family extending physics models down to the low keV region. With the introduction of PRESTA (Parameter Reduced Electron-Step Transport Algorithm), the low-energy behaviour of the EGS4 condensed history scheme was improved [61]. A new EGS version, EGS5 [97], was released more recently. Another Monte Carlo system often applied in radiotherapy is the coupled neutron/photon/electron transport code MCNP (acronym for Monte Carlo N-Particle) [98, 99], originally developed for nuclear physics simulations. Electron transport capabilities were introduced with version MCNP4 [98] of the simulation package. The electron physics algorithms in MCNP4 and its successor MCNP5 [99] are largely adopted from the Integrated TIGER Series (ITS) code system [101]. MCNP uses a Class I scheme for ionization processes and a Class II scheme for Bremsstrahlung production. Another modern, general-purpose Monte Carlo package is the previously mentioned Geant4 toolkit (GEANT stands for GEometry ANd Tracking) [25, 26], which includes physics algorithms for a large range of particles; it applies a Class II scheme to describe charged particle transport (a more detailed review of physics options in Geant4 is presented in Chapter 3). Like EGS, Geant4 has its roots in high-energy physics. Further, a modern electron/photon transport code is PENELOPE (PENetration and Energy LOSS of Positrons and Electrons) [56, 58, 100], which employs a Class II transport scheme. In contrast to most other Monte Carlo packages, PENELOPE incorporates a mixed scattering scheme, which enables a discrete treatment of hard elastic collision events. A summary of all mentioned Monte Carlo code systems is presented in Table 2.1. Although partly outdated, a detailed overview of electron/photon algorithms implemented in the different codes can be found in the paper of Verhaegen and Seuntjens [19]. Recent physics options are generally described in reference papers or manuals like [25, 58, 59, 96, 98, 99, 102, and citations therein].

2.3 Hadron and ion transport simulations

When traversing matter, hadrons and ions encounter elastic and inelastic nuclear interactions. Inelastic processes can induce secondary particle cascades eventually leading to the formation of mixed radiation fields. Radiother-

apy proton beams, for example, produce recoil nuclei as well as secondary protons, neutrons and, less frequently, other light fragments. The complexity of beam–absorber interactions increases for ions due to the possibility of projectile fragmentation. Inelastic nucleus–nucleus interactions yield diversified spectra of secondary nuclear species, protons and neutrons, which contaminate the incident ion beam. Apart from nuclear collisions, protons and ions are subject to Coulomb scattering off target nuclei and they experience energy losses due to interaction with electrons bound to absorber atoms, culminating in an abrupt stopping of particles at low energies.

Accurate dosimetry in particle therapy relies on the quantitative assessment of cascade development, as naturally delivered by Monte Carlo transport methods. Besides that, Monte Carlo techniques allow one to account for other peculiarities of proton and ion transport such as the alteration and dispersion of particle ranges due to absorber heterogeneities. Owing to the elevated dose delivery prior to particle stopping, accurate range calculations are critical to the clinical outcome of proton and ion therapy. Similarly, particle field perturbations beyond material inhomogeneities can significantly impact the dose delivery. It is generally acknowledged [4, 103] that Monte Carlo transport methods are currently the only algorithms allowing a detailed account of hadron and ion processes, resulting cascades, fluence perturbations and induced dose distributions in heterogeneous media, particularly in the vicinity of hard-edged material boundaries.

Different hadron and ion Monte Carlo transport codes, many of them originating from the high-energy physics environment [104], are available in the public domain. Similarly as the electron Monte Carlo systems described in the previous section, these codes adopt condensed history transport schemes to describe Coulomb interactions of charged hadrons and ions. Nuclear interactions are handled in an analogue manner. In the energy regime relevant to radiotherapy, the Monte Carlo codes typically adopt multi-phase approaches to describe the dynamical evolution of inelastic hadron–nucleus and nucleus–nucleus collisions: in this modelling scheme, the initial stages are generally handled by means of intra-nuclear cascade (INC) and pre-equilibrium models or, alternatively, by using a quantum molecular dynamics (QMD)-based approach. The final stage of the reaction treats the de-excitation of remaining nuclei by means of according fragment and gamma emissions. Some Monte Carlo transport systems are coupled with external nuclear event generators to handle such interactions.

A brief overview of typical Monte Carlo applications in proton and ion therapy is given in the following. The section is then concluded by a summary of the most common hadron and ion Monte Carlo code systems employed in medical physics.

2.3.1 Applications in particle therapy

Proton therapy Monte Carlo transport simulations are widely employed for clinical and research studies in proton therapy. Applications range from the verification of analytical pencil-beam dose algorithms [105–107] to monitor unit calculations (see, e.g., the Refs. [108, 109]) and shielding design (see, for instance, the Refs. [110, 111]). In particular, Monte Carlo codes were used to examine clinically relevant effects resulting from machine–beam interaction, such as patient-dose degradation due to proton collimator scatter [112, 113] or risk of secondary cancer induction due to stray neutrons (see, e.g., the Refs. [114–116]). In other publications, Monte Carlo calculations aided in the analysis of *in-vivo* imaging techniques based upon prompt gamma-ray [117] and positron emission [118, 119]. Monte Carlo transport methods also proved to be a cost-effective technique for hardware design studies [120–122] and the verification of clinical QA procedures [47, 123]. Notably, different authors [123, 124] demonstrated that Monte Carlo simulations are a suitable alternative to measurements for commissioning proton therapy treatment planning systems. In another article, Newhauser et al. [125] used Monte Carlo calculations to prepare a TP system prior to the construction of a proton therapy facility. Such an application demonstrates potential economic aspects behind the use of Monte Carlo simulations. Despite the increasing number of Monte Carlo-related studies, measurements, however, continue to play a major role in hadron therapy.

Ion therapy A review of the pertinent literature also demonstrates the increased attraction Monte Carlo codes have gained in the field of ion therapy in recent years: examples are the simulation of β^+ -activity distributions in tissue-like materials for positron emission tomography (PET) as a means of dose monitoring [126–128], the Monte Carlo-based evaluation of water-to-air stopping power ratios for ionisation chamber dosimetry [129–132], the examination of the dependency of dose and radiation quality on the field size [133], the investigation of biological dose distributions [134], or the Monte Carlo-based prediction of radiochromatic film response [135].

2.3.2 Common general-purpose Monte Carlo codes: hadron and ion transport systems

General-purpose codes are widely dominating Monte Carlo applications in hadrontherapy, although code systems optimized for hadron and ion transport in CT-based patient geometries have been reported in the literature [136–138]. The most common general-purpose Monte Carlo packages used in

medical hadron and ion transport problems are FLUKA [139, 140], Geant4 [25, 26], MCNPX [141], PHITS [142, 143], and SHIELD-HIT [104]. A comprehensive summary of hadron and ion Monte Carlo codes was presented in a paper by Gudowska et al. [104]. The current section attempts to provide a brief overview of general features of the different codes.

FLUKA (acronym for FLUktuierende KAskade) was originally developed as a hadron cascade code for high-energy particle accelerators [139]; currently it supports more than 60 particle species, as well as a range of ions [139]. Like FLUKA, Geant4 enables, as previously mentioned, the tracking of a variety of particle species, including hadrons and ions. In addition to nuclear interaction models already available in its predecessor GEANT3 [60], Geant4 offers a number of alternative final-state models and cross sections applicable at radiotherapy energies (more details are presented in the next chapter). MCNPX is an expansion of the previously mentioned MCNP code; it originates from a fusion of MCNP with the LAHET Code System [141]. In addition to the original MCNP neutron/photon/electron transport features, MCNPX enables the tracking of leptons, hadrons and light ions ($Z \leq 2$), and since the latest release also the transport of ions with $Z > 2$ [146]. Another Monte Carlo package offering hadron and ion transport capabilities is PHITS (Particle and Heavy Ion Transport code System). It simulates electron and photon transport by means of external codes [144] and allows to handle hadrons and both light and heavy ions. A Monte Carlo transport system specifically aiming at proton and ion therapy applications is SHIELD-HIT, which is based on the SHIELD [145] code [104]. Improvements over the original SHIELD package primarily concerned Coulomb interactions [104, 129], however transport of secondary electrons or photons is neglected. An overview of the different Monte Carlo codes is presented in Table 2.2.

Code	Description	Affiliated institution(s)	First release	Latest version ^a (release date)
FLUKA [139, 140] Geant4 [25, 26]	Many-particle transport code. Object-oriented toolkit for simulating the coupled transport of photons, leptons, hadrons and ions in matter (see also Table 2.1). Completely re-designed successor of the GEANT3 [60] high-energy physics code. Significantly extends the capabilities of GEANT3 by offering a variety of alternative electromagnetic and nuclear interaction models. Extension of the MCNP code system (see Table 2.1), following a fusion of MCNP with the LAHET code. In addition to MCNP neutron/photon/electron transport algorithms, MCNPX offers transport capabilities for leptons, hadrons and light ions ($Z \leq 2$), and since the latest release version (2.6.0) also for ions with $Z > 2$.	CERN and INFN CERN, ESA, Fermilab, HIP, IN2P3, INFN, KEK, Lebedev Institute, LIP, SLAC, TRIUMF and UK/STFC LANL	1988 ^b 1998	2008.3c.0 (2009) ^c 9.3 (2009) ^d
MCNPX [141]	General-purpose hadron and ion transport package, based on the NMTC/JAM code. Electron and photon transport is handled by means of EGS5 (see Table 2.1) routines [144]. Variant of the hadron and ion transport code SHIELD [145]. Specifically targets applications in radiotherapy. Neglects secondary electron production and transport.	RIST, KEK, JAEA, and Chalmers University Stockholm University, DKFZ, and Russian Academy of Science	1997 2002 2004	2.6.0 (2008) ^e PHITS2 (2010) ^f SHIELD-HIT07 (2007) ^g

Table 2.2: Monte Carlo code systems (in alphabetical order) commonly applied to hadron transport problems in radiotherapy studies.

^aAs of July 2010. Beta releases are not considered.

^bRelease of 3rd FLUKA generation.

^cSource: <http://www.fluka.org>

^dSource: <http://geant4.web.cern.ch/geant4/>

^eSource: <http://mcnpx.lanl.gov/>

^fPHITS2 currently only available in Japan. Source: <http://phits.jaea.go.jp>

^gSource: <http://www.inr.troitsk.ru/shield/shi-hit-eng.html>

Chapter 3

Transport methods and models in Geant4

Geant4 [25, 26] is a versatile, object-oriented toolkit for simulating the coupled transport of a large variety of particles such as photons, electrons, positrons, hadrons, and ions. The code system is applied in a diversity of fields, spanning from high-energy physics [27] and experimental nuclear physics [28] to space science [29, 30] and, as outlined in the previous chapter, medical physics (see e.g. [18, 19, 31–33]). Geant4 has advanced capabilities for modelling complex, three-dimensional geometrical constructs like beam line components, detectors or voxel phantoms. It also offers functionalities to retrieve and record information describing the detector response; it further includes physics event generators and interfaces to external generators, different user interfaces, and several graphics systems for displaying geometries, particle trajectories and hits in detectors.

This chapter gives a brief overview of transport methods (Section 3.1) and physics models (Section 3.2) governing the tracking of particles in Geant4. The discussions primarily address physics modelling approaches pertinent to radiotherapy applications. For more details on other Geant4 capabilities, in particular concerning geometry modelling, scoring features, or physics models important to other domains, the reader is referred to the relevant literature [25–27].

3.1 Particle transport

General principles of Monte Carlo particle transport methods were presented in Section 2.1. The current section describes Geant4-specific details of the tracking scheme steering the propagation of particles through media. Geant4

employs the two-step transport algorithm described in Section 2.1.1. In contrast to other Monte Carlo code systems like EGS, Geant4 does not apply a tracking cut, i.e. particles are followed until they have lost all their kinetic energy [25]. The two principal step-limiting mechanisms in Geant4 are:

- (i) **Discrete interactions and particle decays** The size of simulation steps is restricted by the occurrence of discrete physical events, i.e. events described in an analogue manner. This includes for example all interactions of photons and neutral particles, nuclear interactions of hadrons and ions, as well as charged particle interactions with secondary emissions above T_{cut} (a special feature of Geant4 is that secondary production thresholds must be specified as a distance, which is converted into a corresponding energy threshold; for secondary electrons, this calculation is based on the CSDA range, while for photons the absorption length is used). Moreover, a step can be limited due to decay. In this case, the mean free path is $\lambda = \gamma v \tau$, where γ represents the relativistic factor $(1 - v^2/c^2)^{-1/2}$, v the particle velocity, and τ the mean life time [25].

To determine the distance to discrete physical events, Geant4 employs a path length sampling equation based on the number of mean free paths n_λ (see Equation (2.13)) [25].

- (ii) **Volume boundaries** Secondly, simulation steps are automatically limited if a particle impings on a volume boundary [25]. This restriction is required due to the material dependency of the mean free path λ (see Equation (2.2)) entering the path length sampling formula.

The step size of charged particles transported within condensed history schemes can be subject to restrictions of different nature and may depend on simulation parameters. In Class II systems like Geant4, the selected production threshold T_{cut} directly affects the mean free path between discrete collisions and hence impacts the sampling of the spatial distance to subsequent ionization and Bremsstrahlung events. On the other hand, condensed history physics algorithms in Geant4 additionally limit charged particle steps by means of non-stochastic criteria [147]. Such restrictions ensure that the simulation maintains a certain level of precision [25, 147]. In particular, different step length limits and stepping options are implemented in energy loss and multiple scattering models [27, 147–149]. Throughout particle tracking, all mechanisms stipulate an upper limit for the step size and the shortest of all prescribed values consequently determines the actual length of a step [25]. In this way, stochastic and non-stochastic criteria are in direct competition to determine segments composing a condensed history particle trajectory

[147]. The different non-stochastic stepping restrictions, applied on top of (i) and (ii), are briefly outlined in the following. The step limits were previously summarized in various publications [147, 150–153], but are repeated here due to their importance in benchmark calculations performed in later chapters:

- (iii) **Multiple scattering** The multiple scattering algorithm enforces a volume and energy-dependent path length limit governed by the model parameter f_r . This parameter, which can assume values in the interval $[0,1]$, limits particle steps to [148, 149]

$$s = f_r \times \max\{\lambda_1(E_b), R_c(E_b)\}, \quad (3.1)$$

where E_b is the kinetic energy of the particle when it entered the current volume, λ_1 is the first transport mean free path, and R_c is given by

$$R_c(E) = \int_0^E S_c^{-1}(E') dE', \quad (3.2)$$

with S_c being the total mean energy loss rate below T_{cut} , i.e. S_c are restricted stopping powers defined in Equation (2.20). The step limit in (3.1) is important for an accurate description of multiple scattering around material interfaces [148, 149].

The multiple scattering algorithm implements a second stepping restriction, which forces charged particles to perform multiple (condensed history) steps within a given volume. Details may be found elsewhere [149].

- (iv) **Continuous energy loss** A complementary step size restriction is imposed by the Geant4 energy loss algorithm, which forces particle steps to become progressively smaller as a charged particle slows down. The restriction is only active if $R_c(E_s)$ lies above a certain threshold ρ_R [25, 27], where R_c is given by Equation (3.2) and E_s is the electron energy at the beginning of the step [27]:

$$s = \begin{cases} \alpha_R R_c(E_s) + \rho_R (1 - \alpha_R) (2 - \rho_R / R_c(E_s)) & R_c(E_s) > \rho_R \\ R_c(E_s) & R_c(E_s) \leq \rho_R. \end{cases} \quad (3.3)$$

Here, $\alpha_R \in [0,1]$ is an empirical parameter. In contrast to (3.1), which is only updated if a particle enters a new volume, Equation (3.3) yields a different limit for each simulation step.

- (v) **User-defined** In addition to path length restrictions outlined above, users can assign a customized maximum step size to particles [25], for instance, to adapt steps to the spatial resolution of detectors.

Another point needing careful attention in Monte Carlo transport is the handling of boundary crossings. As noted in Section 2.1.2, multiple scattering theories generally break down if a particle travels near an interface between different materials. Geant4 therefore allows one to employ a single scattering algorithm in the close proximity of volume boundaries [149]. If activated, single scattering is applied within a distance $skin \times \lambda_{elastic}$ from a volume surface, where $\lambda_{elastic}$ is the mean free path for elastic scattering and $skin$ is an empirical parameter [149].

3.2 Physics models

Physical processes in Geant4 are described by means of algorithms responsible for calculating:

- (i) the step length based on cross sections, the decay time, or other, non-stochastic criteria,
- (ii) the final state of the interaction, i.e. the state of the projectile (if it survives the interaction) as well as the state of generated particles or recoils.

For processes treated in the condensed history scheme, the second item includes the cumulative effect due to interactions experienced by the particle along the step. For a variety of processes, Geant4 offers alternative sets of cross sections and physics models. The following sections briefly introduce electromagnetic and hadronic models relevant for applications in radiotherapy. Some modelling approaches are discussed in more detail in the next chapters.

3.2.1 Electromagnetic interactions

Monte Carlo algorithms in Geant4 cover a wide spectrum of electromagnetic interactions of projectiles with matter, including ionization and Bremsstrahlung processes of charged particles; elastic Coulomb scattering off nuclei; Rayleigh and Compton scattering of photons; the photo-electric effect; electron–positron pair production by photons; electron–positron annihilation into gamma pairs; as well as miscellaneous other processes relevant for high-energy physics applications (e.g. electron–positron pair production by muons) [25]. Corresponding physics models are contained in two distinct packages, respectively called “Standard Electromagnetic” [154] (see also [27] for a recent summary) and “Low-Energy Electromagnetic Package” [155, 156]. Modelling approaches implemented in the first package are

largely (but not exclusively) tailored towards applications at higher energies, whereas the second package offers – as implied by its name – extensions for particle–matter interactions at lower energies [25]. There is however no strict division of energy ranges covered by “Standard” and “Low-Energy” physics models.

Multiple scattering can be described by means of two alternative models, one being based on the semi-empirical formulation by Urbán [148, 149] and the second [157] (available since Geant4 version 9.2) combining the Goudsmit-Saunderson [64, 65] angular distribution with an algorithm by Kawrakow and Bielajew [35] to describe the spatial displacement. The first model is applicable to any charged particle species, whereas the latter model handles electron and positron scattering only. Both simulation models employ the path length restriction defined in (3.1) as well as the boundary crossing algorithm outlined at the end of the previous section. More details on Geant4 multiple scattering algorithms can be found in the publication of Ivanchenko et al. [147].

The “Standard Electromagnetic Package” implements electron and positron energy loss models largely based on stopping powers and sampling algorithms previously adopted in GEANT3 [60]. Similarly, photon interaction cross sections and final state models are based on GEANT3. These models are generally applicable at energies where effects due to the atomic shell structure can be neglected [25]. The “Low-Energy Electromagnetic Package” offers alternative ionization and Bremsstrahlung models [158] based on cross sections of the Evaluated Electron Data Library (EEDL) [159], and alternative photon models [158] based on cross sections and Rayleigh form factors of the Evaluated Photon Data Library 1997 (EPDL97) [160]. In the case of ionization and the photo-electric effect, sampling algorithms are based on cross sections for individual atomic shells. As a third alternative, the “Low-Energy” package contains analytical models [156] originally developed for the PENELOPE [56, 58] Monte Carlo code system. In both packages, sub-threshold energy loss straggling of electrons and positrons is handled by means of a modified version of an algorithm originally developed for GEANT3 [161]. In contrast to “Standard” algorithms, models of the “Low-Energy” package simulate the emission of x-rays and Auger electrons due to atomic shell vacancies. The atomic relaxation module [162] uses data from the LLNL Evaluated Atomic Data Library (EADL) [163].

A (partly outdated) overview of the different Geant4 photon and electron physics models applicable at radiotherapy energies can also be found in the publications of Poon and Verhaegen [150] and Verhaegen and Seuntjens [19]. Detailed evaluations of Geant4-based photon attenuation coefficients, cross sections and stopping powers against reference data or other code systems

were published elsewhere [150, 164, 165].

Besides electron and photon processes, both packages also implement models describing ionization processes of protons and ions [27, 166–168]. At higher energies, the Bethe formula is applied, supplemented by higher-order correction terms, whereas different semi-empirical stopping power parameterizations are employed in the energy region below a few MeV. Stopping powers for ions are scaled from proton or alpha stopping powers by means of an effective charge formula. Both, collisional energy loss straggling and charge exchange straggling is modelled. The simulation package also accounts for nuclear stopping.

3.2.2 Hadronic interactions

The Geant4 “Hadronics Package” contains an abundance of different cross section data sets and final-state models describing hadronic interactions of hadrons and nuclei with nuclei of absorber materials. Some data sets and models are only applicable for a certain energy range and/or target nuclei. It is beyond the scope of the current section to give a complete overview of all algorithms; instead selected physics modelling approaches are discussed, in particular cross sections and models employed in a later chapter.

The default set of cross sections for inelastic nuclear interactions of protons, neutrons, pions and light nuclei (deuterons, tritons and ^4He) is based on the GHEISHA [169] code. Alternatively, the simulation package implements cross section formulae according to Wellisch and Axen [170], Wellisch and Laidlaw (unpublished, mentioned in [25]) and Tripathi et al. [171, 172] for protons, neutrons and light nuclei, respectively. For neutron energies below 20 MeV, point-wise cross section from evaluated data libraries such as ENDF/B-VI [57] are included. The simulation package further offers different cross section for heavier ions, based on parameterizations proposed by Tripathi et al. [173, 174], Shen et al. [175], Kox et al. [176] and Sihver et al. [177].

The most simplistic approach to inelastic final state generation for incident protons, neutrons, pions and light nuclei is implemented in the “Low Energy Parameterized” models, originating from GHEISHA. Alternatively, final states of inelastic proton, neutron and pion interactions can be described by means of different theory-based multi-phase approaches, which handle intranuclear cascade (INC), pre-equilibrium and evaporation stages of the reaction. INC models available in Geant4 include the Geant4 Binary Cascade [178], the Bertini Cascade [179, 180], and the Liège Cascade [181]. For neutrons with energies below 20 MeV, final state generation can be based on evaluated data libraries. Inelastic nucleus–nucleus interactions can be de-

scribed by means of the ion Binary Cascade Model, which is an extension of the above mentioned Binary Cascade to light ions, and a more recent model based on quantum molecular dynamics (QMD) [182].

The de-excitation of excited residual nuclei, which are created in the pre-equilibrium stage of the reaction, are simulated by different approaches: the Fermi break-up model [183]; the generalized evaporation model (GEM) by Furihata [184]; and the statistical multifragmentation model (SMFM) by Bondorf et al. [185]. The de-excitation scheme also accounts for gamma emissions.

Chapter 4

Comparative study of electron dose distributions in solid targets

The accurate description of electron transport in matter is fundamental to a variety of problems in radiotherapy. As discussed in Chapter 2.1, condensed history techniques employed in Monte Carlo simulations inherently introduce some approximations to the treatment of electron transport. The accuracy of transport simulations additionally depends on cross sections and corresponding stopping powers applied in a code system. Validation studies form an important prerequisite for Monte Carlo-based dosimetry, in order to assess the predictive ability of transport simulations and to understand the limits of modelling approaches.

This chapter¹ presents a comprehensive benchmark of Geant4 electron transport calculations against experimental energy distribution measurements available in the literature. The accuracy of Geant4 physics models is examined for a wide range of materials, different electron energies (0.05–1 MeV), and normal and oblique beam incidence. The focus is on elemental targets to study the dependency of simulation predictions on the atomic number Z of

¹The results forming the basis of this chapter were partly published in: A. Lechner, M. G. Pia, M. Sudhakar, Validation of Geant4 Low Energy Electromagnetic Processes Against Precision Measurements of Electron Energy Deposition, *IEEE Trans. Nucl. Sci.* 56 (2009) 398–416; A. Lechner, A. Mantero, M. G. Pia, M. Sudhakar, Validation of Geant4 X-Ray Fluorescence Transitions - Validation of Geant4 electromagnetic models against calorimetry measurements in the energy range up to 1 MeV, in: *IEEE Nuclear Science Symposium Conference Record*, Dresden, Germany, 2008, pp. 2869–2876. Preliminary results were presented in: A. Lechner, M. G. Pia, M. Sudhakar, Validation of Geant4 low energy physics models against electron energy deposition and backscattering data, in: *IEEE Nuclear Science Symposium Conference Record*, Honolulu, HI, 2007, pp. 2001–2007.

materials. Not all materials considered are of primary importance in radiotherapy applications. However, by systematically examining target samples with different Z one may infer general trends concerning the ability of the code system. The energy range discussed in this chapter is important to a variety of problems in radiotherapy-related transport studies, particularly in cases where electrons appear as secondary products. Electron transport at higher energies, i.e. at energies relevant for specific treatment modalities such as external electron beam therapy, is studied in the next chapter as a part of backscattering simulations.

4.1 Previous studies and outline

In this chapter, predictions of Geant4 electron transport calculations are compared against experimental data published by Lockwood et al. [186, 187]. Lockwood et al. conducted a series of high-precision measurements addressing the spatial dose distribution of 0.05–1 MeV electrons in solid targets. These dose distributions can be considered a suitable reference for validating electron transport algorithms; several authors employed portions of these data in the validation of Monte Carlo code systems [188–191]. A small subset of the dose profiles was also used in previous Geant4-based studies by Ivanchenko [192], Carrier et al. [193] and Kadri et al. [194]. This chapter examines the evolution of Geant4 multiple scattering algorithms since the publication of Kadri et al. In addition, the current work significantly extends previous comparisons by systematically examining the accuracy of simulation models across all target materials, electron energies and incident angles covered by Lockwood et al. An accurate scoring setup is implemented in order to avoid systematic errors due to characteristics of the experiment.

The chapter is organized as follows. Section 4.2 presents a brief outline of the experimental configurations and provides a discussion of the benchmark simulations and the employed scoring setup. Section 4.3 presents a comparison of Monte Carlo predictions against measurements, considering different Geant4 versions (8.1.p02 and 9.1/9.1.p03) and alternative energy loss models implemented in the Geant4 “Low-Energy Electromagnetic Package”. A summary and concluding remarks are given in Section 4.4.

4.2 Materials and methods

4.2.1 Experimental data

Lockwood et al. [186, 187] presented calorimetric measurements of the depth-

absorbed dose deposited by 0.05–1.0 MeV electron beams in Be, C, Al, Fe, Cu, Mo, Ta, and U. Most experiments were carried out under normal beam incidence; in a few cases, experimental configurations included beams with incident angles α of 30° and 60°, where α is the angle between the beam axis and the normal to the target surface.

The target assembly of Lockwood et al. consisted of a calorimeter foil placed between a passive front layer and a bulk sample, which was typically larger than the range of electrons. All components, including the calorimeter, were made of the same material. A few complementary measurements were performed with mixed material layers; these experiments are however not considered in the current benchmarks. In a few cases (Be and U), calorimeter foils were coated with thin Al shields ($\sim 1 \mu\text{m}$) for the purpose of thermal isolation. Repeated measurements with front foils of increasing thickness allowed to obtain depth-absorbed dose distributions. Depending on the beam energy and material, the thickness of calorimeter foils represented less than one percent of the electron CSDA range R in some cases, and up to several tens of percent of R in other cases (see Equation (2.18) for the definition of R). Measurement depths were determined as the sum of the front foil thickness plus half of the calorimeter thickness. In their publications, Lockwood et al. express experimental depth-dose profiles as:

$$D(z') = \frac{E}{d\rho}, \quad (4.1)$$

where z' is the measurement depth z as a fraction of R , E is the energy deposition in the calorimeter per incident electron, and d and ρ are the calorimeter thickness and density, respectively. Table 4.1 summarizes CSDA ranges used by Lockwood et al. together with corresponding values [195] reported by the United States National Institute of Standards and Technology (NIST).

The experimental uncertainty of dose values was quoted as 1.2%–2.2%, depending on the target material. For a fraction of the measurements (Be, Al and Ta), the employed high-precision calorimetric system [196] revealed higher beam energies compared to the nominal ones; differences of up to 16% were reported. The error of beam energy measurements was specified to be less than 0.1%.

4.2.2 Monte Carlo simulation

As a part of the benchmarks, a dedicated Geant4-based application was developed, aiming to mimic essential features of the experiment. The measurement setup was represented by a cylindrical target exposed to a pencil beam with Gaussian energy distribution and zero divergence. The width and

Material	Ref.	R (g/cm ²)				
		0.05 MeV	0.1 MeV	0.3 MeV	0.5 MeV	1.0 MeV
Be	Lockwood et al.	0.00604	0.0189	0.107	0.224	0.554
	NIST	0.00526	0.0175	0.104	0.219	0.546
C	Lockwood et al.	–	–	–	–	0.489
	NIST	–	–	–	–	0.496
Al	Lockwood et al.	0.00663	0.0203	0.113	0.234	0.569
	NIST	0.00574	0.0187	0.108	0.226	0.555
Fe	Lockwood et al.	–	–	0.121	0.249	0.606
	NIST	–	–	0.122	0.253	0.616
Cu	Lockwood et al.	–	–	0.125	0.258	0.625
	NIST	–	–	0.126	0.262	0.637
Mo	Lockwood et al.	–	0.0246	0.137	0.281	0.673
	NIST	–	0.0245	0.137	0.281	0.675
Ta	Lockwood et al.	–	–	0.160	0.325	0.763
	NIST	–	–	0.161	0.325	0.766
U	Lockwood et al.	–	–	0.174	0.349	0.809
	NIST	–	–	0.173	0.348	0.807

Table 4.1: Electron CSDA ranges from Lockwood et al. [186] and the NIST [195] database. Ranges are only shown for energy-material combinations considered by Lockwood et al.

mean of the Gaussian were set according to experimental beam characteristics, considering higher than nominal beam energies in the case of Be, Al and Ta. Densities and mean excitation energies of target materials were taken from the Geant4 material database [27], which is based on reference data sets of NIST [197]. A summary of material properties can be found in Table 7.1 of the Appendix, Section A.1. Target samples were assumed to contain no impurities. This was considered legitimate as no information about material compositions were reported in the considered references.

The energy deposition by primary electrons and secondary particles was scored in plane-parallel slabs. Position and thickness of the slabs accurately represented the calorimeter setup in the experiment, accounting for the fact that measurement depths generally followed a non-uniform longitudinal pattern. Calorimeter coatings were not implemented since Lockwood et al. already incorporated a target material-equivalent contribution into measurement depths. The effect due to different scattering characteristics in coatings was estimated to be negligible for the validation. The scoring geometry was invisible to particle tracking, i.e. particle steps were not interrupted at slab boundaries. In order to account for the continuous energy loss electrons experience along condensed history steps, the energy deposition was assigned to a random point on the linear track segment connecting the start and end-point

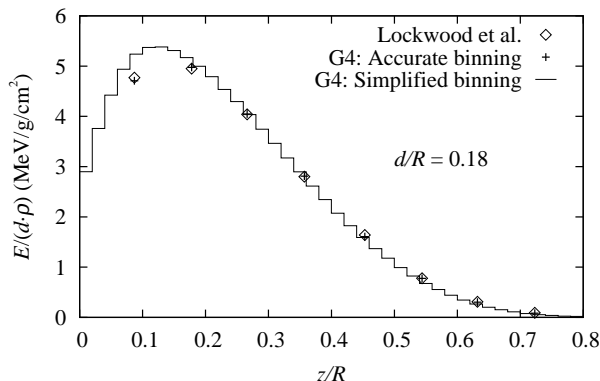


Figure 4.1: Energy deposition per density-weighted calorimeter thickness vs depth for 300 keV electrons incident on Cu: comparison of experimental data from Lockwood et al. [186, 187] against Geant4 9.1.p03 simulation results obtained either with a simplified geometrical model based on a uniform scoring grid (histograms) or, alternatively, an accurate model which incorporates actual calorimeter geometries (crosses).

of a step.

The accurate description of the calorimeter setup proved to be essential for the benchmark study given that the longitudinal dose gradient varied considerably within the calorimeter volume for some beam/target combinations. The impact of the scoring geometry was particularly important at lower beam energies, where the calorimeter thickness accounted for a considerable fraction of the CSDA range of incident electrons. In this case, using an approximative description of the experimental setup can lead to non-negligible artifacts. This is illustrated in Figure 4.1, showing calculated and measured energy deposition profiles of 300 keV electrons in Cu; simulation results correspond to two different spatial scoring configurations, one being based on equally-sized, consecutive scoring bins and a second which accurately reproduces experimental calorimeter sizes and measurement depths. In both cases, the energy deposition displayed is weighted by the inverse of the surface density of scoring slabs. It is evident from the comparison, that a simplified scoring geometry can lead to non-negligible artifacts in the dose build-up. Similar conclusions can be drawn for other target materials. It is worth noting, that none of the past Monte Carlo benchmarks involving data from Lockwood et al. (see e.g. [188–194]) accounted for an accurate description of calorimeter geometries.

All benchmark calculations presented in this study were based on fully coupled electron-photon simulations, which included the generation and trans-

port of δ -electrons and Bremsstrahlung photons. A discussion of production thresholds employed in the simulation setup is given in the following section. Two sets of Geant4 electron and photon interaction models were examined (see Section 3.2.1): one being based on EEDL and EPDL97 libraries, and the second employing algorithms originally developed for the PENELOPE code. Electron multiple scattering was described using the semi-empirical model by Urbán (when the current study was carried out, the model by Urbán was the only approach to multiple scattering available in Geant4). In this model, the scattering angle and the spatial displacement are determined by means of model distributions designed to yield first and second moments in agreement with the theory of Lewis [62]. The author of the model used experimental data from different sources to tune parameters of the scattering distributions. The variants of the multiple scattering model employed in the two considered Geant4 versions (8.2.p01 and 9.1/9.1.p01) differ in their implementation; noteworthy, the expression of the mean scattering angle has been modified. Differences in dose distributions obtained with toolkit versions 8.2.p01 and 9.1/9.1.p01 can hence be attributed to modifications of the multiple scattering algorithm as other models considered in this study have remained unaltered.

4.2.3 Transport parameter settings

It was demonstrated in previous publications [148–151, 194] that, in certain cases, Geant4 electron transport calculations exhibit a dependency on simulation parameters. Poon et al. [151], for example, showed that (using Geant4 6.1) the energy spectrum and angular distribution of 1 MeV electrons transmitted through a thin aluminium layer can considerably depend on parameters governing the step size. They demonstrated that smaller step sizes significantly improve the agreement with EGSnrc simulations. Similarly, dose profiles of 1 MeV electrons in water were closer to EGSnrc results when choosing a smaller production threshold T_{cut} and a small user-defined step limit. In another paper, Poon and Verhaegen [150] reported similar findings for ionization chamber simulations. More recently, and based on Geant4 8.1, Kadri et al. [194] showed that the total energy deposited by ~ 0.5 MeV electrons in Al and Ta samples also depends to some degree on T_{cut} as well as on the multiple scattering parameter f_r . As reported [27, 149], the multiple scattering model was improved in several respects (from version 8.0 on) to remedy some of the observed problems.

In the current study, two different transport parameter configurations were used. Corresponding settings are summarized in Table 4.2. Configuration “A” applies a secondary production threshold T_{cut} of 1 keV and ad-

		Configuration A	Configuration B
Ionization/Bremsstrahlung	T_{cut}	1 keV	0.25 keV
	α_R	0.01	0.20*
	ρ	0.1-1 μm	200 μm^*
Multiple scattering	f_r	0.02*	0.02*
User-defined		calorimeter size	1 μm

Table 4.2: Transport parameter settings used in the benchmarks. Values labelled with a star correspond to the default settings in the considered Geant4 versions.

ditionally limits particle steps by using small values for parameters entering Equation (3.3). In contrast, stepping configuration “B” is more restrictive by employing the lowest recommended limit for secondary production and a user-defined step limit of 1 μm . In either case, values of multiple scattering parameters were not changed from their default settings.

4.3 Results and discussion

Energy deposition profiles were calculated for all combinations of beam energy, incident angle and target material. The number of primary particles tracked in the Monte Carlo simulations was 5×10^5 for electron energies ≥ 300 keV and 1×10^6 for energies < 300 keV. This resulted in statistical errors $< 1\%$ except in tails of distributions, where errors were as large as a few percent in some cases. The statistical uncertainty of the energy deposition around the peak was $< 0.3\%$ in all materials. Simulation errors are not displayed in figures for the clarity of plots. Distributions are expressed according to (4.1).

4.3.1 Comparison of different Geant4 versions and transport parameter configurations

Figs. 4.2–4.9 compare Geant4-calculated and measured [186, 187] dose profiles of 0.058–1.033 MeV electrons normally incident on different target samples (Be to U). Simulation results displayed in the plots correspond to different Geant4 versions and transport parameter configurations: 8.1.p02 with configuration “A”, and 9.1.p03 and 9.1 with configuration “A” and “B”, respectively. All calculations were performed with EEDL and EPDL97-based models. Dashed lines indicate the experimental uncertainty quoted by Lockwood et al.

When based on the same set of transport parameters, simulation predic-

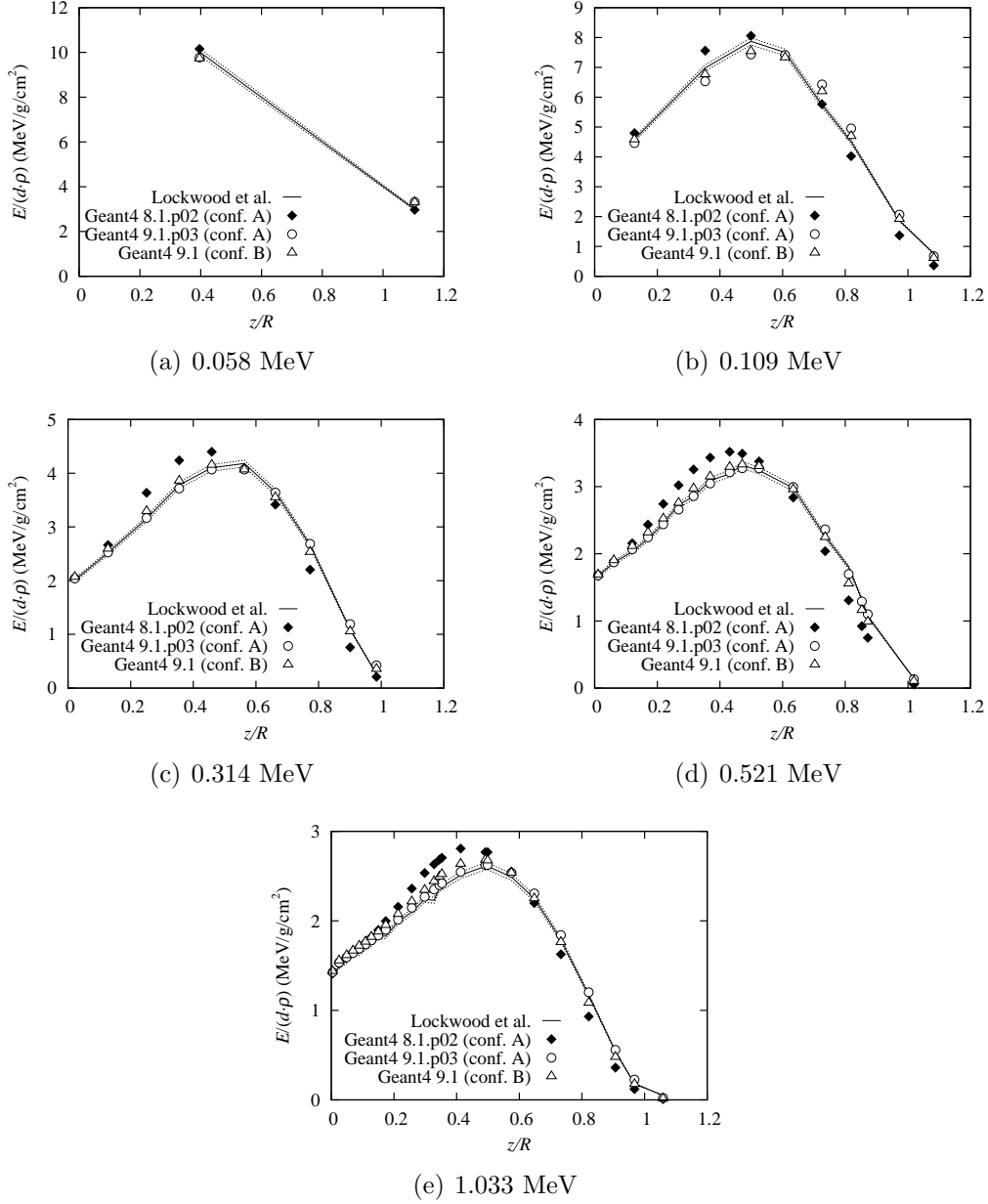


Figure 4.2: Energy deposition per density-weighted calorimeter thickness vs depth in Be for (a) 0.058 MeV, (b) 0.109 MeV, (c) 0.314 MeV, (d) 0.521 MeV and (e) 1.033 MeV electrons incident at 0° . Experimental data from Lockwood et al. [186, 187] are compared against Geant4 simulation results based on different Geant4 versions (8.1.p01 and 9.1.p03) and parameter configurations (see Table 4.2). Dashed lines indicate the experimental uncertainty.

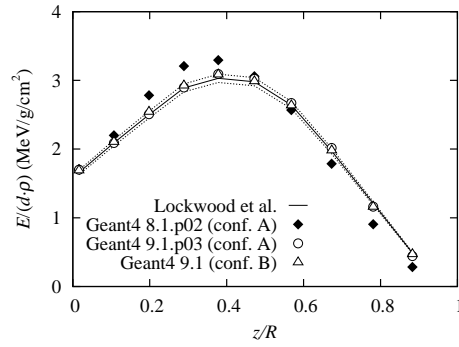


Figure 4.3: Energy deposition per density-weighted calorimeter thickness vs depth in C for 1 MeV electrons incident at 0° . Details as in Fig. 4.2.

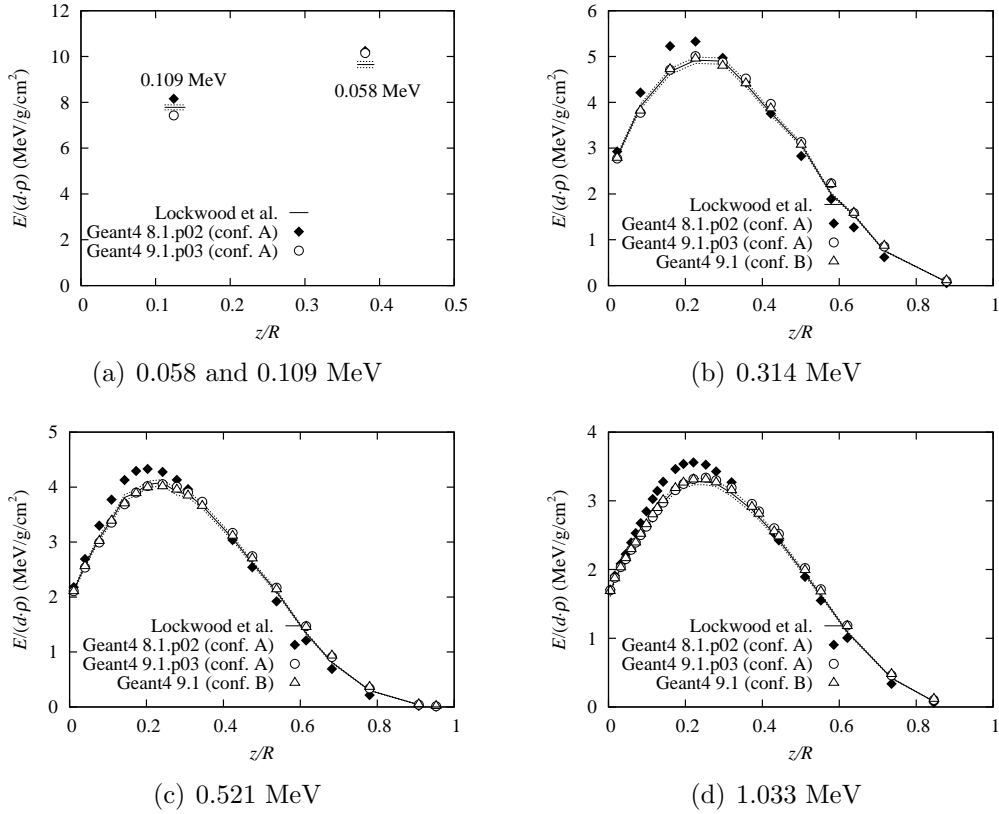


Figure 4.4: Energy deposition per density-weighted calorimeter thickness vs depth in Al for (a) 0.058/0.109 MeV, (b) 0.314 MeV, (c) 0.521 MeV and (d) 1.033 MeV electrons incident at 0° . Details as in Fig. 4.2.

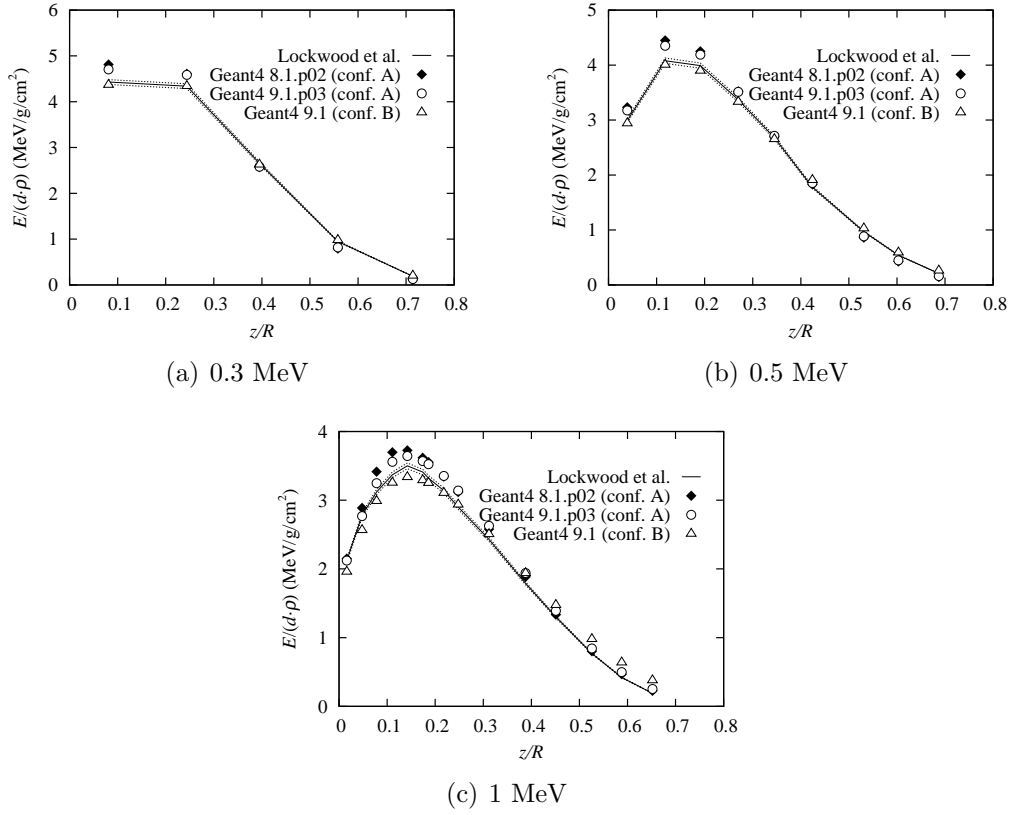


Figure 4.5: Energy deposition per density-weighted calorimeter thickness vs depth in Fe for (a) 0.3 MeV, (b) 0.5 MeV and (c) 1 MeV electrons incident at 0° . Details as in Fig. 4.2.

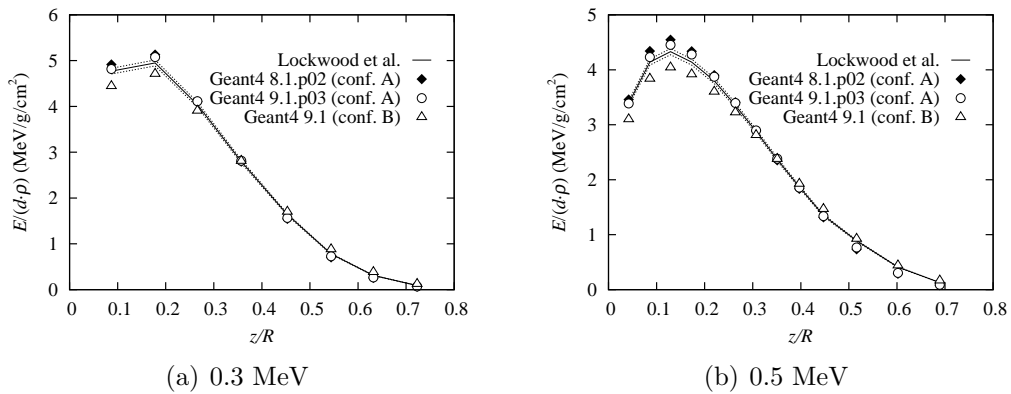
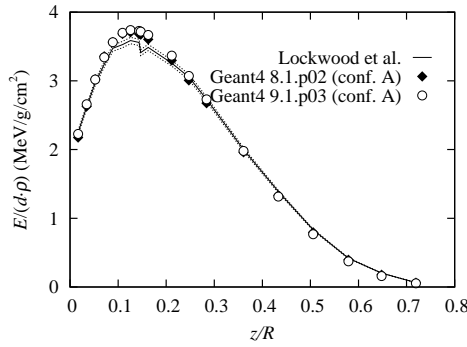
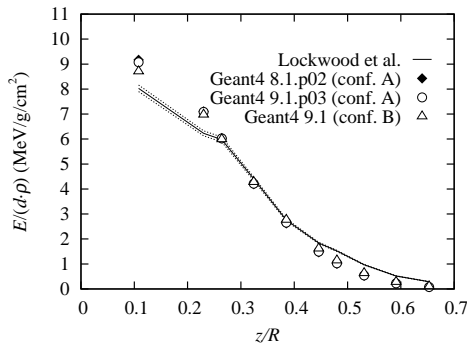


Figure 4.6: Energy deposition per density-weighted calorimeter thickness vs depth in Cu for (a) 0.3 MeV, (b) 0.5 MeV and (c) 1 MeV electrons incident at 0° . Details as in Fig. 4.2. Figure continued on next page.

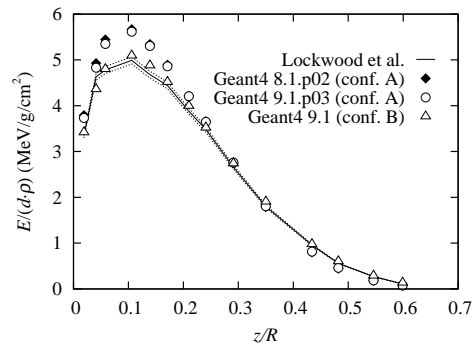


(c) 1 MeV

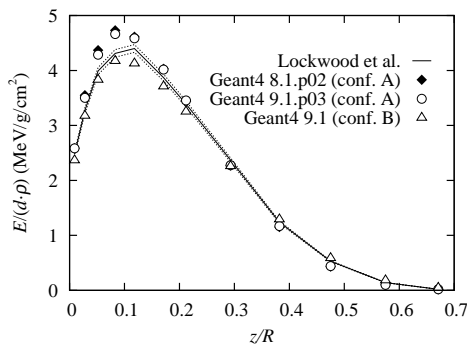
Figure 4.6: **(cont.)** Energy deposition per density-weighted calorimeter thickness vs depth in Cu for (a) 0.3 MeV, (b) 0.5 MeV and (c) 1 MeV electrons incident at 0° . Details as in Fig. 4.2.



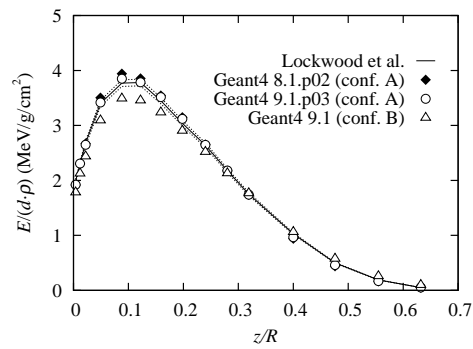
(a) 0.1 MeV



(b) 0.3 MeV



(c) 0.5 MeV



(d) 1 MeV

Figure 4.7: Energy deposition per density-weighted calorimeter thickness vs depth in Mo for (a) 0.1 MeV, (b) 0.3 MeV, (c) 0.5 MeV and (d) 1 MeV electrons incident at 0° . Details as in Fig. 4.2.

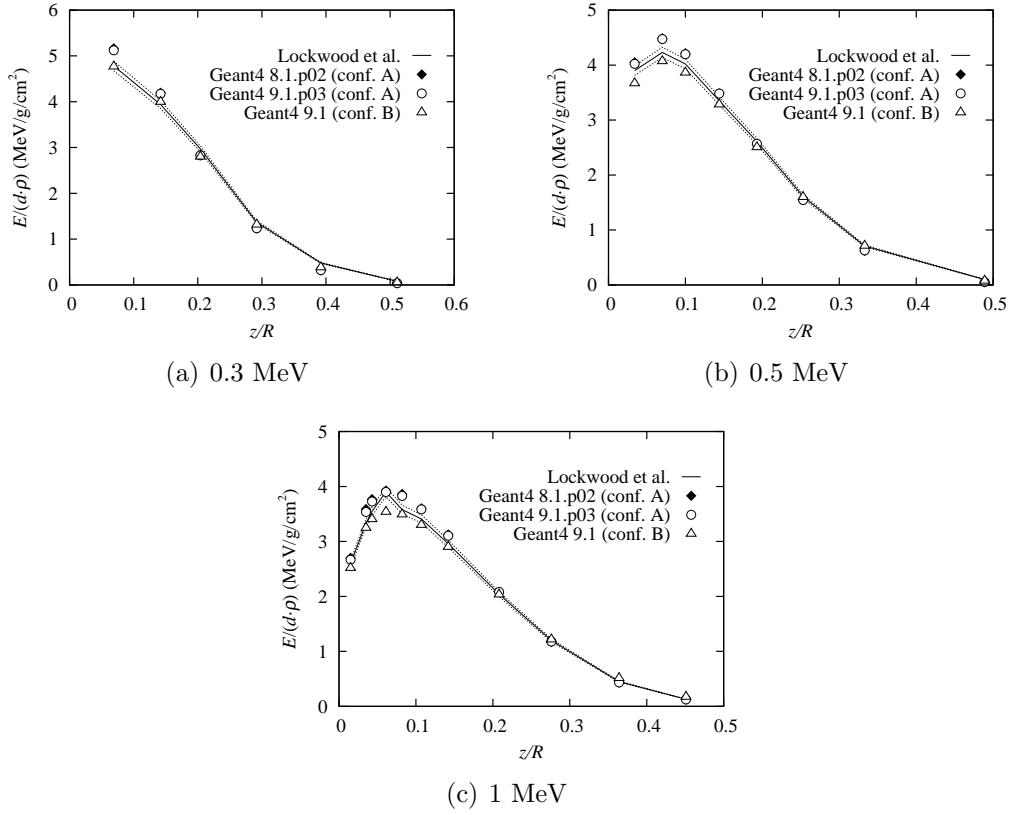


Figure 4.8: Energy deposition per density-weighted calorimeter thickness vs depth in Ta for (a) 0.3 MeV, (b) 0.5 MeV and (c) 1 MeV electrons incident at 0° . Details as in Fig. 4.2.

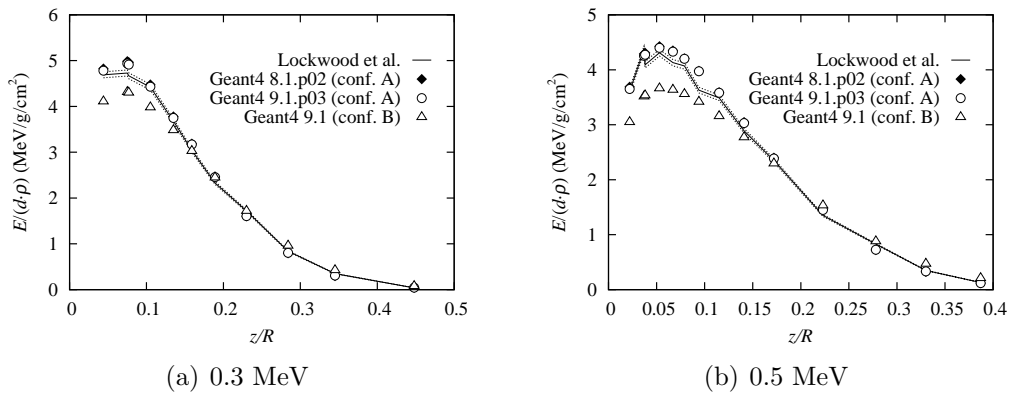
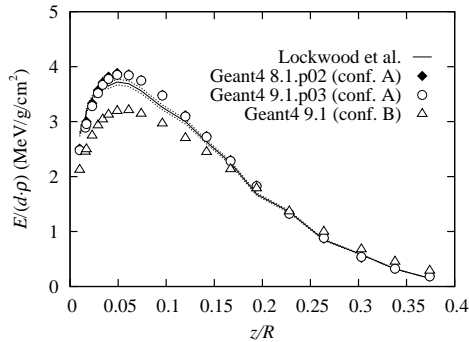


Figure 4.9: Energy deposition per density-weighted calorimeter thickness vs depth in U for (a) 0.3 MeV, (b) 0.5 MeV and (c) 1 MeV electrons incident at 0° . Details as in Fig. 4.2. Figure continued on next page.



(c) 1 MeV

Figure 4.9: **(cont.)** Energy deposition per density-weighted calorimeter thickness vs depth in U for (a) 0.3 MeV, (b) 0.5 MeV and (c) 1 MeV electrons incident at 0° . Details as in Fig. 4.2.

tions obtained with toolkit versions 8.1.p02 and 9.1.p03 exhibit significant differences in lower- Z materials, whereas discrepancies tend to be smaller in high- Z target samples. In the case of Be, C and Al, profiles based on Geant4 9.1.p03 are generally in good agreement with experimental data, while simulations performed with version 8.1.p02 yield less penetrating dose distributions, with peaks being up to $\sim 10\%$ higher than measured ones. With some exceptions, both toolkit versions tend (when based on parameter set “A”) to overestimate experimental dose values around the peak in medium and high- Z samples. In a few cases, previous studies reported similar observations for other Monte Carlo codes (see, for example, PENELOPE results for 1 MeV electrons shown by Sempau et al. [191]). As suspected by Sempau et al., one cannot completely rule out a systematic error present in some of the measurements.

Despite the significantly differing dose pattern in lower- Z materials, the total energy E_{tot} deposited in target samples is only moderately affected by differences across toolkit versions: predictions of E_{tot} obtained with Geant4 8.1.p02 and 9.1.p03 agree within 1% for all materials. This indicates that electrons eventually backscattered from absorbers are less sensitive to the modifications in the multiple scattering algorithm.

Apart from discrepancies across toolkit versions, the figures demonstrate a significant dependency on the employed parameter configuration for simulations involving medium and high- Z media. Compared to distributions obtained with parameter configuration “A”, configuration “B” results in a lower peak dose and a less rapid fall-off in Fe, Cu, Mo, Ta, and U. None of the parameter sets yields a consistently better agreement with measurements

across all materials and electron energies.

4.3.2 Evaluation of the simulation accuracy with different physics models

A second set of calculations was performed to examine predictions of alternative Geant4 energy loss and secondary production algorithms originally developed for the PENELOPE code. Figs. 4.10–4.17 compare experimental energy deposition profiles [186, 187] with simulation results obtained with library-based and PENELOPE-like physics models, respectively. Simulations were performed with Geant4 version 9.1.p03, employing stepping configuration “A”. As in the previous section, dashed lines indicate the quoted experimental uncertainty.

Compared to library-based interaction models, PENELOPE-like models predict a slightly lower peak maximum in low- Z materials (Be and C), a comparable peak height in Al, and a higher peak in materials heavier than Al. With the set of transport parameter values selected in the current study, both physics configurations reproduce equally well experimental profiles in light absorbers (Figs. 4.10–4.12), whereas simulations with library-based physics models generally yield a better description of the measured data for $Z \geq 26$ (Figs. 4.13–4.17). Apart from this overall trend, it can be seen that in some absorbers (e.g. Mo) discrepancies among Monte Carlo results are smaller than the difference between simulation and experiment.

In the energy range considered, electron energy losses due to bremsstrahlung emission are significantly smaller than losses due to target ionization and atomic excitation. For example, radiative stopping powers of 1 MeV electrons are approximately one order of magnitude smaller than collision stopping powers in Ta, and more than two orders of magnitude smaller in Be. Consequently, discrepancies in dose distributions calculated with library-based and PENELOPE-like models are likely due to different cross sections associated with the production of δ -electrons. As reported by Poon and Verhaegen [150], for a T_{cut} value of 10 keV the mean free path for δ -emission predicted by EEDL-based and PENELOPE-like models differs by roughly 10% for 1 MeV electrons in tungsten. On the other hand, Kadri et al. [194] showed that depth-dose profiles of 0.5 MeV electrons in Mo and Ta exhibit only small differences if a large production threshold is selected which effectively suppresses the generation of δ -electrons. This supports the conclusion, that discrepancies observed in energy deposition profiles can be attributed to differences in δ -electron production cross sections (and corresponding mean free paths).

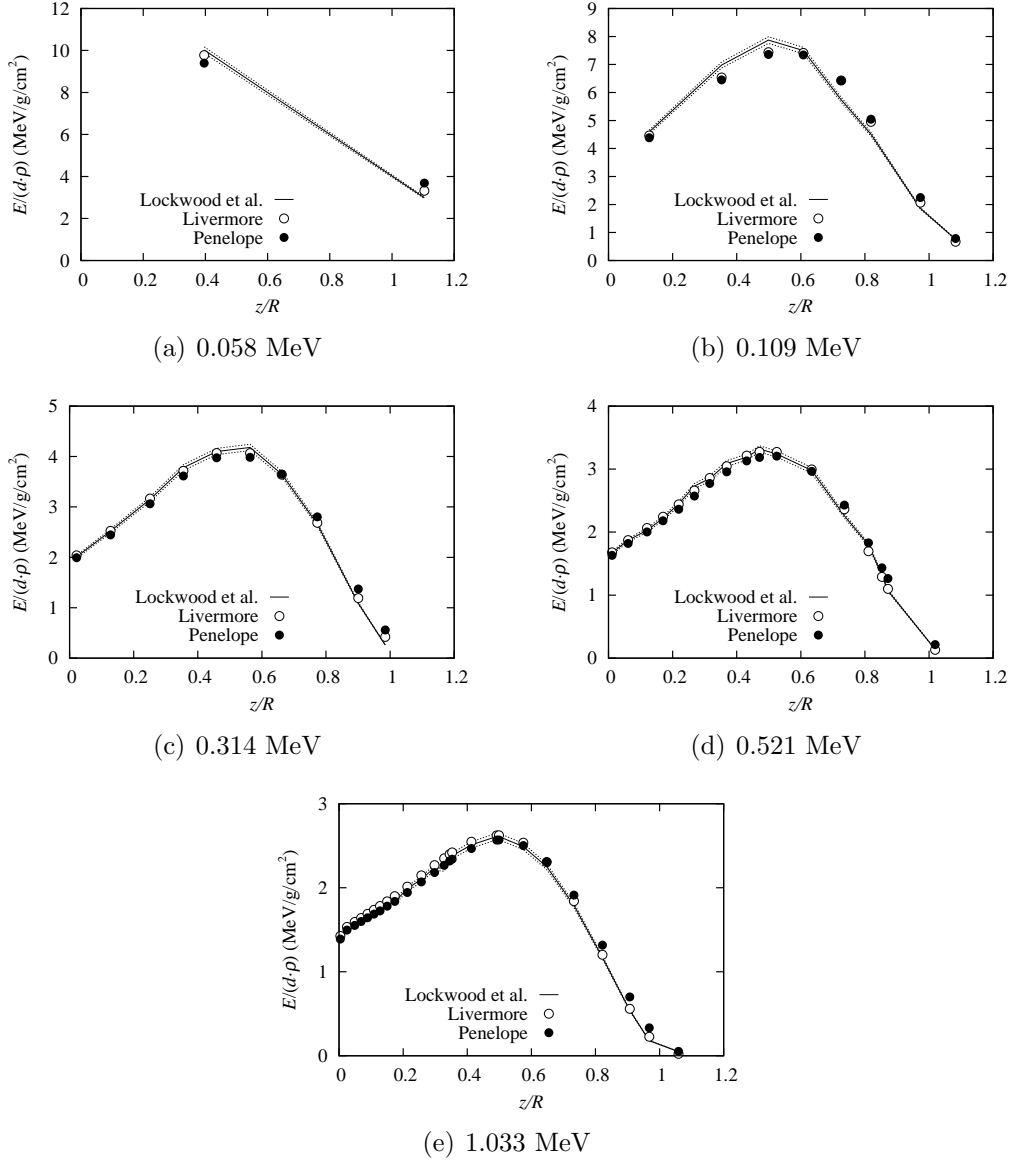
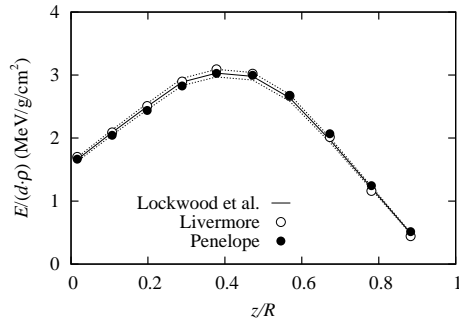
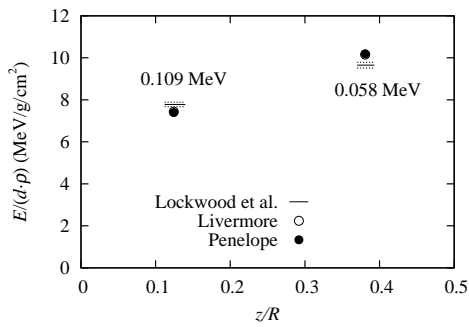


Figure 4.10: Energy deposition per density-weighted calorimeter thickness vs depth in Be for (a) 0.058 MeV, (b) 0.109 MeV, (c) 0.314 MeV, (d) 0.521 MeV and (e) 1.033 MeV electrons incident at 0° . Experimental data from Lockwood et al. [186, 187] are compared against Geant4 simulation results based on library-based (Livermore) and PENELOPE-like physics models. Results were obtained with Geant4 9.1.p03, employing parameter configuration “A”. Dashed lines indicate the quoted experimental uncertainty.

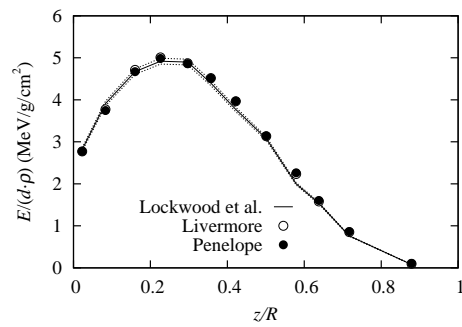


(a) 1 MeV

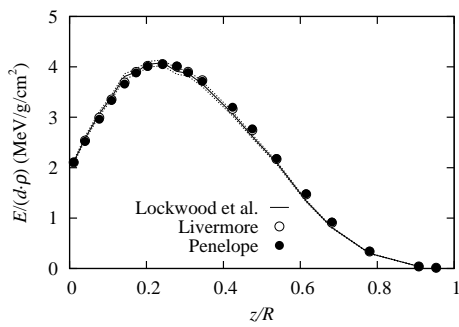
Figure 4.11: Energy deposition per density-weighted calorimeter thickness vs depth in C for 1 MeV electrons incident at 0° . Details as in Fig. 4.10.



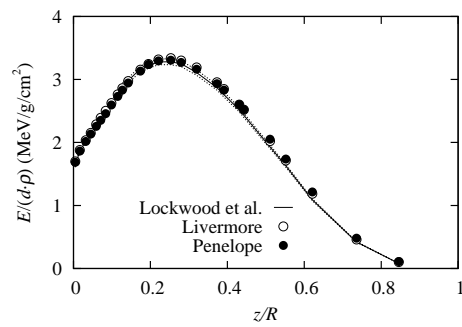
(a) 0.058 and 0.109 MeV



(b) 0.314 MeV



(c) 0.521 MeV



(d) 1.033 MeV

Figure 4.12: Energy deposition per density-weighted calorimeter thickness vs depth in Al for (a) 0.058/0.109 MeV, (b) 0.314 MeV, (c) 0.521 MeV and (d) 1.033 MeV electrons incident at 0° . Details as in Fig. 4.10.

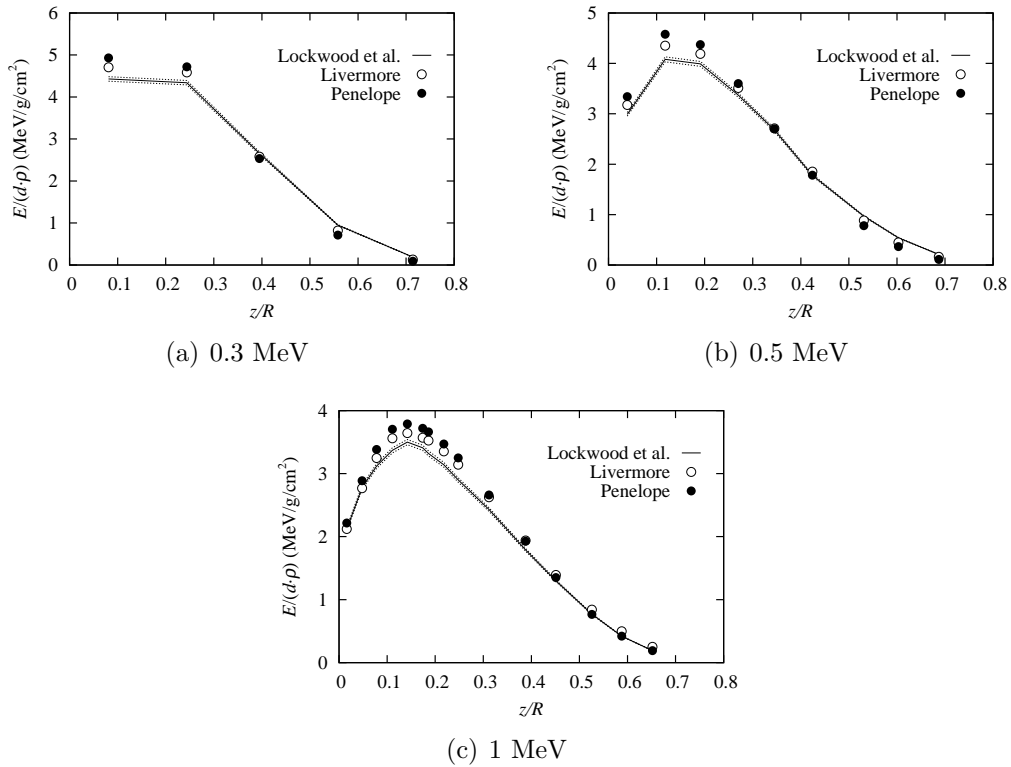


Figure 4.13: Energy deposition per density-weighted calorimeter thickness vs depth in Fe for (a) 0.3 MeV, (b) 0.5 MeV and (c) 1 MeV electrons incident at 0°. Details as in Fig. 4.10.

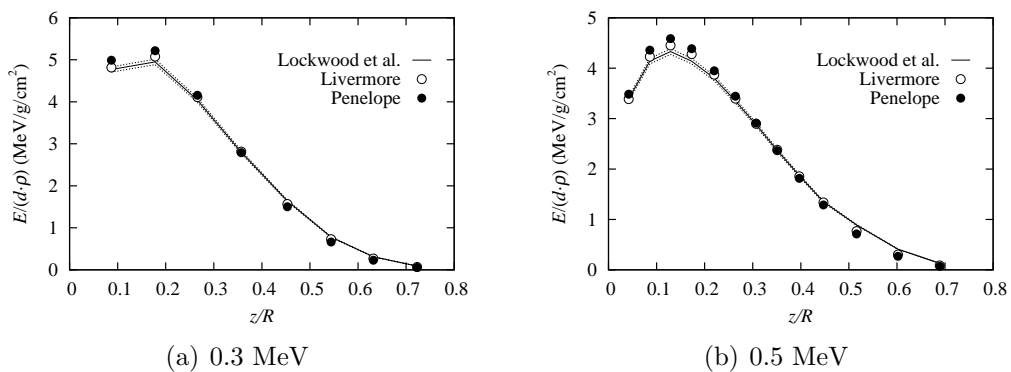
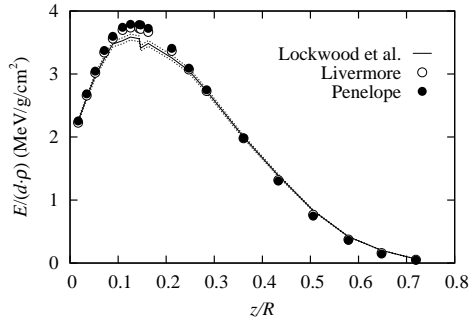
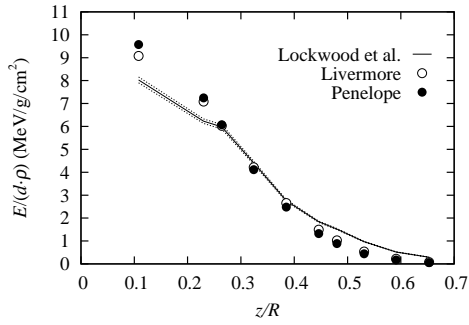


Figure 4.14: Energy deposition per density-weighted calorimeter thickness vs depth in Cu for (a) 0.3 MeV, (b) 0.5 MeV and (c) 1 MeV electrons incident at 0°. Details as in Fig. 4.10. Figure continued on next page.

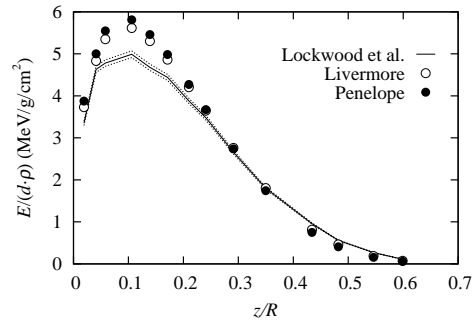


(c) 1 MeV

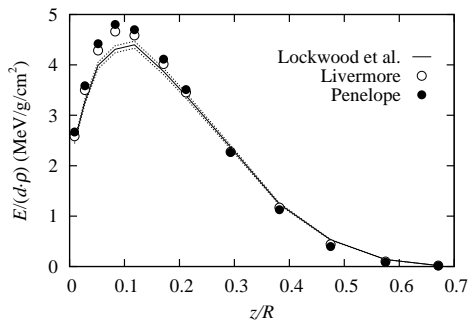
Figure 4.14: (cont.) Energy deposition per density-weighted calorimeter thickness vs depth in Cu for (a) 0.3 MeV, (b) 0.5 MeV and (c) 1 MeV electrons incident at 0° . Details as in Fig. 4.10.



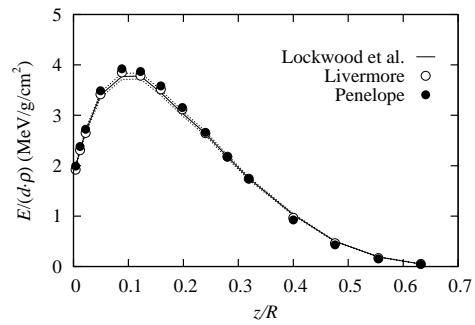
(a) 0.1 MeV



(b) 0.3 MeV



(c) 0.5 MeV



(d) 1 MeV

Figure 4.15: Energy deposition per density-weighted calorimeter thickness vs depth in Mo for (a) 0.1 MeV, (b) 0.3 MeV, (c) 0.5 MeV and (d) 1 MeV electrons incident at 0° . Details as in Fig. 4.10.

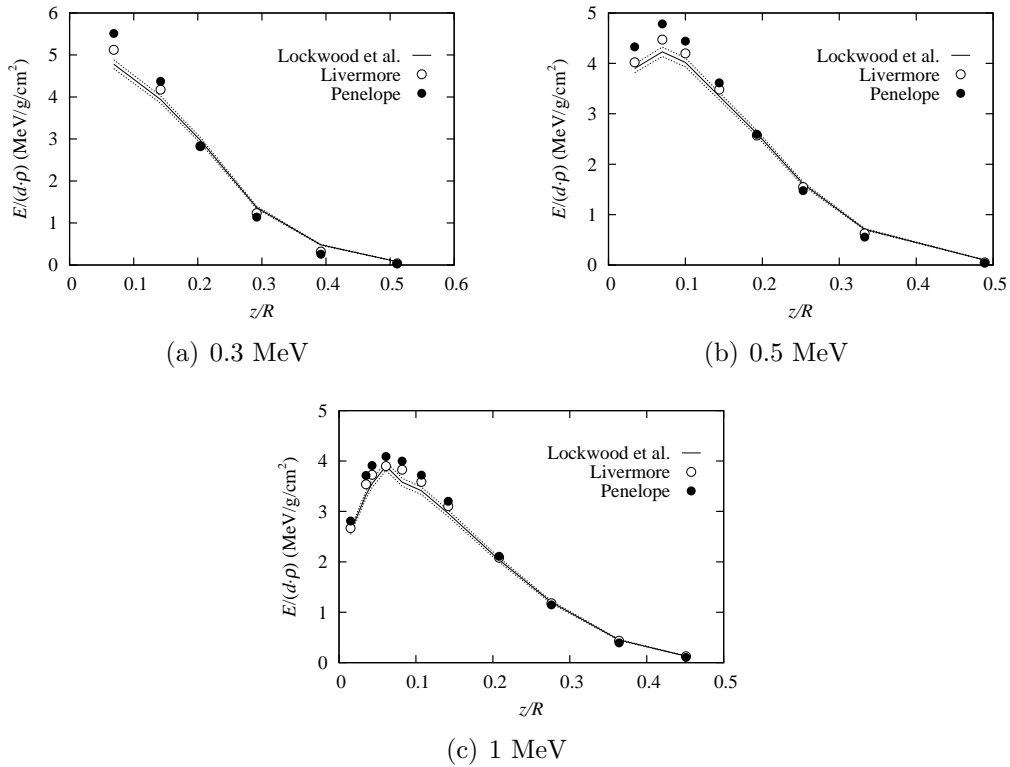


Figure 4.16: Energy deposition per density-weighted calorimeter thickness vs depth in Ta for (a) 0.3 MeV, (b) 0.5 MeV and (c) 1 MeV electrons incident at 0°. Details as in Fig. 4.10.

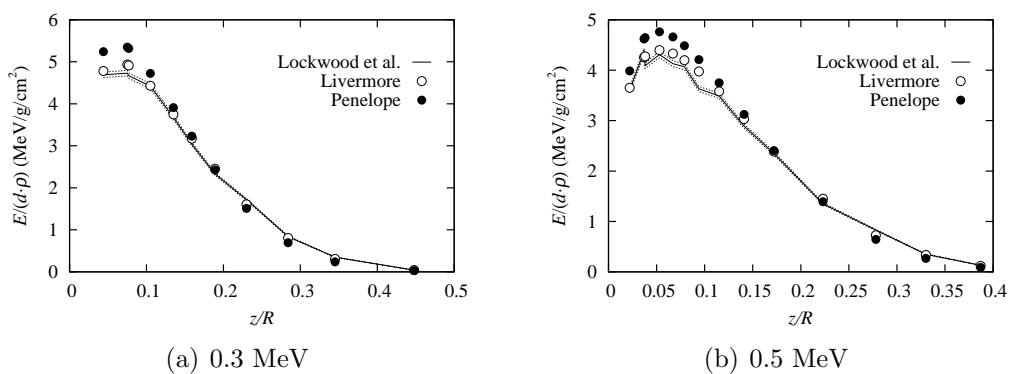
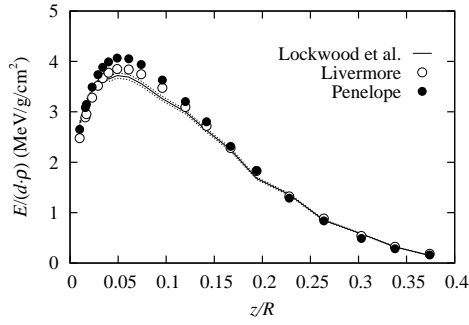
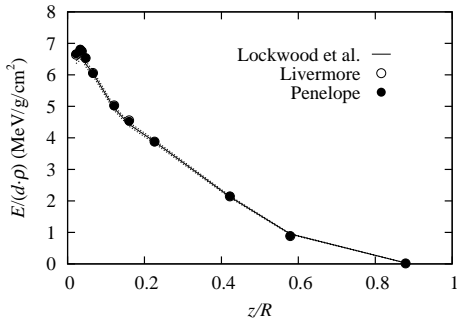


Figure 4.17: Energy deposition per density-weighted calorimeter thickness vs depth in U for (a) 0.3 MeV, (b) 0.5 MeV and (c) 1 MeV electrons incident at 0°. Details as in Fig. 4.10. Figure continued on next page.

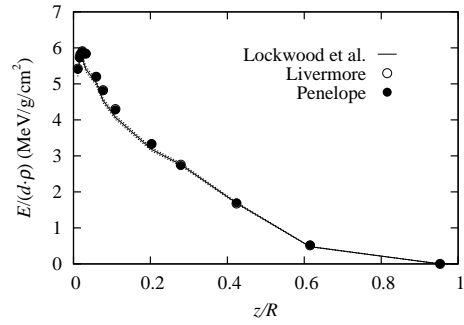


(c) 1 MeV

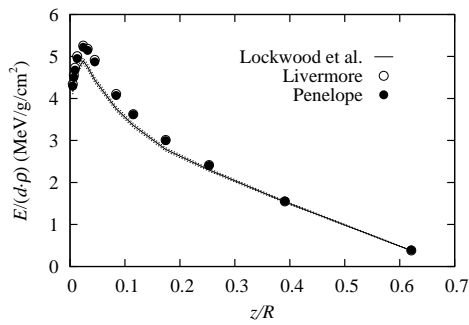
Figure 4.17: (**cont.**) Energy deposition per density-weighted calorimeter thickness vs depth in U for (a) 0.3 MeV, (b) 0.5 MeV and (c) 1 MeV electrons incident at 0° . Details as in Fig. 4.10.



(a) 0.314 MeV



(b) 0.521 MeV



(c) 1.033 MeV

Figure 4.18: Energy deposition per density-weighted calorimeter thickness vs depth in Al for (a) 0.314 MeV, (b) 0.521 MeV and (c) 1.033 MeV electrons incident at 60° . Details as in Fig. 4.10.

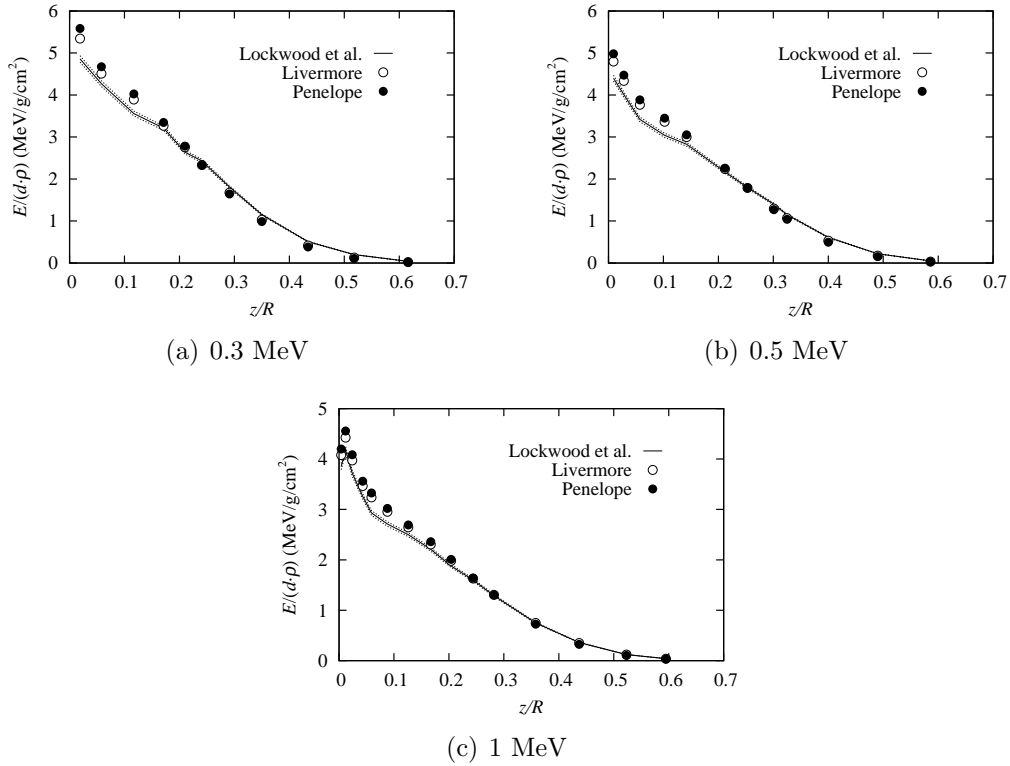
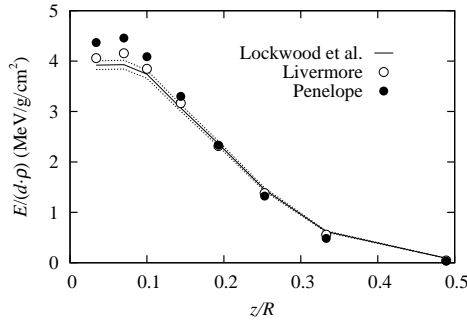


Figure 4.19: Energy deposition per density-weighted calorimeter thickness vs depth in Mo for (a) 0.3 MeV, (b) 0.5 MeV and (c) 1 MeV electrons incident at 60°. Details as in Fig. 4.10.

It is remarked that current results are not directly comparable with simulations based on the native PENELOPE code (e.g. in [191]), since the treatment of multiple scattering and transport mechanics are significantly different in both simulation packages.

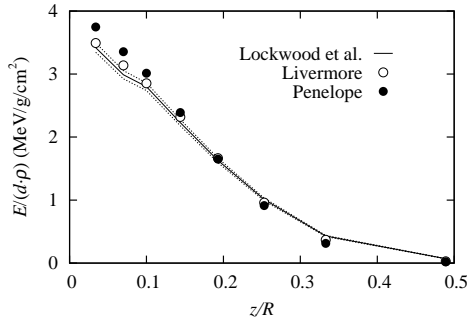
4.3.3 Comparison of data at 30° and 60° electron beam incidence

Complementing the comparison of dose distributions at normal beam incidence, Figs. 4.18–4.22 show calculated and experimental [186, 187] dose profiles at oblique electron incidence ($\alpha=30^\circ$ and 60°). Experimental data are available only for a smaller set of targets (Al, Ta, Mo, and U) and fewer beam energies. As in the previous section, figures display simulation results obtained with library-based and PENELOPE-like models, respectively. All simulations were performed with toolkit version 9.1.p03, using the same set

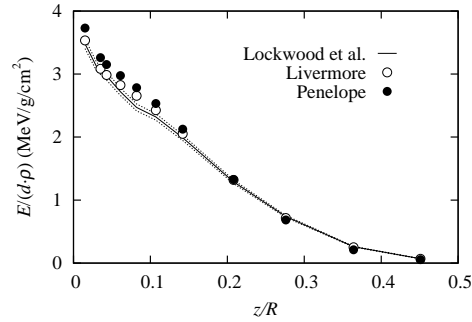


(a) 0.5 MeV

Figure 4.20: Energy deposition per density-weighted calorimeter thickness vs depth in Ta for (a) 0.5 MeV electrons incident at 30° . Details as in Fig. 4.10.



(a) 0.5 MeV



(b) 1 MeV

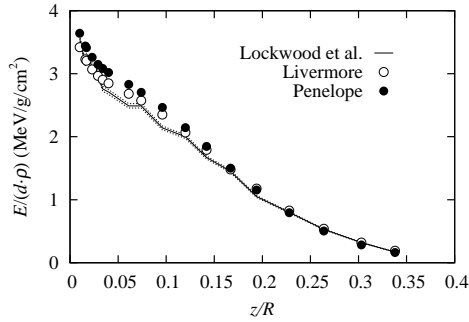
Figure 4.21: Energy deposition per density-weighted calorimeter thickness vs depth in Ta for (a) 0.5 MeV and (b) 1 MeV electrons incident at 60° . Details as in Fig. 4.10.

of stepping parameters (“A”) as above.

Obtained results exhibit similar characteristics as for normal beam incidence. Except for Al, library-based models yield a lower dose than PENelope-like models at shallow depths. As can be seen in the plots, experimental distributions are generally better reproduced by the first set of models.

4.4 Conclusions

In this chapter, dose profiles of ≤ 1 MeV electrons in solids were studied for a large range of experimental configurations. Based on the obtained results, one can conclude that modifications of the multiple scattering algorithm,



(a) 1 MeV

Figure 4.22: Energy deposition per density-weighted calorimeter thickness vs depth in U for (a) 1.0 MeV electrons incident at 30° . Details as in Fig. 4.10.

introduced between version 8.1.p02 and 9.1.p03, improved Monte Carlo predictions in Al and lighter materials. Experimental peak dose and the distal fall-off are more accurately reproduced. This demonstrates an improvement with respect to previous studies by Kadri et al. [194], who employed Geant4 8.1. In contrast, no significant change in dose distributions was observed for medium and high- Z targets. Additionally, results were found to exhibit a non-negligible dependency on transport parameters. A similar dependency was also reported by other authors in previous publications (see e.g. [150]). Besides that, for parameter values considered in the current study, library-based models yielded results in better agreement with dose measurements than PENELOPE-like models.

Chapter 5

Simulation benchmark of electron backscattering from solid targets

A fundamental, but challenging aspect of condensed history Monte Carlo transport is the accurate description of fluence perturbations in the vicinity of material interfaces due to electron backscatter [95, 198]. Backscattering phenomena can be observed whenever electrons are exposed to inhomogeneous scattering conditions. A quantitative description of corresponding effects like dose enhancement upstream of material heterogeneities can be critical to simulation studies in radiotherapy, for example when examining backscatter contributions to the monitor chamber response in external beam radiotherapy [199]; when studying effects of inserts (e.g. Pb shields) on dose and particle spectra in phantoms [200–204]; when investigating dose backscatter factors for beta sources employed in brachytherapy [205, 206]; or when designing attenuators for use in intraoperative electron beam therapy [207, 208]. Besides their importance in radiotherapy applications, backscattering phenomena are also relevant to many other fields, for example β -spectroscopy [28].

This chapter¹ presents a comprehensive benchmark of Geant4 electron transport algorithms by examining their ability to yield a quantitative description of electron backscattering from solid targets. The accuracy of sim-

¹The results presented in this chapter were summarized in a paper submitted to Nucl. Instr. and Meth. B (paper under review as of December 27, 2011): A. Lechner, V.N. Ivanchenko, L. Urbán, M. Maire, O. Kadri, “Geant4 simulation of electron backscattering from solid targets”. Preliminary results were published in: A. Schälicke, A. Bagulya, Ø. Dale, F. Dupertuis, V. Ivanchenko, O. Kadri, A. Lechner, M. Maire, M. Tsagri, L. Urbán, Geant4 electromagnetic physics for the LHC and other HEP applications, J. Phys.: Conf. Ser. 331 (2011) 032029.

ulation models is investigated by validating Monte Carlo predictions against experimental backscattering data available in the literature. The main objective is to establish the accuracy of Geant4 models for simulation scenarios where electron backscattering is critical.

5.1 Previous studies and outline

Following the earlier studies by Carrier et al. [193] and Kadri et al. [194], as well as the benchmarks presented in the previous chapter (partly published in Lechner et al. [209]), several authors pursued with further comparisons of Geant4 electron transport simulations against experimental data or other, well-validated Monte Carlo codes such as EGSnrc. In a recent article, Maigne et al. [152] demonstrated a good agreement between GATE/Geant4 and EGSnrc dose point kernels and pencil beam kernels in water at energies 0.05–4 MeV and 0.015–20 MeV, respectively. These results confirmed an improvement over dose distributions previously obtained by Poon and Verhaegen [150]. The changes were mainly attributed to modifications of the multiple scattering model by Urbán. In two other studies, Vilches et al. [210] and Faddegon et al. [211] respectively found some discrepancies between experimental and Geant4-calculated angular distributions of 13 and 20 MeV electrons scattered by thin foils. As described by Faddegon et al., the agreement could however be significantly improved by retuning scatter distributions of the Urbán model. The modified configuration also entered subsequent Geant4 releases.

Electron backscatter calculations with Geant4, and their comparison with experimental data, have been reported previously in the literature, however these simulations were either restricted to a small energy range and/or a few target materials (see, for example, the Refs. [148, 149, 157, 212–215]), or they were part of publications with a wider scope [28]. In the current study, a broad range of energies, typically encountered in radiotherapy, is covered (0.1–14 MeV). The benchmarks are based on version 9.4 of the Geant4 toolkit, released in December 2010. Predictions of the simulation code are compared against published experimental data from Lockwood et al. [216, 217] and Tabata [218].

Lockwood et al. performed high-precision measurements of integral electron energy and charge albedos for beams incident at various angles on thick absorbers (these experiments were performed by the same group as the measurements discussed in the previous chapter). In the second study considered, Tabata presented angular spectra and integral fractions of electrons backscattered from bulk samples at normal beam incidence. The measurements de-

scribed in these publications cover complementary electron energies. In both cases, absorber materials studied encompass a large range of atomic numbers ($Z=4-92$). The backscatter measurements by these authors are among the most comprehensive experimental studies of their kind in the energy range considered.

The chapter is organized as follows. Section 5.2 summarizes the experiments and provides a detailed account of the simulation setup, including transport parameter settings and a brief overview of relevant Geant4 models. In addition, the impact of secondary production on the backscatter yield is briefly reviewed and aspects of Bremsstrahlung corrections pertaining to the energy backscatter measurements are discussed. Section 5.3 presents a comparison of obtained Monte Carlo results against experimental electron energy and number backscatter, as well as angular distributions. Concluding remarks are given in Section 5.4.

5.2 Materials and methods

The Monte Carlo benchmark presented in this chapter examines electron backscattering as a function of kinetic energy E_0 , incident angle α , and atomic number Z of the absorber material. As in the previous chapter, α is defined as the angle between the central beam axis and the absorber surface normal. The quantities studied are a) the ratio of reflected electrons to the number of incident electrons, η_N , and b) the ratio of backscattered and incident electron kinetic energies, η_E . The first quantity, η_N , is generally referred to as the electron backscatter coefficient [219].

5.2.1 Experimental data

Numerous publications reported backscatter experiments with keV and MeV electron beams at normal and oblique incidence. Compilations of experimental data were for example presented in the articles of Ali and Rogers [198] and Tabata et al. [220]. The backscatter measurements used in the current benchmarks [216–218] were partly adopted in previous Monte Carlo studies employing the PENELOPE [191, 221], ITS 3.0 [219, 222], and EGS5 [222] code systems. A comparison of previous Geant4 versions with a subset of data from Lockwood et al. was presented elsewhere [214, 215]. In this section, a brief overview of the considered experiments is given.

Lockwood et al. measured the relative electron energy and charge reflected from targets irradiated by electrons with kinetic energies between 0.1 and 1 MeV. In a few cases, measurements were also performed for incident

energies below 100 keV. Target materials examined by Lockwood et al. were Be, C, Al, Ti, Mo, Ta, and U. Longitudinal and lateral dimensions of absorber samples were generally larger than the range of incident electrons such that electron transmission was negligible. Measurements were conducted at 5 incident angles between 0° and 75° . The energy and charge reflected from the absorbers was determined indirectly, by taking the complement of energy deposition and current in the target. The target current I_t was obtained by keeping absorbers at a potential of approximately +55 V, which at the same time eliminated secondary electron emission into the backward hemisphere. By measuring simultaneously the incident current I_0 , Lockwood et al. determined backscatter coefficients according to

$$\eta_N = 1 - \frac{I_t}{I_0}. \quad (5.1)$$

The energy deposition in the targets was measured by means of a calorimetric technique. When deriving the relative energy backscatter η_E from the deposited energy, Lockwood et al. applied a correction accounting for the Bremsstrahlung energy leakage ε_γ from calorimeters. The corrections were based on simulations with the TIGER Monte Carlo code [223] (this transport code later become part of the previously mentioned Integrated TIGER Series (ITS) [224]). The fraction of backscattered electron energy was then calculated as

$$\eta_E = 1 - \frac{E + \varepsilon_\gamma}{E_0}, \quad (5.2)$$

where E_0 is the incident beam energy and E is the total energy deposition in the calorimeter. Similarly as for the measurements described in the previous chapter, beam energies deviated from nominal values in several cases.

All experimental data and Bremsstrahlung corrections obtained by Lockwood et al. are available in tabulated form in Ref. [216]. Experimental uncertainties of backscatter coefficients range from 5% in Al to 1% in high- Z targets (errors can be found in Ref. [217]). In the case of Be, where only a small fraction of incident electrons is reflected, the error is higher (26%). No experimental uncertainties were reported for calorimeters made of C. For all materials, the relative errors of η_E are equal or higher than errors of corresponding η_N (10% in Al and 1% in U). At oblique incidence, η_N and η_E are affected by an additional uncertainty as a result of the beam alignment. This error is quoted as 1–2% for measurements involving a tilt angle α of 60° .

Contrary to Lockwood et al., Tabata measured angular distributions of backscattered electrons as well as integral electron backscatter coefficients for 3.24–14.1 MeV beams normally incident on material samples made of Be, C, Al, Cu, Ag, Au, and U. In most measurements, the target thickness was

such that the number of reflected electrons reached a saturation level. In the Geant4 benchmarks presented in the following, only saturated backscatter data were considered for comparison. The experimental setup of Tabata included an evacuated scattering chamber, which contained the target assembly, and an ionization chamber for detecting backscattered electrons which passed a cone-shaped collimator. The ionization chamber response was calibrated using a Faraday chamber; calibrations were performed for beams with different energies incident on Au. By comparing the output of both detectors, Tabata deduced the multiplication factor of the ionization chamber as a function of the mean energy of backscattered electrons. This allowed to establish a relationship between the ionization chamber current and the number of electrons reflected into the respective solid angle. The quoted uncertainty of experimental backscatter coefficients and angular distributions obtained by Tabata ranges from $\sim 6\%$ to $\sim 14\%$.

In a recent paper, Kirihara et al. [222] showed that the multiplication factor assumed by Tabata is affected by a non-negligible error, which they attributed to Tabata's method of determining the mean energy of backscattered electrons for different target materials. Based on EGS5 Monte Carlo simulations, Kirihara et al. performed a recalculation of multiplication factors and backscatter coefficients for all materials and beam energies. In particular, factors were constructed in a way that they also accounted for low-energy electrons, which could not traverse the Al window of ionization chambers employed by Tabata. In most cases, the proposed correction yielded a higher backscatter coefficient; significant changes occurred particularly in low- Z absorbers such as Be and C. To account for these findings, updated backscatter coefficients from Kirihara et al. were adopted as reference in the Geant4 validation. Original data from Tabata were retained for completeness.

5.2.2 Monte Carlo simulation

Benchmarks were performed by means of a custom-made Geant4 application, linked against version 9.4 of Geant4 toolkit libraries. Absorbers were modelled as cylindrical disks of homogeneous composition. The target setup of Lockwood et al. was emulated by adjusting absorber dimensions according to the calorimeter size. An accurate rendering of the calorimeter dimensions was less important for the simulation of electron backscatter, but allowed for a more reliable estimate of the Bremsstrahlung leakage. The targets used in the experiments of Tabata were approximated by assuming an absorber thickness sufficient to obtain a saturation of electron backscatter coefficients. Target materials were assumed to contain no impurities. This imitates well target samples of Tabata, which were of high purity. As in the previous chap-

ter, the assumption of pure materials was also considered legitimate when modelling the calorimeters of Lockwood et al. as no details on material properties were reported. Employed densities and mean excitation energies are listed in Section A.1 of the Appendix. Incident electrons were assumed to impinge on targets in the form of pencil beams. The spatial and angular spread of electrons in the experiments was disregarded. At any tilt angle α , the beam axis intersected the front surface of the absorber model in its central point. Beams were assumed to be mono-energetic. Deviations from nominal beam energies encountered by Lockwood et al. were taken into account in the simulation.

To perform a comparison against the experiments of Lockwood et al., the kinetic energy and number of electrons reflected from absorbers was recorded and results were respectively divided by the incident kinetic energy and the number of incident particles. Simultaneously, Bremsstrahlung corrections were calculated such that TIGER-based values in Equation (5.2) could be substituted by Geant4 ones. More details on the replacement of original Bremsstrahlung corrections are presented in Section 5.2.5. To benchmark Geant4 simulations against measurements of Tabata, angular distributions of backscattered electrons were recorded on a hemisphere 100 cm in diameter and centered at the intersection point of beam axis and absorber. The rotational symmetry of the scoring setup with respect to the beam axis was exploited to increase the efficiency of the simulation. The hemisphere was segmented into 45 consecutive spherical sectors, each corresponding to a 2° polar angle (θ) interval. Results were normalized by dividing obtained scores by the solid angle $d\Omega$ and by the number of primary electrons. Total backscatter coefficients were derived by integrating $d\eta_N/d\Omega$ over the entire hemisphere.

The study benchmarked both electron multiple scattering models currently available in Geant4 (see Section 3.2.1), one being the semi-empirical model by Urbán used in the previous chapter and the second being the alternative model incorporating the Goudsmit-Saunderson angular distribution and the algorithm of Kawrakow and Bielajew for the spatial displacement. As discussed in Section 3.2.1, path length correction and step size limitations follow identical formalisms in both models. In the current study, the latest variant of the Urbán multiple scattering model, implemented in the `G4UrbanMscModel193` class, was used.

Ionization and Bremsstrahlung processes of electrons were described by means of the data-driven simulation models based on the EEDL cross sections. Correspondingly, interactions of secondary photons were included in the benchmark simulations using models based on the EPDL97 data sets.

5.2.3 Secondary particle production

In all simulations conducted in this study, the lower production threshold T_{cut} for secondary emission (δ -electrons and Bremsstrahlung photons) was set to 1 keV. This value introduces an artificial limit to the number of secondary electrons contributing to the simulated backscatter yield. In particular, a discrepancy remains between the adopted production threshold and the energy above which electrons could escape targets in the experiments of Lockwood et al. In another benchmark study, comparing EGSnrc simulations and experimental backscatter coefficients of keV electrons, Ali and Rogers [198] estimated the systematic uncertainty due to such a discrepancy to be less than 2%. On the other hand, the employed production threshold is consistent with corrected backscatter coefficients proposed by Kiriwara et al. as they applied the same threshold when recalculating multiplication factors with EGS5.

5.2.4 Transport parameter settings

It was demonstrated in previous Geant4-based studies [28, 148, 149, 194] that calculations of backscatter coefficients for keV electrons exhibit a dependency on the multiple scattering model parameter f_r (see Equation 3.1); smaller f_r values (≤ 0.02) generally improved the accuracy of backscatter simulations. Accounting for this observation, f_r was set to 0.01 in the current study; this value is smaller than the default one ($f_r=0.04$) used in the employed Geant4 release [67]. The choice of f_r proved to be relevant only at lower energies, whereas little dependency on f_r was observed at 1 MeV or higher energies (at higher energies, steps were increasingly dominated by the occurrence of discrete interactions). For illustration, Fig. 5.1 presents the ratio of simulated and measured [216, 217] backscatter coefficients η_N as a function of f_r for 0.109 MeV electrons normally incident on Ti and Ta. The gray band displayed in the plot reflects the uncertainty of the experiment.

As discussed in the previous chapter, the step limitation imposed by the electron energy loss algorithm can be important when studying spatial dose distributions in extended, homogeneous media (see also [152]), but proved to be less relevant in current backscatter simulations as steps of electrons contributing to the backscatter yield were sufficiently restricted by other mechanisms. Parameter settings used in the current simulations were 100 μm for ρ_R and 0.2 for α_R (see Equation 3.3).

Single scattering near material interfaces was activated in all benchmark simulations by employing the “UseDistanceToBoundary” stepping option [147]. With this option, single scattering is applied within a distance

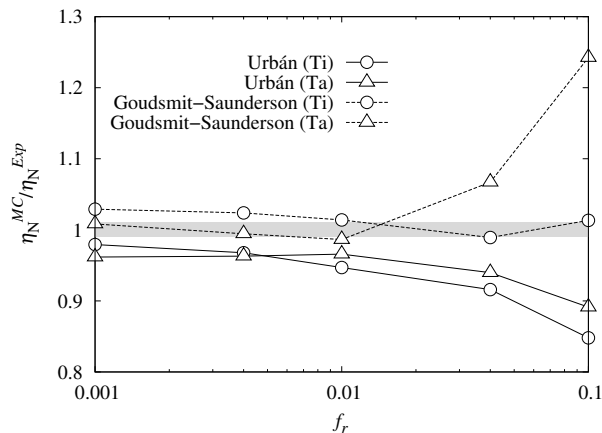


Figure 5.1: Ratio of calculated and measured [216, 217] electron backscatter coefficients η_N^{MC} and η_N^{Exp} vs the stepping parameter f_r for 0.109 MeV electrons normally incident on Ti and Ta. Simulations were performed using respectively the Urbán multiple scattering model (solid lines) and the alternative Geant4 model based on the Goudsmit-Saunderson angular distribution (dashed lines). The gray band indicates the experimental uncertainty.

$skin \times \lambda_{elastic}$ from a volume surface. Varying the $skin$ parameter between 1 and 3 showed no significant impact on the electron backscatter coefficient, and hence $skin$ was arbitrarily set to 3 in all simulations.

5.2.5 Bremsstrahlung correction

As discussed in Section 5.2.1, the experimental method adopted by Lockwood et al. for measuring η_E required a correction accounting for the energy fraction escaping from calorimeters in the form of Bremsstrahlung. For the purpose of the benchmark, original Bremsstrahlung corrections were substituted by corresponding Geant4-based results. With few exceptions, corrections obtained with Geant4 were systematically larger than predictions of the TIGER code reported by Lockwood et al. Discrepancies up to a factor of ~ 2 were observed between the two code systems. The differences are illustrated in Fig. 5.2, showing Geant4 and TIGER-based Bremsstrahlung corrections versus energy for electron beams normally incident on different calorimeters. The corrections displayed in the figure are expressed as a fraction of the incident energy.

A possible source of the disagreement between Geant4 and TIGER are different sets of Bremsstrahlung cross sections used in both code systems.

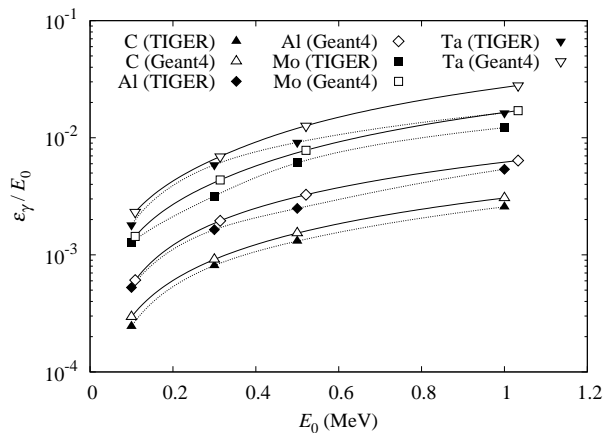


Figure 5.2: Fraction of the incident electron energy escaping from calorimeters (C, Al, Mo, and Ta) as Bremsstrahlung energy: comparison of TIGER calculations [216, 217] (full symbols) against Geant4 9.4 results (open symbols). The incident angle is 0° . Data points are joined by lines to guide the eye. The statistical error of TIGER-based results is $<10\%$ for $\varepsilon_\gamma/E_0 > 0.005$, and $>10\%$ for $\varepsilon_\gamma/E_0 < 0.005$ [216]. The statistical error of Geant4 results is $<4\%$.

The EEDL cross sections employed in Geant4 are based on the formulations of Seltzer and Berger [225, 226], who quote an uncertainty of 5–10% for energies between 1 keV and 2 MeV [160]. The Seltzer-Berger cross sections are considered more accurate than the Bremsstrahlung cross sections used in early versions of the Integrated TIGER Series [101]. This supports the use of Geant4-calculated Bremsstrahlung corrections over TIGER-based ones. The new correction alters experimental η_E by up to 4%. Relevant changes occur only at higher energies and small incident angles since the relative contribution of ε_γ/E_0 to η_E rapidly decreases with decreasing E_0 or increasing tilt angle α .

5.3 Results and discussion

Monte Carlo simulations were performed for a representative subset of experimental configurations. For each case, the number of primary particle histories simulated was between 1×10^6 and 4×10^6 , resulting in statistical errors $<1\%$ and $<3\%$ for backscatter coefficients of 0.1–1 MeV and 3.2–14.1 MeV electrons, respectively. Energy albedos η_E obtained in the simulations are affected by a statistical error slightly larger than the uncertainty of corre-

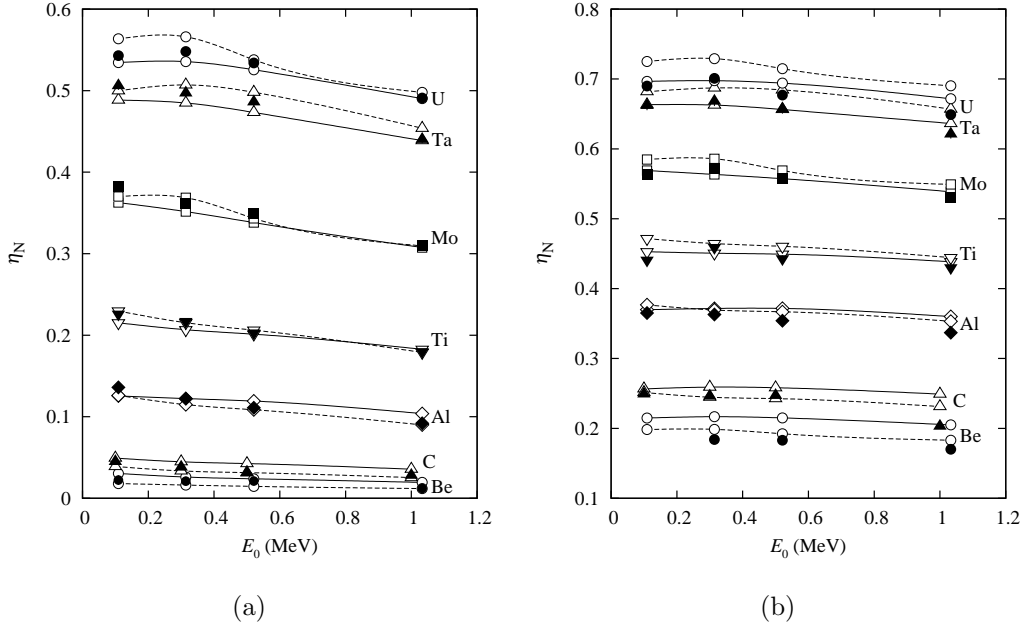


Figure 5.3: Electron backscatter coefficients η_N as a function of beam energy E_0 , for beams incident at (a) 0° and (b) 60° , respectively. Exceptionally, in the case of Be, incident angles are 1° and 61° . Geant4 9.4 results (open symbols) are compared against experimental data from Lockwood et al. [216, 217] (full symbols). Simulations were based on different Geant4 multiple scattering models employing the semi-empirical formulation by Urbán (solid lines) and the Goudsmit-Saunderson angular distribution (dashed lines). Where not indicated by vertical bars, experimental errors are smaller than the symbols representing the data (no errors were reported for C). The experimental uncertainty of the beam alignment at 60° (61°) is not included in the error bars.

sponding backscatter coefficients. The statistical uncertainty of calculated angular distributions of backscattered electrons is $<5\%$, except for very small or very large backscattering angles. In all cases, the statistical error of Monte Carlo results is significantly smaller than the experimental uncertainty. Simulation uncertainties are not displayed in figures for the sake of clarity.

5.3.1 Backscattering of electrons with energies between 0.1 and 1 MeV

Fig. 5.3 displays simulated and measured [216, 217] electron backscatter coefficients η_N as a function of the beam energy. Results are presented for different target Z , and for normal and 60° incidence. Conversely, Fig. 5.4

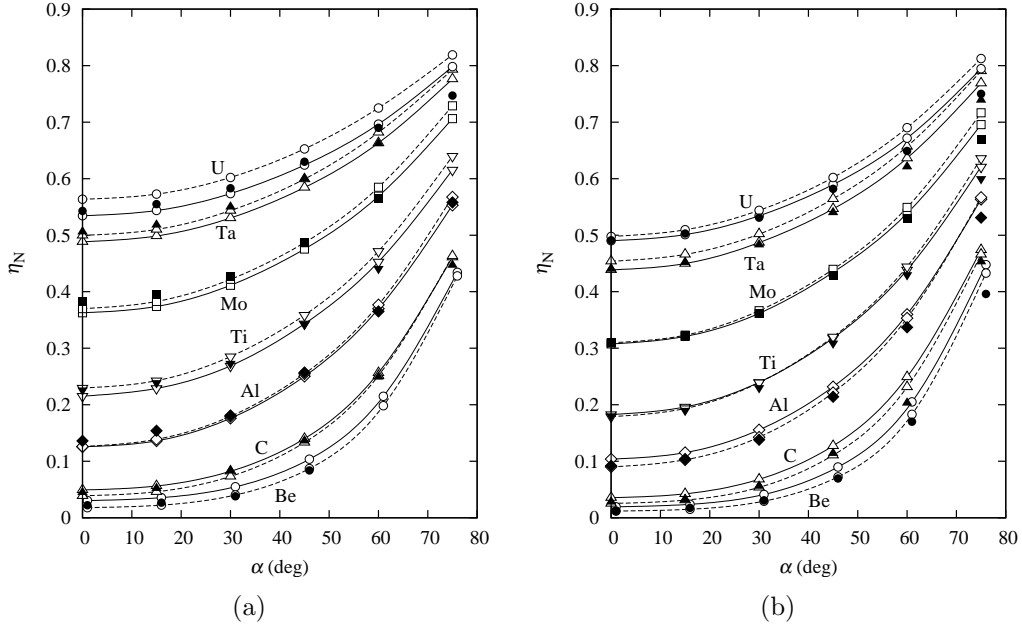


Figure 5.4: Electron backscatter coefficients η_N vs angle of incidence for (a) 0.109 MeV and (b) 1.033 MeV electrons. Exceptionally, in the case of C, the beam energy E_0 is 0.100 MeV and 1.000 MeV. Geant4 9.4 results (open symbols) are compared against experimental data from Lockwood et al. [216, 217] (full symbols). Simulations were based on different Geant4 multiple scattering models employing the semi-empirical formulation by Urbán (solid lines) and the Goudsmit-Saunderson angular distribution (dashed lines).

shows η_N versus the incident angle for energies of ~ 0.1 and ~ 1 MeV. Both figures display Monte Carlo predictions respectively obtained with the Urbán multiple scattering model and the alternative Geant4 model based on the Goudsmit-Saunderson theory. Simulation results are joined by lines for visual clarity.

In the energy range considered, the relative backscatter yield exhibits only a moderate variation with the beam energy E_0 (see Fig. 5.3). At the same time, η_N is a monotonically increasing function of the target Z (Figs. 5.3 and 5.4) and the incident angle α (Fig. 5.4). The Monte Carlo simulations generally reproduce experimental backscatter coefficients and their dependency on E_0 , α and Z reasonably well. For medium- and high- Z targets ($Z \geq 22$), calculations based on the Urbán multiple scattering model match experimental backscatter coefficients within 6% at normal incidence, and within 4% at 60° incidence. A similar agreement is found for simulations employing the model based on the Goudsmit-Saunderson theory, which

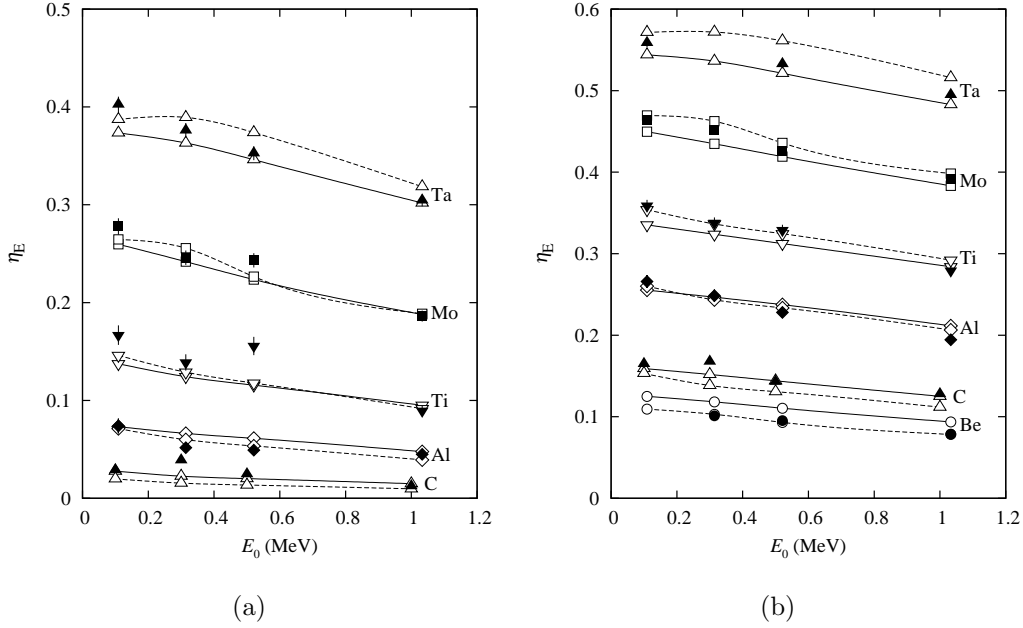


Figure 5.5: Ratio η_E of backscattered and incident kinetic energies as a function of beam energy E_0 , for beams incident at (a) 0° and (b) 60° , respectively. Exceptionally, in the case of Be, incident angles are 1° and 61° . Details as in Fig. 5.3.

reproduce measured η_N (for $Z \geq 22$) with an accuracy better than 4% at $\alpha = 0^\circ$, and better than 7% at $\alpha = 60^\circ$. The relative difference between calculated and experimental η_N tends to be larger in the case of lighter targets ($Z \leq 13$), particularly for beams at normal incidence. In contrast to higher- Z materials, experimental backscatter coefficients of low- Z samples shown in Figs. 5.3 and 5.4 are affected by a larger uncertainty as the precision of the measurement technique is approximately proportional to $(1 - \eta_N)^{-1}$ [216, 217]. Similarly, the experimental uncertainty increases with decreasing angle α . The reduced experimental precision poses a constraint for obtaining a more accurate assessment of the simulation accuracy for low- Z targets and small incident angles.

Figs. 5.5 and 5.6 display simulated and measured [216, 217] fractions η_E of the incident energy backscattered from targets. Experimental energy albedos for U were found to be significantly underestimated in the simulation at all energies and incident angles. Judging from previous Monte Carlo studies [191, 216, 219], this discrepancy is likely due to a systematic error in the experiment. The energy albedo measurements for U were hence not

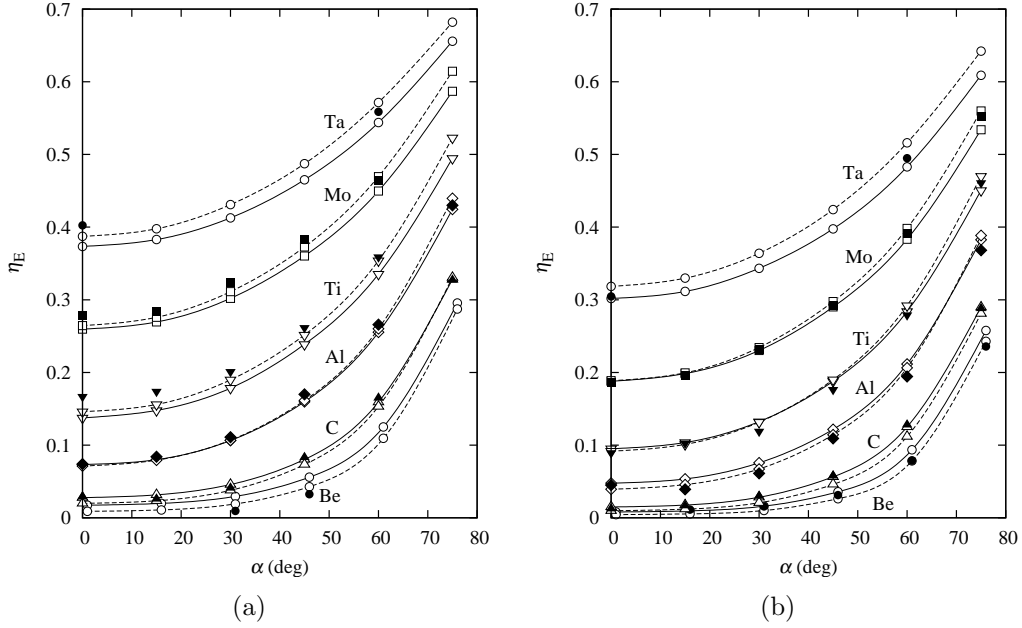


Figure 5.6: Ratio η_E of backscattered and incident kinetic energies vs angle of incidence, for (a) 0.109 MeV and (b) 1.033 MeV electrons. Exceptionally, in the case of C, the beam energy E_0 is 0.100 MeV and 1.000 MeV. Details as in Fig. 5.5.

considered reliable for a validation of Monte Carlo models and were excluded from the comparison.

Similar to the case of backscatter coefficients, Geant4 simulations of energy albedos are in good agreement with experimental data for high- Z materials, but exhibit larger discrepancies with measurements for low- Z samples. The relative differences between calculated and measured energy backscatter in higher- Z targets such as Mo and Ta are comparable to those determined for η_N . No systematic discrepancies across different materials are observed identifying one of the multiple scattering models to be preferable over the other.

5.3.2 Backscattering of electrons with energies between 3 and 14 MeV

Fig. 5.7 compares Geant4-calculated with measured backscatter coefficients η_N for electrons normally incident on semi-infinite targets with different Z . Results are presented as a function of beam energy E_0 . As in the previous

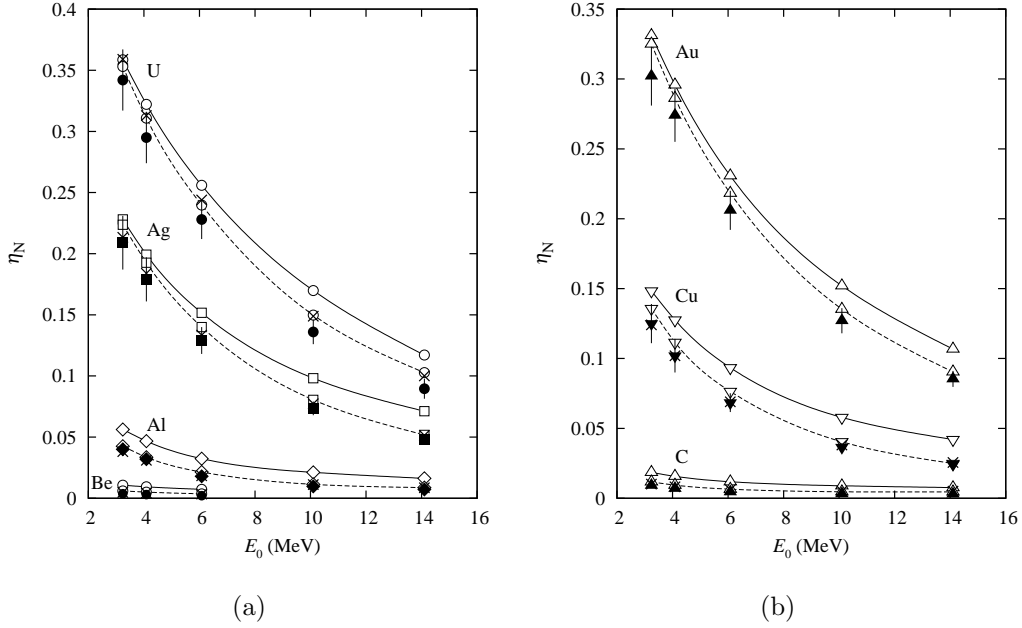


Figure 5.7: Electron backscatter coefficients η_N vs beam energy E_0 for electrons normally incident on (a) Be, Al, Ag, U and (b) C, Cu, and Au. Geant4 9.4 results (open symbols) are compared against experimental data from Tabata [218] (full symbols) and corrected backscatter coefficients proposed by Kirihara et al. [222] (crosses). The corrections apply to all data points, except to those corresponding to Au. Simulations were based on different Geant4 multiple scattering models employing the semi-empirical formulation by Urbán (solid lines) and the Goudsmit-Saunderson angular distribution (dashed lines), respectively. Vertical bars indicate the experimental uncertainty.

section, the plots show two sets of Monte Carlo results respectively based on alternative multiple scattering models. Calculated backscatter coefficients are joined by lines to guide the eye. In addition to the experimental data by Tabata [218], Fig. 5.7 displays corrected backscatter coefficients proposed by Kirihara et al. [222]. The corrections apply to all data points, except to those corresponding to Au, which were separately measured by means of a Faraday cup [218].

Backscatter coefficients shown in Fig. 5.7 decrease monotonically with beam energy E_0 , reaching values significantly lower than those of 0.1–1 MeV electrons presented in the previous section. Considering the experimental uncertainty, simulations employing the Goudsmit-Saunderson theory-based model compare well with experimental backscatter coefficients; for materials with $Z \geq 47$, the difference between simulation results and corrected coeffi-

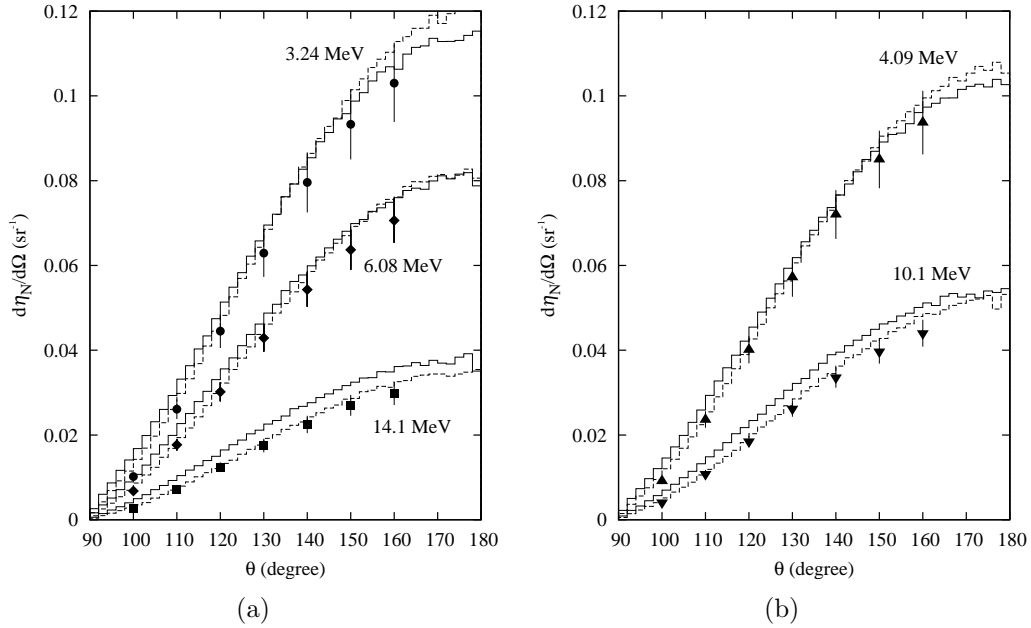


Figure 5.8: Differential backscatter coefficients vs the detector angle for 3.24–14.1 MeV electrons normally incident on Au. Comparison of Geant4 9.4 results (histograms) against experimental data from Tabata [218] (full symbols). Simulations were based on different Geant4 multiple scattering models employing the semi-empirical formulation by Urbán (solid lines) and the Goudsmit-Saunderson angular distribution (dashed lines), respectively. Vertical bars indicate the experimental uncertainty.

coefficients from Kirihara et al. (respectively original data from Tabata for Au) is less than 8%. Discrepancies are found to be partly larger for lighter targets, particularly in case of Be, where predictions of the simulation model and data of Kirihara et al. disagree by up to 26%. The Urbán multiple scattering model has a tendency to yield backscatter coefficients which are in most cases higher than the data from Tabata and Kirihara et al. The largest discrepancies occur for Be, where calculated backscatter coefficients are roughly twice as large as experimental values.

Complementing the comparison of total backscatter coefficients, Fig. 5.8 shows Geant4-based and experimental [218] angular distributions of 3.24 to 14.1 MeV electrons backscattered from a semi-infinite Au target. Simulation predictions based on the Goudsmit-Saunderson model reproduce measured distributions with good accuracy; with few exceptions, obtained results match experimental angular spectra within their quoted uncertainty. As expected from results presented in Fig. 5.7, the agreement is less satisfactory for

simulations based on the Urbán modelling approach; with increasing beam energy, calculated angular distributions appear to be gradually higher than the measurement data.

5.4 Conclusions

This study systematically examined the accuracy of Geant4 electron transport algorithms for simulating backscattering of electrons from solid targets. Simulation predictions were compared against published experimental backscatter coefficients, energy albedos, as well as angular distributions of reflected electrons. The study benchmarked two alternative multiple scattering models, respectively employing the semi-empirical formulation by Urbán and the Goudsmit-Saunderson theory. To achieve maximum accuracy, the multiple scattering parameter f_r was set to 0.01. Using the default value 0.04 increases the systematic error of backscattering coefficients by up to $\sim 20\%$ below 1 MeV, and by up to $\sim 5\%$ at 1 MeV and above. The model by Urbán was found to reproduce experimental data reasonably well at lower energies (~ 0.1 –1 MeV), but tended to overestimate measured backscatter coefficients at higher energies (~ 3 –14 MeV). Simulations employing the alternative multiple scattering model, based on the angular distribution of Goudsmit and Saunderson, were found to be in reasonable agreement with experimental measurements in the entire energy range under study. The best agreement was observed for higher- Z targets while comparably larger discrepancies were found for low- Z targets such as Be and C, where the backscatter yield is significantly lower and experimental data were partly affected by larger errors.

The results demonstrate the predictive ability of the Geant4 toolkit for simulation scenarios requiring a quantitative knowledge of electron backscatter phenomena. Particle energies covered in this chapter are of particular interest for applications in radiotherapy, but are also fundamental to a variety of other scenarios, including simulations of sampling calorimeters in high energy physics experiments; shielding calculations for electronic devices used in space applications; and β -spectroscopy as applied in nuclear physics experiments. Further validation studies are required to establish the accuracy of the Geant4 code for energies beyond the range covered in this chapter, in particular in the energy regime below 100 keV. The simulation software developed for this study allows to perform regular comparisons of new Geant4 versions with electron backscattering data.

Chapter 6

Validation study of ion dose distributions in phantom materials

The advantages of patient irradiation with energetic carbon ions as a means of cancer treatment have been much discussed in the literature (see, for example, Refs. [8, 9]). One of the most well-known characteristics of ion penetration into matter is the longitudinal energy deposition pattern, exhibiting a steep maximum (the “Bragg peak”) prior to particle stopping. In view of a conformal dose delivery to a defined volume, as generally sought in patient treatment [227], carbon ions show a more favourable behaviour than protons due to a reduced lateral scattering and longitudinal straggling, but also due to an increased relative biological effectiveness [9]. On the other hand, light fragments from inelastic nuclear reactions of ions with target atoms can propagate to depths exceeding the position of the Bragg peak, hence causing a typical dose tail. This poses a disadvantage in ion therapy. Also, fragmentation reactions increase the complexity of ion beam transport modelling and dosimetric calculations.

A fundamental aspect of dose calculations in ion therapy is the accurate prediction of Bragg peak positions based on an adequate description of the electronic energy loss of ions. This chapter¹ presents the integration of state-of-the-art stopping powers into the Geant4 toolkit. The accuracy of the implementation is evaluated by comparing simulations against published measurements of dose distributions induced by ^{12}C beams in typical phantom materials. The study also examines the performance of different Geant4

¹The content of this chapter formed the basis of the following paper: A. Lechner, V.N. Ivanchenko, J. Knobloch, “Validation of recent Geant4 physics models for application in carbon ion therapy”, Nucl. Instr. and Meth. B 268 (2010) 2343–2354.

generators for projectile fragmentation by investigating proportional features of dose distributions.

6.1 Introductory aspects, previous studies and outline

An accurate description of the spatial energy deposition pattern is a key point in Monte Carlo-based ion dosimetry. Electromagnetic modelling features are considerably contributing to the Bragg peak shape and position. In this chapter, a plug-in model, newly implemented in Geant4 (version 9.3), is presented, which enables the use of external stopping powers to describe the electronic energy loss of ions. In its default configuration the model utilizes tables from the ICRU 73 report [36] and includes recent revisions of ICRU 73 stopping powers by Sigmund et al. [37], which have not yet been employed in a Monte Carlo system. The main objective of this study is to examine the accuracy of the energy loss model for simulating light-ion transport in tissue-like media. Investigations also involve a comparison against conventional Geant4 stopping power algorithms, which incorporate an effective ion charge [166].

The presented validation focuses on the simulation of depth-dose profiles of ^{12}C beams incident on water and polyethylene. Water is the most widely used tissue substitute and reference material in radiotherapy studies. Polyethylene, $(\text{C}_2\text{H}_4)_n$, is also employed as a phantom material and is commonly used for shielding purposes in space applications. In the current validation setup different beam energies relevant to radiotherapeutical applications are considered (from 90 MeV/u up to 400 MeV/u). Computed profiles are compared against experimental data available in the literature aiming to reproduce the Bragg peak position as well as shapes of the dose distributions.

Monte Carlo-based carbon ion Bragg peaks, and their comparison against measured profiles, have been reported by different authors (see for example [104, 129, 228]), addressing also Geant4-based profiles [134, 229–231]. However, only few authors note if the underlying experiments are suitable for a benchmark of the absolute peak position in the considered target material and most studies do not account for associated experimental errors. In some papers simulated profiles are shifted to match the experimental curves in the vicinity of the peak. Hence, to execute a detailed examination of simulation models, the study is restricted to experimental distributions which allow for a high-precision validation of the Bragg peak position. Particular

attention is paid to corresponding experimental uncertainties: the employed data sets permit a sub-millimeter analysis concerning the location of the peak. Complementing the investigations on the peak position, a systematic and quantitative comparison of proportional features of the Bragg curves is conducted.

Some of the experimental data used in the current work (from Sihver et al. [232] and Haettner et al. [233]) have been employed by other authors in previous evaluations of analytical beam models and Monte Carlo codes; comparisons were also performed against older versions of Geant4 by Pshenichnov et al. [229, 230]. However, since then the Geant4 toolkit has been subject of evolution and several physics models and methods have been added or improved. Specific attention is paid to some of the recent modelling approaches, in particular to the ICRU 73-based energy loss model and the native Geant4 quantum molecular dynamics (QMD) generator for light ion fragmentation.

The chapter is organized as follows. An overview of electronic energy loss algorithms for ions in Geant4 is given in Section 6.2. Section 6.3 presents details of the validation setup, including characteristics of the simulation configuration and a description of experimental data sets. Section 6.4 presents results and discussions. Conclusions are given in Section 6.5.

6.2 Electronic energy loss of ions

As briefly discussed in Section 3.2.1, the Geant4 toolkit includes physics algorithms allowing the simulation of the energy loss of protons and ions due to interactions with atomic shells of absorber atoms or molecules. As of version 9.3, the corresponding physics processes are implemented in the C++ class `G4hIonisation` for protons, deuterons and tritons, and in the class `G4ionIonisation` for all other ions. These classes are configurable with models which compute electronic stopping powers, energy loss fluctuations, and cross sections for the production of δ -electrons [27]. A description of original Geant4 stopping power algorithms as well as new parameterizations is given in the following (Sections 6.2.1 and 6.2.2, respectively), complemented by a discussion of stopping powers available in the literature (Sections 6.2.3) and aspects related to the mean ionization potential (Section 6.2.4).

6.2.1 Geant4 “Standard” stopping power algorithms

By default, the `G4ionIonisation` class uses stopping power models [166] of the Geant4 “Standard Electromagnetic Package”. Below a defined threshold energy, currently set to 2 MeV/u, a parameterization formula is employed.

Above the threshold energy, the restricted energy loss rate of ions with energy E is calculated according to

$$S_{c,ions}(E, T_{cut}) = z_{ion}^2 S_{c,p}(E_s, T_{cut}) + F(E, z_{ion}) + G(E), \quad (6.1)$$

where G is a correction term which enables a smooth transition to the low-energy parameterization at the threshold energy and decreases with increasing energy. The second term, F , includes Barkas, Bloch and Mott corrections, which are proportional to higher orders of z_{ion} ; corresponding terms originate from [234–236], where the Barkas term relies on minimum-impact parameters from ICRU 49 [237]. The ion charge z_{ion} is calculated as $z_{ion} = \gamma Z_{ion}$, where Z_{ion} is the atomic number of the ion and γ is the fractional effective charge computed according to a parameterization formula of Ziegler et al. [238] for He ions, and according to the theory of Brandt and Kitagawa [239] for ions with $Z_{ion} \geq 3$. Further, $S_{c,p}$ is based on the restricted Bethe formula for protons in Ref. [240], and includes a shell correction term C from ICRU 49 [237] and a correction δ accounting for the density effect according to Sternheimer and Peierls [241]:

$$S_{c,p} = 2\pi r_e^2 m_e c^2 \frac{n_{el}}{\beta^2} \times \left[\ln \left(\frac{2m_e c^2 \beta^2 T_{cut}}{(1 - \beta^2) I^2} \right) - \beta^2 \left(1 + \frac{T_{cut}}{T_{max}} \right) - \delta - 2 \frac{C}{Z} \right]. \quad (6.2)$$

Here, r_e is the classical electron radius, m_e is the electron rest mass, β is the ratio of particle velocity and speed of light c , n_{el} is the electron density of the material, and Z and I are the atomic number and the mean excitation energy of the material, respectively. As in the previous chapters, T_{cut} indicates the secondary production threshold, whereas T_{max} represents the maximum energy which can be imparted to a secondary electron. To obtain the energy loss rate of ions according to Equation (6.1), $S_{c,p}$ is evaluated at the scaled energy $E_s = EM_p/M_{ion}$, where M_p and M_{ion} are the proton and ion mass, respectively. More details on “Standard” algorithms are elaborated in the publication of Bagulya et al. [166]. A description of recent updates was given by Apostolakis et al. [27].

6.2.2 Implementation of a new parameterization model

A new Geant4 parameterization model was developed allowing to employ external stopping power tables for Geant4 ion transport simulations. Based on these tables, the model computes the average energy loss projectiles experience in sub-threshold interactions, i.e. in continuous interactions below

T_{cut} . In addition, it accounts for the discrete energy loss as a consequence of catastrophic collisions, where energy is imparted to δ -electrons, and it samples the ejection angle of secondaries. The simulation model is applicable for ion species represented by the Geant4 “generic ion” particle type which comprises all nuclei except tritons, deuterons, ^3He and ^4He . The model is part of the “Low-Energy Electromagnetic Package” and its implementation follows the software design adopted by the Geant4 “Standard” package such that model algorithms are compatible with the `G4ionIonisation` class. It is remarked that previous algorithms of the “Low-Energy Electromagnetic Package”, described in [167], are not discussed here.

For an ion with kinetic energy E , propagating in a material of density ρ_t , the restricted energy loss per unit path length is calculated according to

$$S(E, T_{cut}) = \rho_t (S/\rho)^{Table}(E) - S_\delta(E, T_{cut}), \quad (6.3)$$

where $(S/\rho)^{Table}$ refers to mass stopping powers obtained by interpolating the tabulated values using a cubic spline algorithm [166]. If mass stopping powers are not available for a compound material but only for its elemental constituents, Bragg’s additivity rule [237] is applied to calculate the first term in the above equation:

$$\rho_t (S/\rho)^{Table}(E) = \sum_i w_i (S/\rho)_i^{Table}(E). \quad (6.4)$$

Here, the index i runs over all elements composing the material, w_i is the weight fraction of element i , and $(S/\rho)_i^{Table}$ is the tabulated mass stopping power of the i th constituent. The second term in Equation (6.3), S_δ , denotes the mean energy transferred to δ -electrons per unit path length given by

$$S_\delta(E, T_{cut}) = \sum_i n_i \int_{T_{cut}}^{T_{max}} \frac{d\sigma_{\delta,i}(E, T)}{dT} T dT, \quad (6.5)$$

where the index i considers again all elemental constituents, n_i is the number of atoms of element i per volume, T_{cut} is the lower δ -production threshold, T_{max} is again the maximum energy which can be transferred from projectiles to δ -electrons in a single collision, and $d\sigma_{\delta,i}/dT$ is the differential δ -production cross section corresponding to the interaction of projectiles with atoms of element i . S_δ decreases with increasing T_{cut} and vanishes when T_{cut} becomes equal to or larger than T_{max} .

Algorithms governing the ejection of δ -rays in the simulation model are equivalent to the ones used in previous Geant4 models [166]. The description of ion–electron collision processes is based on the approximation that projectiles interact with quasi-free electrons. This assumption is valid if T_{cut} is much

larger than the mean excitation energy I of the absorber material [240, 242]. For a given simulation step, the actual energy T of a secondary electron is sampled from differential collision cross sections, $d\sigma_\delta/dT = \sum_i n_i (d\sigma_{\delta,i}/dT)$, restricted to the energy range between T_{cut} and T_{max} . For an ion with charge z_{ion} and incident energy E , the differential cross section $d\sigma_{\delta,i}/dT$ can be written as [240, 242]

$$\frac{d\sigma_{\delta,i}}{dT} = 2\pi r_e^2 m_e c^2 \frac{z_{ion}^2 Z_i}{\beta^2} \frac{1}{T^2} \left[1 - \beta^2 \frac{T}{T_{max}} + \frac{T^2}{2E^2} \right], \quad (6.6)$$

where Z_i is the atomic number of the i th element composing the target medium. The ion charge z_i is calculated as described previously. If a secondary is created, its energy is considered as discrete energy loss of the projectile, introducing in a natural way loss fluctuations.

6.2.3 Stopping powers in the literature and their use in Geant4

Several approaches describing ion stopping powers have emerged in the literature, covering ion-material combinations and energy ranges pertinent to ion therapy. It is out of the scope of this study to provide a complete overview beyond the discussion of a few examples. A more comprehensive treatment of the subject, including listings of recent codes and tabulations, can be found, for example, in the ICRU 73 [36] report or in other references like [243, 244].

Well-known semi-empirical stopping power approaches are MSTAR [245–247] and SRIM [248]. Among the most recent theoretical means to describe electronic stopping of ions are the binary theory of Sigmund and Schinner [249], which entered the PASS code [250], and the theory of Grande and Schiwietz [251, and references therein], which is available in the CasP code [252]. Stopping power tables pre-calculated with PASS are also published in the ICRU 73 report. The report considers projectiles ranging from Li to Ar and also includes Fe ions due to their importance in some fields; tables are presented for many elemental materials and compounds. Kinetic energies covered by the ICRU 73 report start at 250 keV/u and extend to 1 GeV/u.

As of version 9.3, all ICRU 73 tables are available in the Geant4 release and can be employed in the simulation by means of the plug-in model presented in the previous section (however the applicability of the model is not restricted to ICRU 73 data and any other stopping power table can be plugged in). For a few target materials, revisions of ICRU 73 stopping powers from Sigmund et al. [37] were included, which replace the original ICRU 73 tables in the Geant4 database. Affected materials are, for example, water

Ion atomic number	Material	Origin of tables	Remarks
3–18, 26	25 elements, 31 compounds	ICRU 73 [36] (PASS)	
3–18, 26	water, water vapor	Revised ICRU 73 [37] (PASS)	Replace original ICRU 73 tables
9	nylon types 6/6 and 6	Corrected ICRU 73 [37] (PASS)	Replace original ICRU 73 tables
26	water	Personal communication with P. Sigmund (PASS)	Complement ICRU 73 tables
3–18, 26	copper	Personal communication with P. Sigmund (PASS)	Replace original ICRU 73 tables

Table 6.1: Electronic stopping power tables included in the Geant4 “Low-energy” electromagnetic data directory (G4EMLOW) version 6.8 or higher (to be used with Geant4 release version 9.3 or higher). These tables are employed by the newly implemented energy loss model for ion transport at projectile energies between 250 keV/u and 1 GeV/u.

and water vapor. Owing to their importance in radiotherapy studies, a brief summary of changes related to ICRU 73 stopping powers of water is given in the next section. An overview of all stopping powers incorporated by the Geant4 simulation model is presented in Table 6.1.

6.2.4 The I -value of water and revised ICRU 73 tables

In the context of proton or light-ion stopping powers and their application to hadron therapy, the role of the mean excitation energy of water has gained substantial attention in the literature, particularly in view of projectile ranges (see, for example, Refs. [232, 253, 254]) or water-to-air stopping power ratios [130–132, 255]. In contrast to various other stopping power programs, the PASS code does not rely directly on I -values. Instead, it requires oscillator-strength spectra of target atoms or molecules as input [36, 250], but evidently these spectra imply a mean excitation energy [37].

The I -value associated with the oscillator-strength spectrum of water in the ICRU 73 report is 67.2 eV [37, 255], which is significantly lower than mean excitation energies suggested in ICRU 49 (75.0 eV) or in more recent publications (for example 77.8±1 eV in Ref. [256], 78.0±1 eV in Ref. [257] or 80.8±2 eV in Ref. [131]). This has been discussed many times in the literature [130–132, 253–255, 258].

The inability of the ICRU 73 tables for water to reproduce experimentally derived ranges was first indicated by Paul [253], who compared the range of

^{12}C ions in continuous slowing down approximation (CSDA) against values extracted from depth-dose profiles of Sihver et al. [232]: as demonstrated by Paul [253], ICRU 73 stopping powers yield a CSDA range which is $\approx 1.5\text{--}2\%$ smaller than results from experiments. This finding was mainly attributed to the adopted oscillator-strength spectrum. Sihver and Mancusi [259] also noted the underprediction of experimental ranges.

Recently, Sigmund et al. [37] published PASS stopping powers for liquid water, based on an adapted oscillator-strength spectrum. As for the original ICRU 73 tables, oscillator strengths and excitation energies of inner shells were taken from molecular oxygen. However, valence shell properties were determined by enforcing a mean excitation energy of 78.0 eV (following the I -value obtained by Schardt et al. [257]). The revised input spectra reduce the stopping powers compared to values originally published by ICRU: for carbon ions, the difference is $\approx 1.8\%$ at 200 MeV/nucleon, $\approx 2.6\%$ at 10 MeV/nucleon and $\approx 6.8\%$ at 250 keV/nucleon (which is approximately the energy where maximum stopping occurs).

For convenience, in further discussions involving water stopping powers, tables from ICRU 73 will be denoted as “original ICRU 73” tables, whereas stopping powers from Sigmund et al. [37] will be referred to as “revised ICRU 73” tables. Stopping powers of other materials, which also derive from Ref. [36], are simply named ICRU 73 stopping powers.

6.3 Materials and methods

To validate the parameterization model presented in the previous section, depth-dose profiles were computed and compared against measured distributions available in the literature. This section presents experimental data used in the validation and gives details about the adopted simulation setup. All calculations were performed with version 9.3 of the Geant4 toolkit. It is emphasized, that the current study does not cover the full spectrum of physics modelling approaches in Geant4. Particularly for secondary particles, several alternative models are available (see Section 3.2).

6.3.1 Experimental depth-dose profiles

Experimental data used in the Monte Carlo validation derive from the publications of Sihver et al. [232], Schardt et al. [257], Haettner et al. [233] and Weber [260]. These authors presented measurements of 90–400 MeV/u ^{12}C beams incident on water and polyethylene targets. All the experiments described have in common that dose profiles were measured by placing ion-

isation chambers up- and downstream of a target of adjustable length. The variation of dose with depth could be determined by recording the relative ionisation of the chambers for different target thicknesses.

In the selection of experimental data sets from the specified references, particular attention was given to the position of the Bragg peak and the related uncertainty of the measurement. In all mentioned experimental studies, dose profiles were presented by specifying absolute depths in the actual target material. This was achieved by accounting for the range shift due to all materials (other than the target) traversed by the beam after leaving the vacuum of the accelerator. Peculiarities and techniques adopted in the different publications are briefly discussed in the following. For more details the reader is referred to the specified references.

Sihver et al. reported experimental depth-dose distributions in water induced by relativistic ^{12}C , ^{18}O and ^{20}Ne beams. The corresponding measurements were performed at GSI (Germany) and RIKEN (Japan). The dose profiles were used in several papers reporting the comparison against Monte Carlo codes, for example against FLUKA [228], Geant4 [229] and SHIELD-HIT [104]. However, not all curves published by Sihver et al. allow for a high-precision validation of the absolute Bragg peak position in water. Only for two beam configurations (195 and 270 MeV/u carbon ions), was the peak position precisely determined by measuring the water equivalent thickness (WET) of beamline equipment (the WET of a material in the beam path corresponds to the thickness of a water layer which would lead to the same ion range in the actual water target): based on the experimentally derived WET of components like ionization chambers, the vacuum exit window or the entrance and exit walls of the water container, and also of air gaps traversed by the beam, the absolute Bragg peak position in water could be deduced. The error of the obtained position was specified as $\pm 0.04 \text{ g/cm}^2$.

For all other depth-dose profiles presented by Sihver et al., materials in the beam path were considered by calculating the WET using the stopping power code ATIMA [261]. However, not all material properties could be incorporated in detail into WET calculations. The largest error occurred due to deformations of the walls (made of Lucite) of the water absorber (from personal communication with D. Schardt, 2009). Hence, in the current study only Bragg peaks corresponding to the 195 and 270 MeV/u ^{12}C beams are considered for comparison.

More recently, high-precision measurements of light ion (^1H up to ^{16}O) Bragg curves in water were reported by Schardt et al. The experiments were performed at GSI and included the measurement of the WET for all materials in the beam path. When the current study was carried out, final data sets were not available, but the Bragg peak positions for 200 and 400 MeV/u ^{12}C

beams were communicated to the author of this work by D. Schardt; the error corresponding to the peak positions was determined as $\pm 0.01\text{--}0.02$ g/cm².

Experimental dose distributions for 200 and 400 MeV/u ¹²C beams in water were presented by Haettner et al. These depth-dose profiles involve larger experimental uncertainties of the Bragg peak position than those reported by Schardt et al. (the focus in the work of Haettner et al. was on measuring the build-up of fragments and the experimental setup was not optimized for a high-precision measurement of the peak position; from personal communication with D. Schardt, 2009). As a consequence, to account for the more precise results of Schardt et al. in the current validation study, the dose profiles of Haettner et al. were arbitrarily shifted such that the peak position coincided with the findings of Schardt et al.; differences amounted to approximately 0.7 mm.

In contrast to the above mentioned experiments, polyethylene targets were used in the work of Weber, who measured Bragg peak profiles for ¹²C ions with energies between 90 and 330 MeV/u. The target configuration included a thick polyethylene block, complemented by a range-shifter, which allowed the regulation of the target thickness by adding thin polyethylene slabs. To obtain the absolute position of the Bragg peak, Weber calculated the polyethylene-equivalent thickness of materials in the beam path by means of ATIMA calculations. However, compared to the described experiments with water absorbers, the total equivalent thickness is smaller due to the absence of a target container (the container walls produced the largest individual contribution to the total equivalent thickness). The uncertainty of the peak position was determined as $\pm 0.01\text{--}0.04$ g/cm², depending on the experimental setup used for a given beam energy.

In the studies of Sihver et al., Haettner et al. and Weber, the experimental uncertainty of the relative ionisation was <5% at depths between entrance and peak, and >5% at depths beyond the dose maximum (these values are from personal communication with D. Schardt, 2009).

6.3.2 Monte Carlo simulation

A dedicated Geant4 application was developed which allowed the computation of depth-dose distributions for the physics model validation. The target was implemented as a homogeneous cylinder filled with either water or polyethylene; the radius was set to 10 cm and the length to 40 cm. The density of water was assumed to be 0.997 g/cm³; this value reflects the temperature during the measurements (24°C; value from personal communication with D. Schardt, 2009). The polyethylene target was modelled to have a density of 0.95 g/cm³, which corresponds to the value determined by

Weber. ^{12}C ions were assumed to hit the target in pencil-beam configuration, where the beam axis was identical to the symmetry axis of the cylinder. The ions were modelled to be completely stripped, as is the case for light ions entering the GSI synchrotron. The primary beam energy and the energy spread could be adjusted through input parameters passed to the program.

Depth-dose curves were scored by recording the energy deposition in a sequence of slices along the beam axis. The slice thickness was set to $25\ \mu\text{m}$ for beams with energies $\leq 100\ \text{MeV/u}$, to $50\ \mu\text{m}$ for energies between 100 and $200\ \text{MeV/u}$ and to $100\ \mu\text{m}$ for higher energies. This resolution is sufficient for a validation aiming at a sub-millimeter precision typically demanded in radiotherapeutical applications. Similarly as for the electron benchmarks in Chapter 4, the scoring setup was implemented as a virtual geometry, which does not force simulation steps to be interrupted at slice boundaries. The energy deposition associated with a step was randomly assigned to a point along the step.

The simulation accounted for all relevant electromagnetic and nuclear interactions of ions with matter, as well as for relevant interactions of secondaries produced in particle cascades (electrons, positrons, protons, neutrons, gammas, pions, and muons).

Electromagnetic interactions of photons and charged particles were simulated by means of physics models included in the “Standard Electromagnetic Package”; an exception was the use of the new parameterization model as described below. For gammas, processes considered in the simulation included Rayleigh scattering, Compton scattering, electron-positron pair production and the photo electric effect. Multiple scattering of charged particles was described using the Urbán model. The setup further accounted for ionization processes of charged particles, bremsstrahlung processes of electrons and positrons, as well as annihilation of positrons with electrons. For ions with atomic numbers $Z_{ion} \geq 3$, ICRU 73 tables were utilized by means of the plug-in model introduced in Section 6.2.2. In the case of water, both revised and original ICRU 73 stopping powers were considered in separate configurations (the original ICRU 73 tables for water, which are not part of the Geant4 package, were prepared in a data format readable by the simulation model). Stopping powers for ions with atomic numbers $Z_{ion} < 3$ were computed with Geant4 “Standard” models described in Section 6.2.1. Alternatively, and for comparison, simulations were repeated using “Standard” stopping power models for all ions.

In addition to electromagnetic processes, the simulation setup accounted for elastic and inelastic nuclear interactions induced by hadrons and ions in flight (see also Section 3.2.2) and also included radioactive decay and absorption at rest. An overview of cross sections and final-state models

Type	Particle	Cross sections	Final-state model
Elastic	protons, neutrons	Chiral Invariant Phase Space (CHIPS) algorithm (G4HadrElastic)	Chiral Invariant Phase Space (CHIPS) algorithm (G4HadrElastic)
	^2H , ^3H , ^3He , ^4He , π^+ , π^- Ions heavier than ^4He	Parameterization based on GHEISHA [169] code (G4HadrElastic) none	Model based on GHEISHA [169] code (G4HadrElastic) none
Inelastic	protons	Semi-empirical formula from Wellisch and Axen [170] for target nuclei with $Z > 3$ (G4ProtonInelasticCrossSection), otherwise parameterization based on GHEISHA [169] (G4HadrCrossSections)	Binary cascade model [178] (G4BinaryCascade), de-excitation as described in text
	neutrons	Formula from Wellisch and Laidlaw (unpublished) for target nuclei with $Z > 1$ and neutron energies above ~ 20 MeV (G4NeutronInelasticCrossSection), otherwise parameterization based on GHEISHA [169] (G4HadrCrossSections)	Binary cascade model [178] (G4BinaryCascade), de-excitation as described in text
	^2H , ^3H , ^3He , ^4He	Parameterization according to Tripathi et al. [171] (G4TripathiLightCrossSection)	Two options: (A) Native Geant4 QMD model [182] (G4QMDReaction) at kinetic energies > 50 MeV/u and ion binary cascade model [178] (G4BinaryLightIonReaction) at kinetic energies ≤ 50 MeV/u (B) Ion binary cascade model [178] (G4BinaryLightIonReaction)
	Ions heavier than ^4He	Parameterization according to Tripathi et al. [171] (G4TripathiLightCrossSection) for target nuclei with $Z < 3$ and parameterization according to Tripathi et al. [174] (G4TripathiCrossSection) for other target nuclei	De-excitation as described in text Same two options as for ^2H , ^3H , ^3He , ^4He
	π^+ , π^-	Parameterization (G4PionNuclearCrossSection)	Bertini intra-nuclear cascade model (G4CascadeInterface)
Capture	neutrons	Parameterization based on GHEISHA [169] code (G4HadrCrossSections)	Model based on GHEISHA [169] (G4ICapture)

Table 6.2: Hadronic processes: cross sections and final-state models employed in the simulations. Names of Geant4 C++ classes implementing model or cross section algorithms are listed in brackets.

employed for different interactions and particle species can be found in Table 6.2. For convenience, the table also lists Geant4 C++ class names containing the implementation of algorithms.

The considered elastic interaction model describes coherent elastic scattering of hadrons on target nuclei. Elastic scattering was activated for ${}^2\text{H}$, ${}^3\text{H}$, ${}^4\text{He}$, protons, neutrons, and pions. The utilized model combines different approaches: scattering of protons and neutrons is simulated by means of the Chiral Invariant Phase Space (CHIPS) algorithm. For other particles, a parameterization approach is applied which is based on the GHEISHA code.

The physics setup employs cross sections from Wellisch and Axen for inelastic proton interactions on target nuclei with $Z > 3$, and cross sections from Wellisch and Laidlaw to sample inelastic interactions of neutrons with energies above 20 MeV, except n-H interactions. Otherwise, parameterizations based on GHEISHA were used. Inelastic nucleus-nucleus interactions were sampled by means of different parameterized cross sections from Tripathi et al. The employed parameterization formula for light systems is applicable if the collision involves light nuclei (${}^1\text{H}$, ${}^2\text{H}$, ${}^3\text{He}$, or ${}^4\text{He}$) either as projectile or as elemental target constituent.

Inelastic reactions of protons and neutrons were simulated by means of the Geant4 binary cascade model, which uses the theory-driven Precompound model based on the approach of Gudima et al. [262] for the pre-equilibrium stage. Neutron capture was described by a GHEISHA-based parameterization model. The Bertini intra-nuclear cascade model was used to handle inelastic hadronic interactions of pions. As outlined in Section 3.2.2, inelastic nucleus-nucleus reaction models available in Geant4 include the ion binary cascade model and a more recent model based on a QMD generator. The latter model derives from the JQMD code [263, 264] and was re-engineered in the Geant4 hadronics package by Koi [182]. A first native Geant4 implementation of the QMD reaction model was included in version 9.1, whereas in previous versions the external JQMD code could be used in Geant4 through dedicated interfaces [265]. In the current study, the QMD-based model (configuration “A” in Table 6.2) was employed in the physics setup, whereas the binary reaction model (configuration “B” in Table 6.2) was used for comparison only in selected cases. Despite the fact that configuration “A” activates the binary model and its sub-models at lower energies, simulations based on this configuration are simply referred to as “QMD-based simulations”.

The de-excitation of excited residual nuclei, which are created in the pre-equilibrium stage of the reaction, were handled by different approaches: nuclei with atomic numbers ≤ 8 and mass numbers ≤ 16 were managed by the Fermi break-up model, whereas other excited nuclei were handled by the generalized evaporation model at excitation energies ≤ 3 MeV/nucleon

and by the statistical multifragmentation model at excitation energies larger than 3 MeV/nucleon. In the Geant4 software design, de-excitation models are invoked by a handler, which is instantiated by nuclear reaction models. In the applied toolkit version, the statistical multifragmentation and Fermi break-up models are not used by default by the de-excitation handler. However, the physics configuration was adapted to employ these de-excitation models.

6.3.3 Secondary electron production and stepping limitation

If not specified differently, the production threshold for δ -electrons was set to $T_{cut} \sim 350$ keV, which corresponds to an electron CSDA range of approximately 1 mm. With this threshold, the step size of a majority of ion steps in the simulation is determined by the mean free path associated with the generation of δ -rays. On the other hand, production thresholds of a few hundred keV or higher can impose significant restrictions on the achievable geometrical resolution if no artificial step limitation is applied. In particular, large thresholds may induce steps exceeding the size of scoring bins, which in turn cause artefacts in the computed depth-dose distributions. To avoid such dose distortions, step lengths were limited to half the size of scoring bins in the longitudinal direction.

6.3.4 Normalization of dose profiles

In the comparison with experimental data, ion depth-dose profiles obtained in the simulation commonly require a normalization since no absolute experimental reference is known. In this study, the quantity of interest is the relative ionisation of two ionisation chambers, which does not relate absolute numbers of primary particles to the deposited dose. A review of pertinent literature shows that no unique procedure exists for rescaling simulation results in the context of Bragg peak validations. Most frequently, a normalization to a certain point of the experimental curve is performed, for example to the entrance or peak dose (as in the publications of Kameoka et al. [231] and Gudowska et al. [104]), or dose profiles are normalized to the integral under curves (as for example executed by Sommerer et al. [228]).

None of these normalization methods accounts for the fact that each point of measurement (at a certain depth) is subject to an experimental uncertainty. However, the integral-based procedure is generally more stable with respect to fluctuations in the measurement. This was shown in the study of Lechner and Pia [266], where different normalization procedures and their impact on the statistical compatibility of Bragg peak profiles are discussed.

Here, dose distributions in water are normalized according to the integral under the curves, considering experimental points between entrance and dose maximum. In the case of polyethylene, the integral normalization is however not practicable, since experimental data points are available only for a small depth-range in the proximity of the Bragg peak. Instead, dose profiles are normalized to the experimental dose value determined by Weber in reference measurements without targets.

6.4 Results and discussion

For each depth-dose distribution, a large number of primaries was tracked ($4\text{--}6 \times 10^7$), such that statistical uncertainties of simulation results are small compared to experimental errors at any depth inside the target. For the sake of clarity, simulation errors are not displayed in plots.

6.4.1 Carbon ion Bragg peak in water

It is well known that the Bragg peak position is primarily determined by electronic stopping powers of primary ions, as well as by straggling effects. As illustrated in Fig. 6.1, which presents Geant4 depth-dose profiles for 400 MeV/u ^{12}C ions in water, alterations of the peak position due to the presence of hadronic interactions are negligible in view of the considered spatial resolution. This effect was studied by performing complementary simulations, where hadronic processes (see Table 6.2) were either activated or disabled. Fig. 6.1 also demonstrates the impact of straggling and scattering on the peak profile. This can be evaluated by deactivating the fluctuation and multiple scattering models and by increasing the production cut to suppress the generation of δ -electrons: the resulting profile is determined by the mean energy loss due to electronic and nuclear stopping, where the latter is less significant for the considered use case (it shifts the peak by approximately one bin of the scoring setup). The ratio of CSDA range and Bragg peak position is found to be approximately 1.0026.

Fig. 6.1 also shows alterations of the peak if the incident ion spectrum is not mono-energetic, but of Gaussian shape. Assuming for example a relative energy spread of 0.15%, the peak maximum changes its position by approximately 0.2 mm.

Fig. 6.2 compares simulated ^{12}C depth-dose distributions in water against experimental data from Sihver et al. [232] and Haettner et al. [233], where profiles from Haettner et al. were shifted along the beam axis to match more precise measurements of the peak position by Schardt et al. [257], as de-

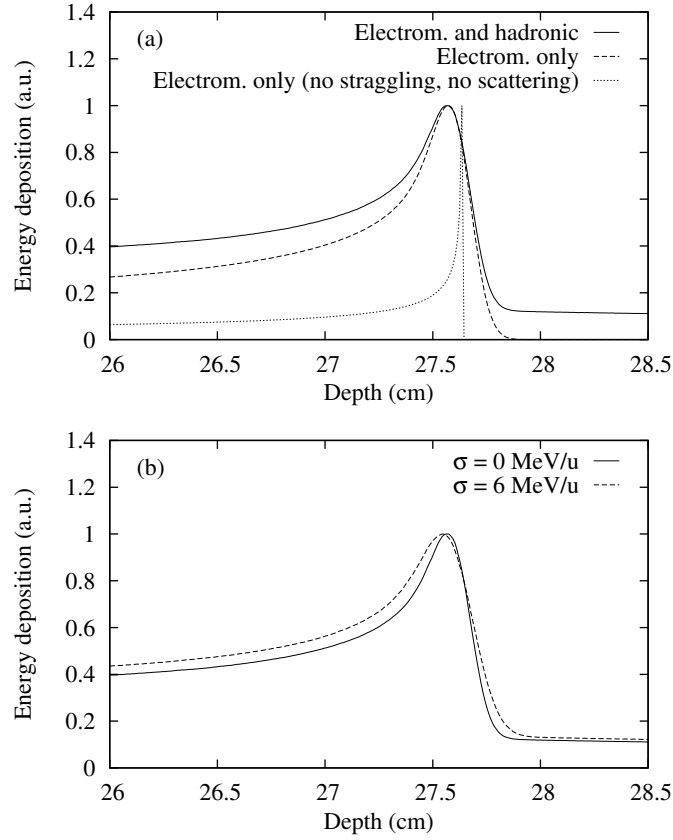


Figure 6.1: Dependency of the Bragg peak profile of 400 MeV/u ^{12}C ions in water (0.997 g/cm^3) on (a) different Geant4 physics modelling options and (b) the initial energy spread σ . Depth-dose profiles shown in (a) were obtained by using a full physics setup and, alternatively, by partially deactivating physics algorithms; σ was set to 0 MeV/u in all cases. Distributions in (b) derive from simulations with a full physics setup, using $\sigma=0$ and $\sigma=6$ MeV/u (i.e. 0.15% of primary energy), respectively. For convenience, all curves are normalized to the same peak height.

scribed in Section 6.3.1. Initial beam energies range from 195 to 400 MeV/u. The Geant4-based distributions were obtained by adopting revised ICRU 73 stopping powers in the simulation. To account for the fact that these stopping powers are inherently associated with a certain mean ionization potential (78.0 eV), the I -value of water molecules was equally set in the simulation, in order that all physics calculations (for example stopping powers of ions with $Z_{ion} \leq 2$) be based on consistent parameters. This I -value also coincides with the default mean excitation energy of water in the current Geant4 material database [27]; contrary to I -values of materials considered in previous chap-

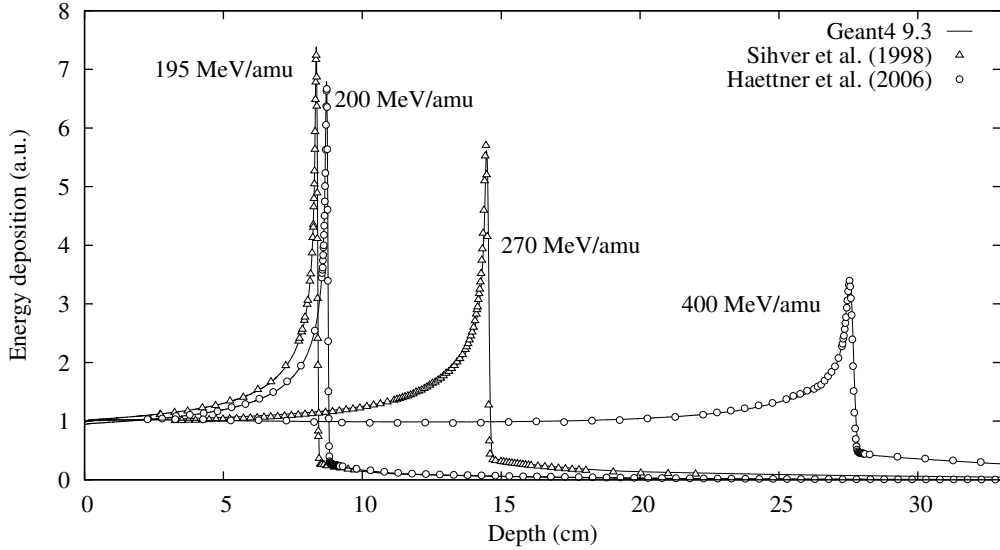


Figure 6.2: Comparison of simulated and measured ^{12}C depth-dose profiles in water (0.997 g/cm^3). Simulations were performed with Geant4 9.3, using revised ICRU 73 stopping power tables and the QMD nuclear reaction model. Experimental data derive from Sihver et al. [232] (triangles) and Haettner et al. [233] (circles), where profiles of Haettner et al. were shifted to match more precise measurements of the peak position by Schardt et al. [257]. All experimental data by courtesy of D. Schardt.

ters, the default settings for water differ from the most recent NIST [197] recommendation. The QMD model was used to simulate inelastic nuclear reactions of ions. The measured dose profiles considered in this study can typically be associated with a Gaussian energy spectrum, with a standard deviation of 0.15% (as adopted in Fig. 6.1). This was reflected in the simulation setup by adjusting input parameters accordingly. The dose distributions were normalized following the procedure outlined in Section 6.3.4.

As seen in Fig. 6.2, the Geant4-based simulations describe the shape of the experimental depth-dose curves with good accuracy. A more detailed analysis of the reproducibility of the experimental Bragg peak position is presented in Fig. 6.3, which displays the difference Δz between simulated (z_{peak}^{Sim}) and measured (z_{peak}^{Exp}) peak positions. Experimental uncertainties are indicated as error bars. In addition to the simulations with revised ICRU 73 tables, Fig. 6.3 includes results from Geant4 runs using other stopping power configurations outlined in Section 6.3.2: original ICRU 73 tables, as well as Geant4 “Standard” algorithms. For simulation runs involving the original ICRU 73 tables, the I -value in the setup was assumed to be 67.2 eV (which

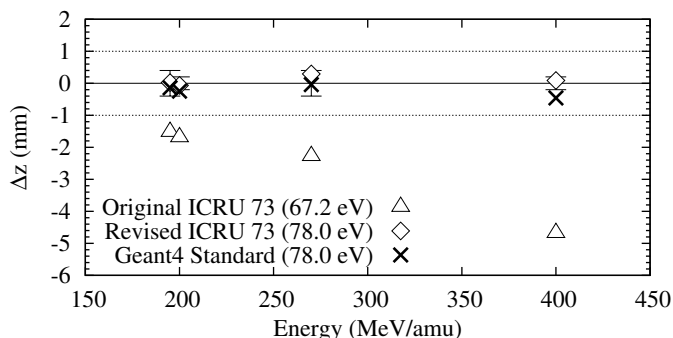


Figure 6.3: Difference Δz between simulated and measured Bragg peak positions of 195–400 MeV/u ^{12}C ions in water (0.997 g/cm^3). Simulation results were derived with Geant4 9.3, using either original or revised ICRU 73 tables or Geant4 “Standard” stopping powers (the figure legend also shows the corresponding I -values). Experimental data are from Sihver et al. [232] and Schardt et al. [257]. The dashed lines indicate deviations of ± 1 mm from the experiment and are for guidance only. Measurement uncertainties are displayed as error bars. Experimental data by courtesy of D. Schardt.

is, as previously mentioned, the value implied by the oscillator-strength spectrum used in the ICRU 73 report). Geant4 “Standard” stopping powers are evaluated for $I=78$ eV.

As can be observed in Fig. 6.3, peak positions obtained in simulations with revised ICRU 73 tables lie within the uncertainty of the measured values for all given energies. Geant4 “Standard” stopping power algorithms yield similar results, where the difference from ICRU 73-based simulations amounts to approximately 0.5 mm at 400 MeV/u. As expected, the original ICRU 73 tables lead to peak positions which significantly underestimate the measured depths. The latter finding is consistent with results presented by Paul [253], who compared CSDA ranges (of 195 and 270 MeV/u ^{12}C ions) with ranges extracted from the same data of Sihver et al. As seen in Fig. 6.3, the trend continues at higher energies and the absolute difference to the measurement is about 4.7 mm at 400 MeV/u. The original ICRU 73 stopping power tables were included in the current study despite the known deficiencies, since to the best of the author’s knowledge no quantitative comparison against revised ICRU 73 tables is yet available in the literature.

It should be noted that the mean excitation energy of 78 eV used in Fig. 6.3 is related to the experimental data from Schardt et al. (200 and 400 MeV/u beams in Fig. 6.3). Based on ion ranges extracted from measured Bragg peak profiles (also including dose distributions for other light

ion species and beam energies than those considered here), Schardt et al. determined this I -value by comparing against CSDA ranges calculated with ATIMA [261]. As outlined in Section 6.2.4, the findings of Schardt et al. were also the basis for modifying the excitation energy of the valence shell, which entered the PASS code to produce the revised ICRU 73 tables.

The satisfactory agreement of Geant4 simulations with experimental values in Fig. 6.3 confirms the accuracy of energy loss algorithms invoked at each particle step in the simulation, and also demonstrates the precision of the utilized cubic spline interpolation algorithm [166]: if one adopts a linear interpolation formula, as used in previous Geant4 versions (9.1 and older), the ICRU 73-based Bragg peak position of a 400 MeV/u ^{12}C beam would shift by ~ 2 mm.

Complementing investigations on the accuracy of simulated peak positions, Figs. 6.4 and 6.5 depict the Bragg peak of considered dose distributions in more detail. In addition to profiles from Fig. 6.2, results obtained with the Geant4 ion binary cascade model are presented. Simulation runs based upon the binary cascade model were observed to be approximately 13% (at 200 MeV/u) to 28% (at 400 MeV/u) faster than those utilizing the QMD model.

The profiles in the Figs. 6.4 and 6.5 suggest that both nuclear reaction models lead to a good description of the Bragg peak profiles. However, at larger energies QMD-based calculations reproduce the peak height more accurately. As a measure of the peak proportions, Table 6.3 compares the full width at half maximum (FWHM) derived in simulation and measurement (the experimental FWHM values were extracted from the considered data sets by means of an interpolation algorithm). As demonstrated, QMD-based simulations lead to a good agreement with experimental widths at all beam energies. The satisfactory results can partly be attributed to the modelling of energy loss fluctuations (cf. Fig. 6.1) and to low-energy stopping powers (the fluctuation model for ions has been subject of evolution in recent Geant4 versions); the consistent agreement over the entire energy range also suggests that experimental conditions can be successfully reproduced with the employed simplified geometry and beam model.

Compared to QMD-based results, simulations with the binary cascade model predict similar proportional features at energies ≤ 270 MeV/u, whereas discrepancies become apparent at 400 MeV/u. The significantly larger FWHM value produced by the binary cascade model can be explained by isotope yields resulting from primary particle fragmentation: as reported by Kameoka [231] the binary model tends to overproduce ^{11}C ions. At higher energies this manifests itself as a small bump in the depth-dose profile (see Fig. 6.5(b)), occurring at a depth where the dose contribution of ^{11}C ions exhibits a maxi-

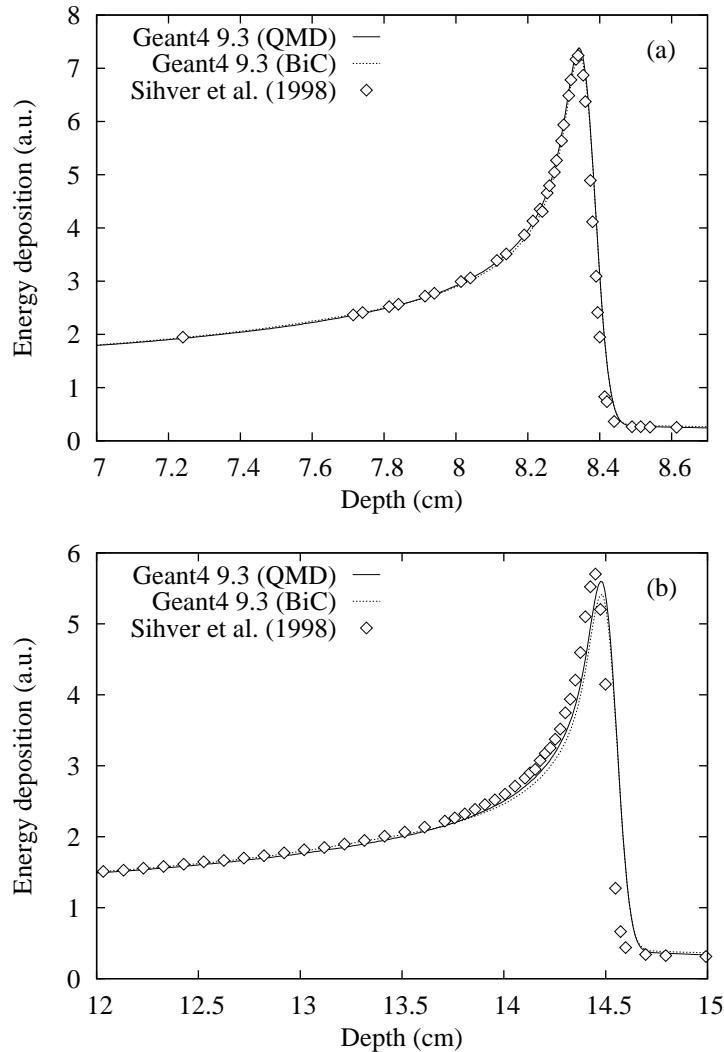


Figure 6.4: Close-up view of simulated and measured ^{12}C Bragg peak profiles in water. Incident beam energies are (a) 195 and (b) 270 MeV/u. Simulations were based on revised ICRU 73 stopping powers. Results were obtained using either the QMD or the ion binary cascade (BiC) nuclear reaction model. Experimental data derive from Sihver et al. [232]. All experimental data by courtesy of D. Schardt.

mum (upstream the Bragg peak). This affects the peak-to-plateau ratio and as a consequence also induces the numerical difference between experimental data and simulation in Table 6.3.

A comparison between the two nuclear models is included here, since previous publications addressing the evaluation of Geant4-based dose-profiles against experimental data most commonly adopted the binary cascade model

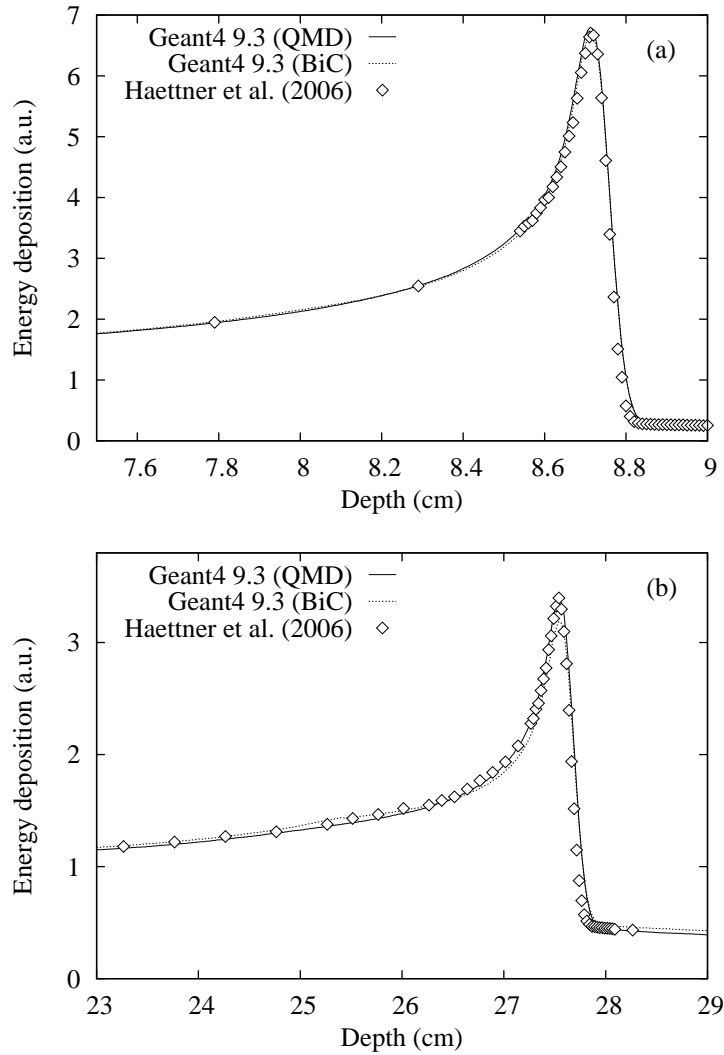


Figure 6.5: Close-up view of simulated and measured ^{12}C Bragg peak profiles in water. Incident beam energies are (a) 200 and (b) 400 MeV/u. Simulations were based on revised ICRU 73 stopping powers. Results were obtained using either the QMD or the ion binary cascade (BiC) nuclear reaction model. Experimental data originate from Haettner et al. [233]. The experimental peak position was adjusted to match more precise measurements of Schardt et al. [257]. All experimental data by courtesy of D. Schardt.

to describe inelastic nuclear reactions of ions [134, 229, 230] (as previously mentioned, in Refs. [229, 230] older versions of Geant4 were compared against the same experimental data as used in the current work). A first comparative evaluation of the binary model against the external JQMD code was carried

	195 MeV/u	200 MeV/u	270 MeV/u	400 MeV/u
Experiment	2.3	2.3	4.1	10.3
Geant4 (QMD)	2.3	2.4	4.3	10.3
Geant4 (BiC)	2.3	2.4	4.4	12.5

Table 6.3: Full width at half maximum (in mm) corresponding to ^{12}C Bragg peaks in water (0.997 g/cm^3). Simulation results were produced with an initial energy spread of 0.15%, using either the ion binary cascade (BiC) or the QMD model. Experimental values were derived by means of a cubic spline interpolation of measured data in Fig. 6.2.

out by Kameoka et al. [231]. However, to the author’s knowledge, no Geant4-based validation paper of ion Bragg peaks has yet included the native Geant4 implementation of the QMD nuclear reaction model. For the dynamical phase of nuclear reactions the Geant4 QMD model is a re-engineered version of the JQMD code, whereas a different handling of the break-up is employed: JQMD uses a statistical decay algorithm, which features sequential light particle evaporation. In contrast, the Geant4 QMD model passes excited fragments to internal Geant4 de-excitation algorithms, which also allow for multi-particle exit channels. In the present case, most of the excited remnants are handled by the Fermi break-up model. A recent analysis of the Geant4 Fermi break-up can be found in Ref. [267].

The current study shows, that the native QMD implementation of the current Geant4 version can be considered a suitable alternative to the binary cascade model for simulating total dose distributions of carbon ion beams in water. This confirms satisfying results reported by Kameoka et al. when using the external JQMD code. A validation of charge-changing cross sections in Geant4 simulations based upon the binary cascade model and the JQMD code, respectively, may be found in a previous publication of Toshito [268]. Quantitative statements concerning fragment production are out of the scope of the present study. However, it can be concluded that below 270 MeV/u predictions of binary cascade and QMD models are indistinguishable within the experimental accuracy of depth dose profiles.

6.4.2 Carbon ion Bragg peak in polyethylene

A similar validation as in the previous section was performed for 90–330 MeV/u ^{12}C ions incident on polyethylene. Fig. 6.6 compares simulated depth-dose profiles against experimental data from Weber [260]. The Geant4-based distributions were obtained by using ICRU 73 stopping powers, where the I -value as implied by the corresponding oscillator-strength spectrum (52.86 eV)

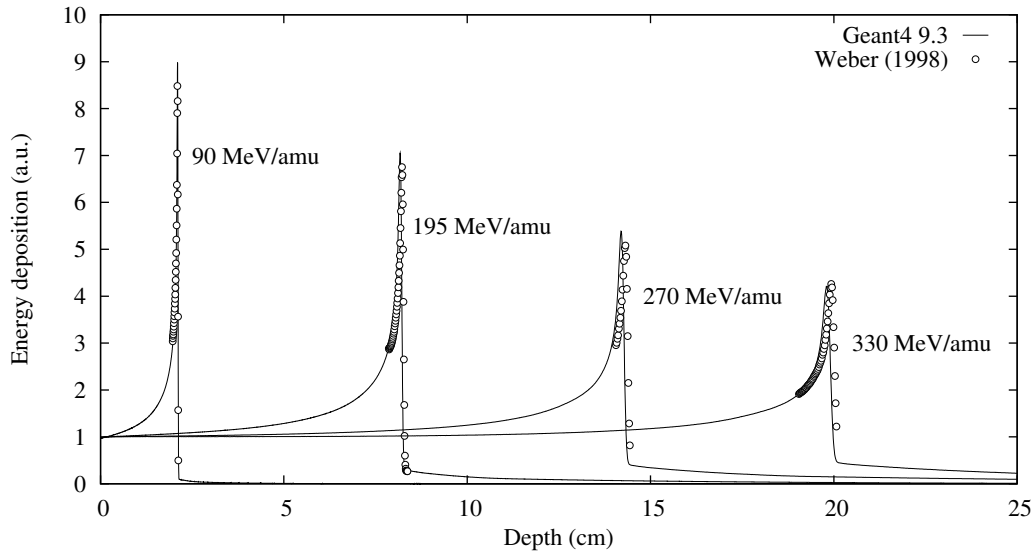


Figure 6.6: Comparison of simulated and measured ^{12}C depth-dose profiles in polyethylene (0.95 g/cm^3). Simulations were performed with Geant4 9.3, using ICRU 73 stopping power tables and the QMD nuclear reaction model. Experimental data derive from Weber [260]. All experimental data by courtesy of D. Scharadt and U. Weber.

was used in the simulation setup (this I -value is from personal communication with P. Sigmund; in contrast to what is stated in the ICRU 73 report, stopping powers for polyethylene were not derived by applying Bragg’s additivity rule, but by using oscillator strengths for outer shells of polyethylene from the book of Berkowitz [269]). Inelastic nuclear reactions of ions were simulated by means of the QMD model. As in the case of water, the initial energy spread of the beam was set to 0.15%. The dose profiles were normalized according to the procedure outlined in Section 6.3.4.

A more detailed analysis of differences between simulated and measured Bragg peak positions is given in Fig. 6.7. Experimental uncertainties are displayed as error bars. As in the previous section, simulation results were also obtained by using Geant4 “Standard” stopping powers, where the same I -value of polyethylene as used in ICRU 73 was applied in the setup.

As can be observed in Fig. 6.7, for a beam energy of 90 MeV/u the ICRU 73-based simulation reproduces the measured value within the experimental uncertainty, but for higher energies the Bragg peak position is predicted at slightly smaller depths inside the absorber. At the largest considered beam energy, the shift Δz is approximately 1.3 mm. Geant4 “Standard” stopping power models yield larger discrepancies with respect to the experiment, ex-

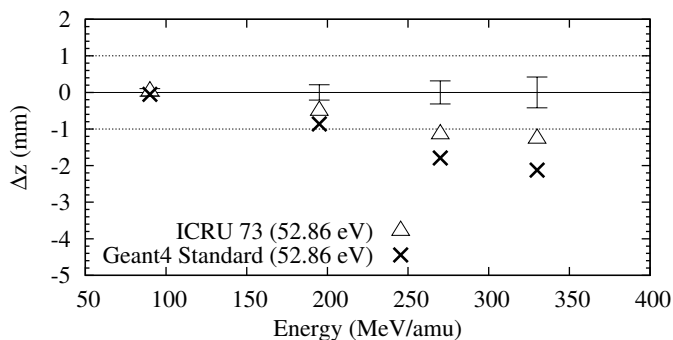


Figure 6.7: Difference Δz between computed and measured Bragg peak positions of 90–330 MeV/u ^{12}C ions in polyethylene (0.95 g/cm^3). Simulation results were derived with Geant4 9.3, using either ICRU 73 or Geant4 “Standard” stopping powers (the figure legend also shows the corresponding I -values). Experimental data are from Weber [260]. The dashed lines indicate deviations of ± 1 mm from the experiment and are for guidance only. Measurement uncertainties are displayed as error bars. Experimental data by courtesy of D. Schardt and U. Weber.

cept at 90 MeV/u where results are comparable with both measurement and ICRU 73-based simulation. At 330 MeV/u, the difference between Geant4 “Standard” results and experimental values amounts to 2.1 mm.

Figs. 6.8 and 6.9 depict the Bragg peak profiles of the 90–330 MeV/u beams in more detail. Dotted curves indicate uncertainties in the normalization factor due to the experimental error associated with the dose at the reference depth. In contrast to the previous section, the comparison generally allows for less conclusive statements, for example concerning the overall agreement or fragmentation tails, since experimental data sets are concentrated around the Bragg peak position.

Given the uncertainty of normalization factors as well as the measurement error associated with the peak dose, proportional features like the peak height are well reproduced in the simulation (Figs. 6.8 and 6.9 illustrate that uncertainties in the normalization against a single dose point can be a significant factor when analysing simulation results; it should be mentioned that most previous studies on Monte Carlo code validation do not take this into account). Owing to the underestimation of ion penetration depths at higher energies, simulated curves do not match the experimental dose pattern in the vicinity of the peak to the same level of accuracy as for water. However, the observed discrepancy between positions of measured and simulated dose maxima is less than the full width at half maximum of the peak.

A comparison of FWHM values measured by Weber against simulation re-

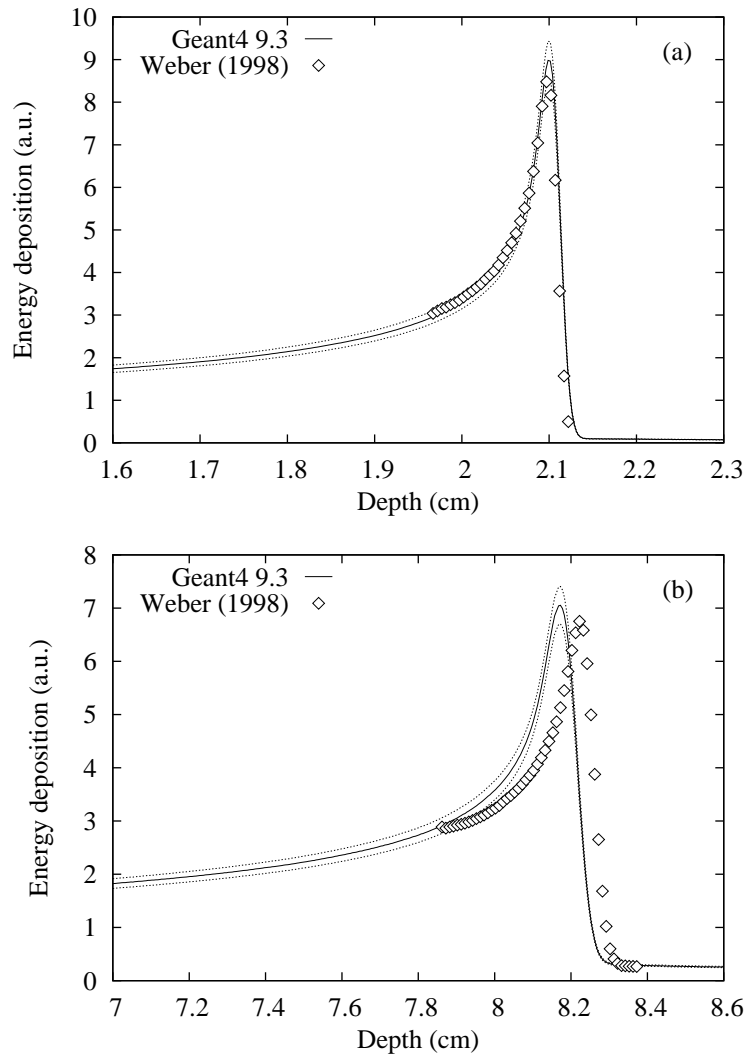


Figure 6.8: Close-up view of simulated and measured ^{12}C Bragg peak profiles in polyethylene. Initial beam energies are (a) 90 and (b) 195 MeV/u. Simulation results were obtained by using the ICRU 73-based stopping power configuration and the QMD nuclear reaction model. Uncertainties in the applied normalization due to experimental errors are also indicated (dotted lines). Experimental data derive from Weber [260]. Data by courtesy of D. Schardt and U. Weber.

sults, obtained either with the QMD or the binary cascade model, is given in Table 6.4. As expected from findings in the previous section, at higher energies the binary model leads to a larger FWHM value compared to QMD-based simulations. However, in contrast to the results obtained for water none of the models yields a consistently better agreement with the experimental values

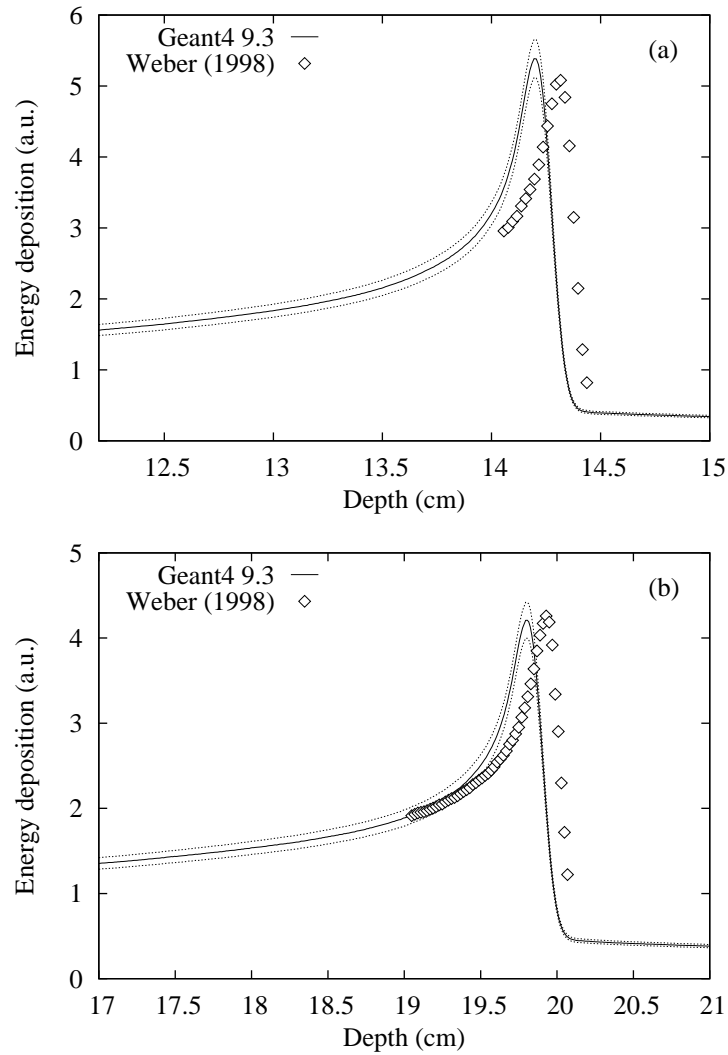


Figure 6.9: As in Fig. 6.8, for beam energies of (a) 270 and (b) 330 MeV/u.

when the beam energy increases. The discrepancies between measurement and either of the simulated values, observed for 270 and 330 MeV/u ions, can partly be attributed to systematic effects due to the simplified geometry model adopted in the simulation setup. For example, inhomogeneities in materials traversed by the beam can impact the width; such effects were not taken into account in the Monte Carlo configuration.

	90 MeV/u	195 MeV/u	270 MeV/u	330 MeV/u
Experiment	0.7	2.3	5.0	7.0
Geant4 (QMD)	0.6	2.3	4.3	6.7
Geant4 (BiC)	0.6	2.3	4.5	7.4

Table 6.4: Full width at half maximum (in mm) corresponding to ^{12}C Bragg peaks in polyethylene (0.95 g/cm^3). Simulation results were produced with an initial energy spread of 0.15%, using either the ion binary cascade (BiC) or the QMD model. Experimental values were taken from Weber [260]. Experimental errors were specified as 0.05 mm at 90 and 195 MeV/u, and as 0.1 mm at 270 and 330 MeV/u.

6.5 Conclusions

This chapter systematically investigated the accuracy of Geant4 electronic energy loss algorithms for simulating depth-dose profiles of ^{12}C beams incident on tissue-like materials. It was shown that simulations using revised ICRU 73 stopping powers of water, recently incorporated into Geant4 and based on a mean excitation energy of 78.0 eV, accurately reproduce the experimental Bragg peak position for beam energies of therapeutical interest. The difference $|\Delta z|/z_{peak}^{Exp}$ between calculation and measurement was $<0.2\%$ in all cases (as already noted, for two of the considered beam energies the underlying experimental data from Schardt et al. [257] impacted the I -value used by Sigmund et al. [37] to produce the revised ICRU 73 tables). Geant4 “Standard” stopping powers, employing an effective ion charge, lead to comparable results. In the case of polyethylene targets, satisfactory results could be achieved when using ICRU 73 tables (the corresponding I -value is 52.86 eV), however at higher energies depths of measured dose maxima were slightly underestimated; $|\Delta z|/z_{peak}^{Exp}$ was found to be less than 0.9%.

This study shows that current Geant4 simulation models are capable to predict absolute Bragg peak positions with good accuracy. The observed discrepancies between simulated and experimental peak positions are typically smaller than other uncertainties affecting ion range calculations in realistic clinical scenarios. For example errors associated with the correlation between Hounsfield units from computed tomography (CT) images and water-equivalent path lengths can induce larger range uncertainties (see for example the work of Rietzel et al. [270]).

The depth-dose profiles of this study also demonstrate that proportional features of dose distributions can be well described. This can in part be attributed to low-energy stopping powers. We also conclude that the current Geant4 implementation of the QMD model shows accurate results concerning

the description of physical dose distributions in radiotherapeutical applications. For energies below 270 MeV/u the binary cascade model yields similar results. More detailed modelling features, like production yields of fragments, would require further validation beyond the scope of this study.

Chapter 7

Summary and conclusions

By sampling individual particle trajectories, Monte Carlo radiation transport simulations inherently allow to mimic realistic scattering conditions encountered in different scenarios. Secondly, through the generation of secondary particle cascades one explicitly accounts for radiation fields effectively contributing to energy deposition and fluence distributions in matter. Owing to a comprehensive set of physics options and due to its flexible software design, the Geant4 toolkit, developed by an international collaboration, has gained significant popularity in the scientific community. In particular, it is increasingly employed in medical physics applications. This thesis presented a comprehensive and detailed examination of Geant4 physics algorithms pertinent to radiotherapy simulations. In addition, physics options were extended by incorporating recent ion stopping powers into the toolkit. The accuracy of Monte Carlo models was investigated by means of benchmark studies focusing on aspects of electron and ion transport.

Chapter 4 presented a comparative study of energy deposition profiles induced by 0.05–1 MeV electrons in solid targets. Simulation predictions obtained with different models and Geant4 versions were compared against experimental data reported in the literature. In contrast to previous publications, a large range of material samples and beam energies was covered in a systematic way. The goal of the study was to identify the accuracy achievable as a function of the atomic number Z , considering that realistic simulation scenarios typically involve materials of varying composition. The comparisons demonstrated an improvement of Geant4 predictions for lower- Z materials across different release versions (8.1.p02 and 9.1/9.1p03). The changes were attributed to modifications in the semi-empirical multiple scattering model by Urbán. No significant differences could be determined for medium- and high- Z samples. Besides that, obtained simulation results exhibited a significant dependency on transport parameters governing the step

size. This deficiency has already been reported in previous studies based on earlier Geant4 versions. For the specific set of parameter values considered in the current work, energy loss models based on LLNL evaluated data libraries were found to be closer to experimental data than models implementing analytical algorithms originally developed for the PENELOPE Monte Carlo code.

Complementing the dose benchmarks in Chapter 4, Chapter 5 was dedicated to the simulation of electron backscattering. A quantitative description of electron backscattering due to heterogeneities in materials is fundamental to many applications in radiotherapy. Electron transport algorithms were benchmarked against published experimental energy and charge albedos, covering kinetic energies between 0.1 and 14 MeV. Two alternative multiple scattering models were examined, one being based on the Goudsmit-Saunderson theory and the second being the model by Urbán also evaluated in Chapter 4. The study showed that simulations based on the first multiple scattering model are in reasonable agreement with experimental data at all considered energies. Obtained Monte Carlo predictions accurately described the dependency of backscattering data with beam energy and angle of incidence. The model developed by Urbán yielded results with comparable accuracy at lower energies (≤ 1 MeV), but tended to overestimate the experimental backscatter yield and angular distributions at higher energies.

Contrary to the previous chapters, Chapter 6 dealt with light-ion transport. A new parameterization model, based on ICRU 73 stopping powers, was implemented and applied to study dose distributions in commonly used phantom materials. Beam energies typically encountered in radiotherapy were examined. A good agreement could be achieved between simulated distributions in water and experimental data reported in the literature. This was partly due to recently published revisions of ICRU 73 tabulations incorporated into Geant4. In polyethylene, slight deviations between calculated and experimental Bragg peak positions were observed, which were attributed to the corresponding I -value adopted in the ICRU 73 report. The results presented in Chapter 6 further demonstrated the capability of the native Geant4-QMD model for Bragg peak simulations in tissue-like media.

This thesis highlighted capabilities and limits of a variety of Monte Carlo physics models in the Geant4 toolkit. In particular, the presented results provide some guidance about the accuracy achievable in Geant4-based radiotherapy applications involving the transport of electrons and ions.

Appendix

A.1 Geant4 material data

Table 7.1 presents material densities and mean excitation energies employed in the Geant4 material database [27]. With few exceptions (e.g. water), material properties are based on values published by the National Institute of Standards and Technology (NIST) [197].

Material	Density (g/cm ³)	<i>I</i> -value (eV)
Be	1.848	63.7
C	1.700	78.0
Al	2.699	166.0
Ti	4.540	233.0
Cu	8.960	322.0
Mo	10.22	424.0
Ag	10.50	470.0
Ta	16.65	718.0
Au	19.32	790.0
U	18.95	890.0

Table 7.1: Densities and mean excitation energies *I* of target materials included in the simulation setup. Values originate from the Geant4 material database [27], which is based on reference data published by NIST [197].

Bibliography

- [1] E. C. Halperin, C. A. Perez, L. W. Brady (Eds.), *Perez and Brady's principles and practice of radiation oncology*, Lippincott Williams & Wilkins, Philadelphia, PA, 5th edition, 2008.
- [2] P. Boyle, B. Levin (Eds.), *World Cancer Report 2008*, Technical Report, International Agency for Research on Cancer (IARC), Lyon, France, 2008.
- [3] G. Delaney, S. Jacob, C. Featherstone, M. Barton, The role of radiotherapy in cancer treatment, *Cancer* 104 (2005) 1129–1137.
- [4] M. Goitein, *Radiation Oncology: A Physicist's Eye View*, Biological and Medical Physics, Biomedical Engineering, Springer, New York, 2008.
- [5] N. Papanikolaou, J. Battista, A. Boyer, C. Kappas, E. Klein, T. Mackie, M. Sharpe, J. V. Dyk, *AAPM Report No. 85: Tissue inhomogeneity corrections in megavoltage photon beams*, Medical Physics Publishing, Madison, WI, 2004.
- [6] B. A. Fraass, J. Smathers, J. Deye, Summary and recommendations of a National Cancer Institute workshop on issues limiting the clinical use of Monte Carlo dose calculation algorithms for megavoltage external beam radiation therapy, *Med. Phys.* 30 (2003) 3206–3216.
- [7] T. Bortfeld, IMRT: a review and preview, *Phys. Med. Biol.* 51 (2006) R363–R379.
- [8] G. Kraft, Tumor Therapy with Heavy Charged Particles, *Prog. Part. Nucl. Phys.* 45 (2000) S473–S544.
- [9] U. Amaldi, G. Kraft, Radiotherapy with beams of carbon ions, *Rep. Prog. Phys.* 68 (2005) 1861–1882.

- [10] D. Schardt, T. Elsässer, D. Schulz-Ertner, Heavy-ion tumor therapy: Physical and radiobiological benefits, *Rev. Mod. Phys.* 82 (2010) 383–425.
- [11] A. R. Smith, Vision 20/20: Proton therapy, *Med. Phys.* 36 (2009) 556–568.
- [12] P. M. Evans, Anatomical imaging for radiotherapy, *Phys. Med. Biol.* 53 (2008) R151–R191.
- [13] U. Nestle, W. Weber, M. Hentschel, A.-L. Grosu, Biological imaging in radiation therapy: role of positron emission tomography, *Phys. Med. Biol.* 54 (2009) R1–R25.
- [14] D. I. Thwaites, J. B. Tuohy, Back to the future: the history and development of the clinical linear accelerator, *Phys. Med. Biol.* 51 (2006) R343–R362.
- [15] P. J. Bryant et al., Proton-Ion Medical Machine Study (PIMMS), 2, CERN-PS-2000-007-DR, 2000.
- [16] N. Papanikolaou, S. Stathakis, Dose-calculation algorithms in the context of inhomogeneity corrections for high energy photon beams, *Med. Phys.* 36 (2009) 4765–4775.
- [17] Ahnesjö, M. M. Aspradakis, Dose calculations for external photon beams in radiotherapy, *Phys. Med. Biol.* 44 (1999) R99–R155.
- [18] N. Reynaert, S. C. van der Marck, D. R. Schaart, W. V. der Zee, C. V. Vliet-Vroegindeweyj, M. Tomsej, J. Jansen, B. Heijmen, M. Coghe, C. D. Wagter, Monte Carlo treatment planning for photon and electron beams, *Rad. Phys. Chem.* 76 (2007) 643–686.
- [19] F. Verhaegen, J. Seuntjens, Monte Carlo modelling of external radiotherapy photon beams, *Phys. Med. Biol.* 48 (2003) R107–R164.
- [20] C. M. Ma, S. B. Jiang, Monte Carlo modelling of electron beams from medical accelerators, *Phys. Med. Biol.* 44 (1999) R157–R189.
- [21] I. J. Chetty et al., Report of the AAPM Task Group No. 105: Issues associated with clinical implementation of Monte Carlo-based photon and electron external beam treatment planning, *Med. Phys.* 34 (2007) 4818–4853.

- [22] F. James, Monte Carlo theory and practice, *Rep. Prog. Phys.* 43 (1980) 1145–1189.
- [23] N. Metropolis, The beginning of the Monte Carlo method, *Los Alamos Sci. Special Issue* (15) (1987) 125–130. Available at <http://library.lanl.gov/la-pubs/00326866.pdf>, accessed Aug 2010.
- [24] D. W. O. Rogers, Fifty years of Monte Carlo simulations for medical physics, *Phys. Med. Biol.* 51 (2006) R287–R301.
- [25] S. Agostinelli et al., Geant4 – a simulation toolkit, *Nucl. Instr. and Meth. A* 506 (2003) 250–303.
- [26] J. Allison et al., Geant4 developments and applications, *IEEE Trans. Nucl. Sci.* 53 (2006) 270–278.
- [27] J. Apostolakis et al., Geometry and physics of the Geant4 toolkit for high and medium energy applications, *Rad. Phys. Chem.* 78 (2009) 859–873.
- [28] F. Wauters et al., A GEANT4 Monte-Carlo simulation code for precision β spectroscopy, *Nucl. Instr. and Meth. A* 609 (2009) 156–164.
- [29] F. Lei, P. R. Truscott, C. S. Dyer, B. Quaghebeur, D. Heynderickx, P. Nieminen, H. Evans, E. Daly, MULASSIS: A Geant4-Based Multi-layered Shielding Simulation Tool, *IEEE Trans. Nucl. Sci.* 49 (2002) 2788–2793.
- [30] G. Santin, V. Ivanchenko, H. Evans, P. Nieminen, E. Daly, GRAS: A General-Purpose 3-D Modular Simulation Tool for Space Environment Effects Analysis, *IEEE Trans. Nucl. Sci.* 52 (2005) 2294–2299.
- [31] H. Zaidi, G. Sgouros (Eds.), *Therapeutic applications of Monte Carlo calculations in nuclear medicine*, Series in Medical Physics and Biomedical Engineering, Institute of Physics Publishing, Bristol, UK, 2003.
- [32] S. Jan et al., GATE: a simulation toolkit for PET and SPECT, *Phys. Med. Biol.* 49 (2004) 4543–4561.
- [33] P. Arce, P. Rato, M. Cañadas, J. I. Lagares, GAMOS: a GEANT4-based easy and flexible framework for nuclear medicine applications, in: *IEEE Nuclear Science Symposium Conference Record*, Dresden, Germany, 2008, pp. 3162–3168.

- [34] M. J. Berger, Monte Carlo calculations of the penetration and diffusion of fast charged particles, in: B. Alder, S. Ferbach, M. Rotenberg (Eds.), *Methods in computational physics*, volume 1, Academic Press, New York, 1963, pp. 135–215.
- [35] I. Kawrakow, A. F. Bielajew, On the condensed history technique for electron transport, *Nucl. Instr. and Meth. B* 142 (1998) 253–280.
- [36] ICRU (International Commission on Radiation Units and Measurements), ICRU Report 73: Stopping of Ions Heavier Than Helium, J. ICRU 5, No. 1, Oxford University Press, Oxford, 2005.
- [37] P. Sigmund, A. Schinner, H. Paul, Errata and Addenda: ICRU Report 73 (Stopping of Ions Heavier than Helium), International Commission on Radiation Units and Measurements, 2009.
- [38] A. E. Nahum, Condensed-history Monte-Carlo simulation for charged particles: what can it do for us?, *Radiat. Environ. Biophys.* 38 (1999) 163–173.
- [39] J. F. Williamson, Brachytherapy technology and physics practice since 1950: a half-century of progress, *Phys. Med. Biol.* 51 (2006) R303–R325.
- [40] M. Ljungberg, S.-E. Strand, M. A. King (Eds.), *Monte Carlo calculations in nuclear medicine: applications in diagnostic imaging*, Series in Medical Physics and Biomedical Engineering, Institute of Physics Publishing, Bristol, UK, 1998.
- [41] H. Zaidi, Relevance of accurate Monte Carlo modeling in nuclear medical imaging, *Med. Phys.* 26 (1999) 574–608.
- [42] PubMed, <http://www.ncbi.nlm.nih.gov/entrez>, accessed Nov 2011.
- [43] I. Lux, L. Koblinger, *Monte Carlo Particle Transport Methods: Neutron and Photon Calculations*, CRC Press, Boca Raton, Florida, 1991.
- [44] W. Feller, *An introduction to probability theory and its applications*, volume 1, Wiley, New York, 3rd edition, 1967.
- [45] T. Pawlicki, C.-M. Ma, Monte Carlo simulation for MLC-based intensity-modulated radiotherapy, *Med. Dos.* 26 (2001) 157–168.

- [46] J. C. Polf, M. C. Harvey, U. Titt, W. D. Newhauser, A. R. Smith, Initial beam size study for passive scatter proton therapy. I. Monte Carlo verification, *Med. Phys.* 34 (2007) 4213–4218.
- [47] H. Paganetti, H. Jiang, K. Parodi, R. Slopsma, M. Engelsman, Clinical implementation of full Monte Carlo dose calculation in proton beam therapy, *Phys. Med. Biol.* 53 (2008) 4825–4853.
- [48] E. Spezi, G. Lewis, An overview of Monte Carlo treatment planning for radiotherapy, *Rad. Prot. Dos.* 131 (2008) 123–129.
- [49] R. Y. Rubinstein, D. P. Kroese, *Simulation and the Monte Carlo Method*, John Wiley & Sons, Inc., Hoboken, New Jersey, 2nd edition, 2008.
- [50] F. Salvat, J. M. Fernández-Varea, Overview of physical interaction models for photon and electron transport used in Monte Carlo codes, *Metrologia* 46 (2009) S112–S138.
- [51] J. M. Fernández-Varea, R. Mayol, J. Baró, F. Salvat, On the theory and simulation of multiple elastic scattering of electrons, *Nucl. Instr. and Meth. B* 73 (1993) 447–473.
- [52] P. Andreo, Monte Carlo techniques in medical radiation physics, *Phys. Med. Biol.* 36 (1991) 861–920.
- [53] D. E. Raeside, Monte Carlo principles and applications, *Phys. Med. Biol.* 21 (1976) 181–197.
- [54] A. F. Bielajew, *Fundamentals of the Monte Carlo method for neutral and charged particle transport*, The University of Michigan. Available at <http://www-personal.umich.edu/~bielajew/MCBook/book.pdf>, last accessed Nov 2011.
- [55] F. James, *Statistical methods in experimental physics*, World Scientific Publishing, 2nd edition, 2006.
- [56] J. Baró, J. Sempau, J. M. Fernández-Varea, F. Salvat, PENELOPE: An algorithm for Monte Carlo simulation of the penetration and energy loss of electrons and positrons in matter, *Nucl. Instr. and Meth. B* 100 (1995) 31–46.
- [57] P. F. Rose, ENDF-201, ENDF/B-VI Summary Documentation, BNL-NCS-17541, 1991.

- [58] F. Salvat, J. M. Fernández-Varea, E. Acosta, J. Sempau, PENELOPE – A Code System for Monte Carlo Simulation of Electron and Photon Transport, in: Workshop Proceedings Issy-les-Moulineaux, France, pp. 1–234.
- [59] W. R. Nelson, H. Hirayama, D. W. O. Rogers, The EGS4 Code System, Technical Report SLAC-265, Stanford Linear Accelerator Center, Stanford, CA, 1985.
- [60] GEANT, Detector Description and Simulation Tool, CERN Program Library Long Writeup W5013, 1994.
- [61] A. F. Bielajew, D. W. O. Rogers, PRESTA: the parameter reduced electron-step transport algorithm for electron Monte Carlo transport, Nucl. Instr. and Meth. B 18 (1987) 165–181.
- [62] H. W. Lewis, Multiple Scattering in an Infinite Medium, Phys. Rev. 78 (1950) 526–529.
- [63] G. Z. Molière, Theorie der Streuung schneller geladener Teilchen II. Mehrfach- und Vielfachstreuung, Z. Naturforsch. 3 (1948) 78–97.
- [64] S. Goudsmit, J. L. Saunderson, Multiple Scattering of Electrons, Phys. Rev. 57 (1940) 24–29.
- [65] S. Goudsmit, J. L. Saunderson, Multiple Scattering of Electrons. II, Phys. Rev. 58 (1940) 36–42.
- [66] P. Sigmund, Stopping power: wrong terminology, ICRU News 1 (2000).
- [67] Geant4 Collaboration, Geant4 Physics Reference Manual, Geant4 9.4 edition, 2010. Available at <http://geant4.web.cern.ch/geant4/UserDocumentation/UsersGuides/PhysicsReferenceManual/fo/PhysicsReferenceManual.pdf>.
- [68] Ahnesjö, B. Hårdemark, U. Isacson, A. Montelius, The IMRT information process—mastering the degrees of freedom in external beam therapy, Phys. Med. Biol. 51 (2006) R381–R402.
- [69] E. Sterpin, M. Tomsej, B. D. Smedt, N. Reynaert, S. Vynckier, Monte Carlo evaluation of the AAA treatment planning algorithm in a heterogeneous multilayer phantom and IMRT clinical treatments for an Elekta SL25 linear accelerator, Med. Phys. 34 (2007) 1665–1676.

- [70] A. Fogliata, E. Vanetti, D. Albers, C. Brink, A. Clivio, T. Knöös, G. Nicolini, L. Cozzi, On the dosimetric behaviour of photon dose calculation algorithms in the presence of simple geometric heterogeneities: comparison with Monte Carlo calculations, *Phys. Med. Biol.* 52 (2007) 1363–1385.
- [71] F. Hasenbalg, H. Neuenschwander, R. Mini, E. J. Born, Collapsed cone convolution and analytical anisotropic algorithm dose calculations compared to VMC++ Monte Carlo simulations in clinical cases, *Phys. Med. Biol.* 52 (2007) 3679–3691.
- [72] T. Knöös, E. Wieslander, L. Cozzi, C. Brink, A. Fogliata, D. Albers, H. Nyström, S. Lassen, Comparison of dose calculation algorithms for treatment planning in external photon beam therapy for clinical situations, *Phys. Med. Biol.* 51 (2006) 5785–5807.
- [73] J. Fan, J. Li, L. Chen, S. Stathakis, W. Luo, F. D. Plessis, W. Xiong, J. Yang, C.-M. Ma, A practical Monte Carlo MU verification tool for IMRT quality assurance, *Phys. Med. Biol.* 51 (2006) 2503–2515.
- [74] O. Pisaturo, R. Moeckli, R.-O. Mirimanoff, F. O. Bochud, A Monte Carlo-based procedure for independent monitor unit calculation in IMRT treatment plans, *Phys. Med. Biol.* 54 (2009) 4299–4310.
- [75] R. Nath, L. L. Anderson, G. Luxton, K. A. Weaver, J. F. Williamson, A. S. Meigooni, Dosimetry of interstitial brachytherapy sources: Recommendations of the AAPM Radiation Therapy Committee Task Group No. 43, *Med. Phys.* 22 (1995) 209–234.
- [76] M. J. Rivard, B. M. Coursey, L. A. DeWerd, W. F. Hanson, M. Saiful Huq, G. S. Ibbott, M. G. Mitch, R. Nath, J. F. Williamson, Update of AAPM Task Group No. 43 Report: A revised AAPM protocol for brachytherapy dose calculations, *Med. Phys.* 31 (2004) 633–672.
- [77] Z. Li, R. K. Das, L. A. DeWerd, G. S. Ibbott, A. S. Meigooni, J. Pérez-Calatayud, M. J. Rivard, R. S. Sloboda, J. F. Williamson, Dosimetric prerequisites for routine clinical use of photon emitting brachytherapy sources with average energy higher than 50 keV, *Med. Phys.* 34 (2007) 37–40.
- [78] S. H. Hosseini, M. Sadeghi, V. Ataeinia, Dosimetric comparison of four new design ^{103}Pd brachytherapy sources: Optimal design using silver and copper rod cores, *Med. Phys.* 36 (2009) 3080–3085.

- [79] R. Pirchio, E. Galiano, M. Saraví, D. Banchik, C. Muñoz, On the physical, spectral, and dosimetric characteristics of a new ^{125}I brachytherapy source, *Med. Phys.* 34 (2007) 2801–2806.
- [80] M. J. Rivard, Monte Carlo radiation dose simulations and dosimetric comparison of the model 6711 and 9011 ^{125}I brachytherapy sources, *Med. Phys.* 36 (2009) 486–491.
- [81] D. Granero, J. Pérez-Calatayud, F. Ballester, Technical note: Dosimetric study of a new Co-60 source used in brachytherapy, *Med. Phys.* 34 (2007) 3485–3488.
- [82] A. S. Meigooni, C. Wright, A. Koonan, S. B. Awan, D. Granero, J. Pérez-Calatayud, F. Ballester, TG-43 U1 based dosimetric characterization of model 67-6520 Cs-137 brachytherapy source, *Med. Phys.* 36 (2009) 4711–4719.
- [83] F. J. Casado, S. García-Pareja, E. Cenizo, B. Mateo, C. Bodineau, P. Galán, Dosimetric characterization of an ^{192}Ir brachytherapy source with the Monte Carlo code PENELOPE, *Phys. Med.* 26 (2010) 132–139.
- [84] R. E. P. Taylor, D. W. O. Rogers, EGSnrc Monte Carlo calculated dosimetry parameters for ^{192}Ir and ^{169}Yb brachytherapy sources, *Med. Phys.* 35 (2008) 4933–4944.
- [85] D. Granero, J. Pérez-Calatayud, J. Gimeno, F. Ballester, E. Casal, V. Crispín, R. van der Laarse, Design and evaluation of a HDR skin applicator with flattening filter, *Med. Phys.* 35 (2008) 495–503.
- [86] P. Papagiannis, D. Baltas, D. Granero, J. Pérez-Calatayud, J. Gimeno, F. Ballester, J. L. M. Venselaar, Radiation transmission data for radionuclides and materials relevant to brachytherapy facility shielding, *Med. Phys.* 35 (2008) 4898–4906.
- [87] F. Ballester, D. Granero, J. Pérez-Calatayud, J. L. M. Venselaar, M. J. Rivard, Study of encapsulated ^{170}Tm sources for their potential use in brachytherapy, *Med. Phys.* 37 (2010) 1629–1637.
- [88] M. J. Rivard, J. L. M. Venselaar, L. Beaulieu, The evolution of brachytherapy treatment planning, *Med. Phys.* 36 (2009) 2136–2153.
- [89] M. J. Rivard, L. Beaulieu, F. Mourtada, Enhancements to commissioning techniques and quality assurance of brachytherapy treatment

- planning systems that use model-based dose calculation algorithms, *Med. Phys.* 37 (2010) 2645–2658.
- [90] B. R. Thomadsen, J. F. Williamson, M. J. Rivard, A. S. Meigooni, Anniversary Paper: Past and current issues, and trends in brachytherapy physics, *Med. Phys.* 35 (2008) 4708–4723.
- [91] A. Lechner, M. Blaickner, S. Gianolini, K. Poljanc, H. Aiginger, D. Georg, Targeted radionuclide therapy: theoretical study of the relationship between tumour control probability and tumour radius for a $^{32}\text{P}/^{33}\text{P}$ radionuclide cocktail, *Phys. Med. Biol.* 53 (2008) 1961–1974.
- [92] W. V. Prestwich, J. Nunes, C. S. Kwok, Beta dose point kernels for radionuclides of potential use in radioimmunotherapy, *J. Nucl. Med.* 30 (1989) 1036–1046.
- [93] C. Janicki, J. Seuntjens, Accurate determination of dose-point-kernel functions close to the origin using Monte Carlo simulations, *Med. Phys.* 31 (2004) 814–818.
- [94] J. Lehmann et al., Monte Carlo treatment planning for molecular targeted radiotherapy within the MINERVA system, *Phys. Med. Biol.* 50 (2005) 947–958.
- [95] I. Kawrakow, Accurate condensed history Monte Carlo simulation of electron transport. I. EGSnrc, the new EGS4 version, *Med. Phys.* 27 (2000) 485–498.
- [96] I. Kawrakow, E. Mainegra-Hing, D. W. O. Rogers, F. Tessier, B. R. B. Walters, The EGSnrc Code System: Monte Carlo Simulation of Electron and Photon Transport, Technical Report PIRS-701, National Research Council of Canada, Ottawa, Ontario, 2010.
- [97] H. Hirayama, Y. Namito, A. F. Bielajew, S. J. Wilderman, W. R. Nelson, The EGS5 Code System, SLAC-R-730, 2005.
- [98] J. F. Briesmeister, MCNPTM – General Monte Carlo N-Particle Transport Code, Version 4C, Technical Report LA-13709-M, Los Alamos National Laboratory, Los Alamos, NM, 2000.
- [99] X-5 Monte Carlo Team, MCNP – A General Monte Carlo N-Particle Transport Code, Version 5, Volume I: Overview and Theory, 2003.

- [100] J. Sempau, E. Acosta, J. Baró, J. M. Fernández-Varea, F. Salvat, An algorithm for Monte Carlo simulation of coupled electron–photon transport, *Nucl. Instr. and Meth. B* 132 (1997) 377–390.
- [101] J. A. Halbleib, R. P. Kensek, G. D. Valdez, S. M. Seltzer, M. J. Berger, ITS: The Integrated TIGER Series of Electron/Photon Transport Codes – Version 3.0, *IEEE Trans. Nucl. Sci.* 39 (1992) 1025–1030.
- [102] Geant4 Collaboration, Geant4 Physics Reference Manual, Geant4 9.3 edition, 2009. Available at <http://geant4.web.cern.ch/geant4/UserDocumentation/UsersGuides/PhysicsReferenceManual/fo/PhysicsReferenceManual.pdf>.
- [103] ICRU (International Commission on Radiation Units and Measurements), ICRU Report 78: Prescribing, Recording, and Reporting Proton-Beam Therapy, *J. ICRU* 7, No. 2, Oxford University Press, Oxford, 2007.
- [104] I. Gudowska, N. Sobolevsky, P. Andreo, D. Belkic, A. Brahme, Ion beam transport in tissue-like media using the Monte Carlo code SHIELD-HIT, *Phys. Med. Biol.* 49 (2004) 1933–1958.
- [105] G. Ciangaru, J. C. Polf, M. Bues, A. R. Smith, Benchmarking analytical calculations of proton doses in heterogeneous matter, *Med. Phys.* 32 (2005) 3511–3522.
- [106] D. Pflugfelder, J. J. Wilkens, H. Szymanowski, U. Oelfke, Quantifying lateral tissue heterogeneities in hadron therapy, *Med. Phys.* 34 (2007) 1506–1513.
- [107] M. Soukup, M. Alber, Influence of dose engine accuracy on the optimum dose distribution in intensity-modulated proton therapy treatment plans, *Phys. Med. Biol.* 52 (2007) 725–740.
- [108] H. Paganetti, Monte Carlo calculations for absolute dosimetry to determine machine outputs for proton therapy fields, *Phys. Med. Biol.* 51 (2006) 2801–2812.
- [109] J. Hérault, N. Iborra, B. Serrano, P. Chauvel, Spread-out Bragg peak and monitor units calculation with the Monte Carlo Code MCNPX, *Med. Phys.* 34 (2007) 680–688.
- [110] J. Fan, W. Luo, E. Fourkal, T. Lin, J. Li, I. Veltchev, C.-M. Ma, Shielding design for a laser-accelerated proton therapy system, *Phys. Med. Biol.* 52 (2007) 3913–3930.

- [111] Y. Zheng, W. Newhauser, E. Klein, D. Low, Monte Carlo simulation of the neutron spectral fluence and dose equivalent for use in shielding a proton therapy vault, *Phys. Med. Biol.* 54 (2009) 6943–6957.
- [112] U. Titt, Y. Zheng, O. N. Vassiliev, W. D. Newhauser, Monte Carlo investigation of collimator scatter of proton-therapy beams produced using the passive scattering method, *Phys. Med. Biol.* 53 (2008) 487–504.
- [113] P. Kimstrand, E. Traneus, A. Ahnesjö, N. Tilly, Parametrization and application of scatter kernels for modelling scanned proton beam collimator scatter dose, *Phys. Med. Biol.* 53 (2008) 3405–3429.
- [114] C. Zacharatou Jarlskog, C. Lee, W. E. Bolch, X. G. Xu, H. Paganetti, Assessment of organ-specific neutron equivalent doses in proton therapy using computational whole-body age-dependent voxel phantoms, *Phys. Med. Biol.* 53 (2008) 693–717.
- [115] P. J. Taddei, D. Mirkovic, J. D. Fontenot, A. Giebeler, Y. Zheng, D. Kronguth, R. Mohan, W. D. Newhauser, Stray radiation dose and second cancer risk for a pediatric patient receiving craniospinal irradiation with proton beams, *Phys. Med. Biol.* 54 (2009) 2259–2275.
- [116] W. D. Newhauser et al., The risk of developing a second cancer after receiving craniospinal proton irradiation, *Phys. Med. Biol.* 54 (2009) 2277–2291.
- [117] J. C. Polf, S. Peterson, G. Ciangaru, M. Gillin, S. Beddar, Prompt gamma-ray emission from biological tissues during proton irradiation: a preliminary study, *Phys. Med. Biol.* 54 (2009) 731–743.
- [118] K. Parodi, A. Ferrari, F. Sommerer, H. Paganetti, Clinical CT-based calculations of dose and positron emitter distributions in proton therapy using the FLUKA Monte Carlo code, *Phys. Med. Biol.* 52 (2007) 3369–3387.
- [119] M. Moteabbed, S. Espana, H. Paganetti, Monte Carlo patient study on the comparison of prompt gamma and PET imaging for range verification in proton therapy, *Phys. Med. Biol.* 56 (2011) 1063–1082.
- [120] M. C. Harvey, J. C. Polf, A. R. Smith, R. Mohan, Feasibility studies of a passive scatter proton therapy nozzle without a range modulator wheel, *Med. Phys.* 35 (2008) 2243–2252.

- [121] M. Bues, W. D. Newhauser, U. Titt, A. R. Smith, Therapeutic step and shoot proton beam spot-scanning with a multi-leaf collimator: a Monte Carlo study, *Rad. Prot. Dos.* 115 (2005) 164–169.
- [122] D. J. Brenner, C. D. Elliston, E. J. Hall, H. Paganetti, Reduction of the secondary neutron dose in passively scattered proton radiotherapy, using an optimized pre-collimator/collimator, *Phys. Med. Biol.* 54 (2009) 6065–6078.
- [123] H. Paganetti, H. Jian, S.-Y. Lee, H. M. Kooy, Accurate Monte Carlo simulations for nozzle design, commissioning and quality assurance for a proton radiation therapy facility, *Med. Phys.* 31 (2004) 2107–2118.
- [124] W. D. Newhauser, N. Koch, S. Hummel, M. Ziegler, U. Titt, Monte Carlo simulations of a nozzle for the treatment of ocular tumours with high-energy proton beams, *Phys. Med. Biol.* 50 (2005) 5229–5249.
- [125] W. D. Newhauser, J. Fontenot, Y. Zheng, J. Polf, U. Titt, N. Koch, X. Zhang, R. Mohan, Monte Carlo simulations for configuring and testing an analytical proton dose-calculation algorithm, *Phys. Med. Biol.* 52 (2007) 4569–4584.
- [126] I. Pshenichnov, I. Mishustin, W. Greiner, Distributions of positron-emitting nuclei in proton and carbon-ion therapy studied with GEANT4, *Phys. Med. Biol.* 51 (2006) 6099–6112.
- [127] I. Pshenichnov, A. Larionov, I. Mishustin, W. Greiner, PET monitoring of cancer therapy with ^3He and ^{12}C beams: a study with the GEANT4 toolkit, *Phys. Med. Biol.* 52 (2007) 7295–7312.
- [128] F. Sommerer, F. Cerutti, K. Parodi, A. Ferrari, W. Enghardt, H. Aiginer, In-beam PET monitoring of mono-energetic ^{16}O and ^{12}C beams: experiments and FLUKA simulations for homogeneous targets, *Phys. Med. Biol.* 54 (2009) 3979–3996.
- [129] O. Geithner, P. Andreo, N. Sobolevsky, G. Hartmann, O. Jäkel, Calculation of stopping power ratios for carbon ion dosimetry, *Phys. Med. Biol.* 51 (2006) 2279–2292.
- [130] H. Paul, O. Geithner, O. Jäkel, The ratio of stopping powers of water and air for dosimetry applications in tumor therapy, *Nucl. Instr. and Meth. B* 256 (2007) 561–564.

- [131] H. Paul, O. Geithner, O. Jäkel, The Influence of Stopping Powers upon Dosimetry for Radiation Therapy with Energetic Ions, *Adv. Quantum Chem.* 52 (2007) 289–306.
- [132] K. Henkner, N. Bassler, N. Sobolevsky, O. Jäkel, Monte Carlo simulations on the water-to-air stopping power ratio for carbon ion dosimetry, *Med. Phys.* 36 (2009) 1230–1235.
- [133] H. Nose, Y. Kase, N. Matsufuji, T. Kanai, Field size effect of radiation quality in carbon therapy using passive method, *Med. Phys.* 36 (2009) 870–875.
- [134] Y. Kase, N. Kanematsu, T. Kanai, N. Matsufuji, Biological dose calculation with Monte Carlo physics simulation for heavy-ion radiotherapy, *Phys. Med. Biol.* 51 (2006) N467–N475.
- [135] T. Frisson, N. Zahra, P. Lautesse, D. Sarrut, Monte-Carlo based prediction of radiochromic film response for hadrontherapy dosimetry, *Nucl. Instr. and Meth. A* 606 (2009) 749–754.
- [136] C. L. Hartmann Siantar, W. P. Chandler, J. A. Rathkopf, M. M. Svatos, R. M. White, PEREGRINE: An all-particle Monte Carlo code for radiation therapy, in: *Proc. of Int. Conf. on Mathematics and Computations, Reactor Physics, and Environmental Analyses Portland, Oregon, April 30-May 4, 1995*, pp. 875–865.
- [137] M. Fippel, M. Soukup, A Monte Carlo dose calculation algorithm for proton therapy, *Med. Phys.* 31 (2004) 2263–2273.
- [138] J. Karg, S. Speer, M. Schmidt, R. Mueller, The Monte Carlo code MCPTV - Monte Carlo dose calculation in radiation therapy with carbon ions, *Phys. Med. Biol.* 55 (2010) 3917–3926.
- [139] A. Fassò, A. Ferrari, J. Ranft, P. R. Sala, FLUKA: a multi-particle transport code, CERN-2005-10 and INFN/TC-05/11 and SLAC-R-773, 2005.
- [140] G. Battistoni, F. Cerutti, A. Fassò, A. Ferrari, S. Muraro, J. Ranft, S. Roesler, P. R. Sala, The FLUKA code: description and benchmarking, in: M. Albrow, R. Raja (Eds.), *Proceedings of the Hadronic Shower Simulation Workshop 2006*, volume 896, pp. 31–49.
- [141] H. G. Hughes, K. J. Adams, M. B. Chadwick, J. C. Comly, S. C. Frankle, J. S. Hendricks, R. C. Little, R. E. Prael, L. S. Waters, P. G.

- Young, MCNPXTM – The LAHETTM/MCNPTM code merger, in: Proceedings of the 3rd Workshop on Simulating Accelerator Radiation Environments (SARE 3), Tsukuba, Japan, pp. 44–51.
- [142] H. Iwase, K. Niita, T. Nakamura, Development of general-purpose particle and heavy ion transport Monte Carlo code, *Nucl. Sci. Tech.* 39 (2002) 1142–1151.
- [143] K. Niita, T. Sato, H. Iwase, H. Nose, H. Nakashima, L. Sihver, PHITS – a particle and heavy ion transport code system, *Radiat. Meas.* 41 (2006) 1080–1090.
- [144] L. Sihver, T. Sato, K. Gustafsson, D. Mancusi, H. Iwase, K. Niita, H. Nakashima, Y. Sakamoto, Y. Iwamoto, N. Matsuda, An update about recent developments of the PHITS code, *Adv. Space Res.* 45 (2010) 892–899.
- [145] A. V. Dementyev, N. M. Sobolevsky, SHIELD – universal Monte Carlo hadron transport code: scope and applications, *Radiat. Meas.* 30 (1999) 553–557.
- [146] J. S. Hendricks, G. W. McKinney, M. L. Fensin, M. R. James, R. C. Johns, J. W. Durkee, J. P. Finch, D. B. Pelowitz, L. S. Waters, M. W. Johnson, MCNPX 2.6.0 Extensions, Technical Report LA-UR-08-2216, Los Alamos National Laboratory, Los Alamos, NM, 2008.
- [147] V. N. Ivanchenko, O. Kadri, M. Maire, L. Urban, Geant4 models for simulation of multiple scattering, *J. Phys.: Conf. Ser.* 219 (2010) 032045.
- [148] L. Urbán, Multiple scattering model in GEANT4, CERN-OPEN-2002-070, 2002.
- [149] L. Urbán, A model for multiple scattering in Geant4, CERN-OPEN-2006-077, 2006.
- [150] E. Poon, F. Verhaegen, Accuracy of the photon and electron physics in GEANT4 for radiotherapy applications, *Med. Phys.* 32 (2005) 1696–1711.
- [151] E. Poon, J. Seuntjens, F. Verhaegen, Consistency test of the electron transport algorithm in the GEANT4 Monte Carlo code, *Phys. Med. Biol.* 50 (2005) 681–694.

- [152] L. Maigne, Y. Perrot, D. R. Schaart, D. Donnarieix, V. Breton, Comparison of GATE/GEANT4 with EGSnrc and MCNP for electron dose calculations at energies between 15 keV and 20 MeV, *Phys. Med. Biol.* 56 (2011) 811–827.
- [153] S. Elles, V. N. Ivanchenko, M. Maire, L. Urban, Geant4 and Fano cavity test: where are we?, *J. Phys.: Conf. Ser.* 102 (2008) 012009.
- [154] H. Burkhardt, V. M. Grichine, P. Gumplinger, V. N. Ivanchenko, R. P. Kokoulin, M. Maire, L. Urban, Geant4 standard electromagnetic package for HEP applications, in: *IEEE Nuclear Science Symposium Conference Record*, Rome, Italy, 2004, pp. 1907–1910.
- [155] S. Chauvie, G. Depaola, V. Ivanchenko, F. Longo, P. Nieminen, M. Pia, Geant4 low energy electromagnetic physics, in: *Proceedings of Computing in High Energy and Nuclear Physics*, Beijing, China, 2001, pp. 337–340.
- [156] S. Chauvie et al., Geant4 low energy electromagnetic physics, in: *IEEE Nuclear Science Symposium Conference Record*, Rome, Italy, 2004, pp. 1881–1885.
- [157] O. Kadri, V. Ivanchenko, F. Gharbi, A. Trabelsi, Incorporation of the Goudsmit-Saunderson electron transport theory in the Geant4 Monte Carlo code, *Nucl. Instr. and Meth. B* 267 (2009) 3624–3632.
- [158] J. Apostolakis, S. Giani, M. Maire, P. Nieminen, M. G. Pia, L. Urban, Geant4 low energy electromagnetic models for electrons and photons, CERN-OPEN-99-034, 1999.
- [159] S. T. Perkins, D. E. Cullen, S. M. Seltzer, *Tables and Graphs of Electron-Interaction Cross Sections From 10 eV to 100 GeV Derived from the LLNL Evaluated Electron Data Library (EEDL), Z = 1–100*, Lawrence Livermore National Laboratory, Livermore, CA, Rep. UCRL-50400, vol. 31, 1991.
- [160] D. Cullen, J. H. Hubbell, L. Kissel, EPDL97: the Evaluated Photon Data Library, ‘97 Version, Rep. UCRL-50400, vol. 6, 1997.
- [161] K. Lassila-Perini, L. Urbán, Energy loss in thin layers in GEANT, *Nucl. Instr. and Meth. A* 362 (1995) 416–422.
- [162] S. Guatelli, A. Mantero, B. Mascialino, P. Nieminen, M. G. Pia, Geant4 atomic relaxation, *IEEE Trans. Nucl. Sci.* 54 (2007) 585–593.

- [163] S. T. Perkins, D. E. Cullen, M. H. Chen, J. H. Hubbell, J. Rathkopf, J. Scofield, Tables and Graphs of Atomic Subshell and Relaxation Data Derived from the LLNL Evaluated Atomic Data Library (EADL), $Z = 1-100$, Rep. UCRL-50400, vol. 30, 1997.
- [164] K. Amako et al., Comparison of Geant4 Electromagnetic Physics Models Against the NIST Reference Data, *IEEE Trans. Nucl. Sci.* 52 (2005) 910–918.
- [165] G. A. P. Cirrone, G. Cuttone, F. Di Rosa, L. Pandola, F. Romano, Q. Zhang, Validation of the Geant4 electromagnetic photon cross-sections for elements and compounds, *Nucl. Instr. and Meth. A* 618 (2010) 315–322.
- [166] A. V. Bagulya, M. S. Vladimirov, V. N. Ivanchenko, N. I. Starkov, Heavy-particle energy loss simulation using the Geant4 toolkit, *Bulletin of the Lebedev Physics Institute* 36 (2009) 127–134.
- [167] V. Ivanchenko, S. Giani, M. G. Pia, L. Urban, P. Nieminen, G. Mancinelli, Geant4 simulation of energy losses of ions, CERN-OPEN-99-300 and INFN/AE-99/21, 1999.
- [168] V. Ivanchenko, S. Giani, M. G. Pia, L. Urban, P. Nieminen, G. Mancinelli, Geant4 simulation of energy losses of slow hadrons, CERN-OPEN-99-121, 1999.
- [169] H. S. Fesefeldt, The simulation of hadronic showers: physics and applications, PITHA-85-02, 1985.
- [170] H. P. Wellisch, D. Axen, Total reaction cross section calculations in proton-nucleus scattering, *Phys. Rev. C* 54 (1996) 1329–1332.
- [171] R. K. Tripathi, F. A. Cucinotta, J. W. Wilson, Universal parameterization of absorption cross sections: Light systems, NASA, Technical paper NASA-TP-1999-209726, 1999. Available at http://ntrs.nasa.gov/archive/nasa/casi.ntrs.nasa.gov/20000004258_1999208078.pdf.
- [172] R. K. Tripathi, F. A. Cucinotta, J. W. Wilson, Accurate universal parameterization of absorption cross sections III - light systems, *Nucl. Instr. and Meth. B* 155 (1999) 349–356.
- [173] R. K. Tripathi, F. A. Cucinotta, J. W. Wilson, Accurate universal parameterization of absorption cross sections, *Nucl. Instr. and Meth. B* 117 (1996) 347–349.

- [174] R. K. Tripathi, F. A. Cucinotta, J. W. Wilson, Universal parameterization of absorption cross sections, NASA, Technical paper NASA-TP-3621, 1997. Available at http://ntrs.nasa.gov/archive/nasa/casi.ntrs.nasa.gov/19970011098_1997015752.pdf.
- [175] W. Shen, B. Wang, J. Feng, W. Zhan, Y. Zhu, E. Feng, Total reaction cross section for heavy-ion collisions and its relation to the neutron excess degree of freedom, *Nucl. Phys. A* 491 (1989) 130.
- [176] S. Kox et al., Trends of total reaction cross sections for heavy ion collisions in the intermediate energy range, *Phys. Rev. C* 35 (1987) 1678–1691.
- [177] L. Sihver, C. H. Tsao, R. Silberberg, T. Kanai, A. F. Barghouty, Total reaction and partial cross section calculations in proton-nucleus ($z_t \leq 26$) and nucleus-nucleus reactions (z_p and $z_t \leq 26$), *Phys. Rev. C* 47 (1993) 1225–1236.
- [178] G. Folger, V. N. Ivanchenko, J. P. Wellisch, The Binary Cascade, *Eur. Phys. J. A* 21 (2004) 407–417.
- [179] A. Heikkinen, N. Stepanov, J. P. Wellisch, Bertini intra-nuclear cascade implementation in geant4, in: Proceedings of CHEP'03, 24–28 March 2003, La Jolla, CA, USA.
- [180] A. Heikkinen, Implementing the Bertini intra-nuclear-cascade in the Geant4 hadronic framework, in: The Monte Carlo Method: Versatility Unbounded in a Dynamic Computing World, Chattanooga, Tennessee, April 17–21, 2005, on CD-ROM, American Nuclear Society, LaGrange Park, IL (2005).
- [181] A. Heikkinen, P. Kaitaniemi, A. Boudard, Implementation of INCL cascade and ABLA evaporation codes in Geant4, *J. Phys.: Conf. Ser.* 119 (2008) 032024.
- [182] T. Koi, New native QMD code in Geant4, in: Nuclear Science Symposium Conference Record, 2008. NSS '08. IEEE.
- [183] E. Fermi, High Energy Nuclear Events, *Prog. Theor. Phys.* 5 (1950) 570–583.
- [184] S. Furihata, Statistical analysis of light fragment production from medium energy proton-induced reactions, *Nucl. Instr. and Meth. B* 171 (2000) 251–258.

- [185] J. P. Bondorf, A. S. Botvina, A. S. Iljinov, I. N. Mishustin, K. Sneppen, Statistical multifragmentation of nuclei, *Phys. Rep.* 257 (1995) 133–221.
- [186] G. J. Lockwood, L. E. Ruggles, G. H. Miller, J. A. Halbleib, Calorimetric Measurement of Electron Energy Deposition in Extended Media - Theory vs Experiment, Technical Report, SAND79-0414 UC-34a, 1987. Available at <http://prod.sandia.gov/techlib/access-control.cgi/1979/790414.pdf>.
- [187] G. J. Lockwood, G. H. Miller, J. A. Halbleib, Absolute measurement of low energy electron deposition profiles in semi-infinite geometries, *IEEE Trans. Nucl. Sci.* 20 (1973) 326–330.
- [188] I. Kawrakow, Cross section improvements for EGSnrc, in: *Engineering in Medicine and Biology Society, 2000. Proceedings of the 22nd Annual International Conference of the IEEE*, volume 3, pp. 1668–1671.
- [189] O. Chibani, X. A. Li, Monte Carlo dose calculations in homogeneous media and at interfaces: A comparison between GEPTS, EGSnrc, MCNP, and measurements, *Med. Phys.* 29 (2002) 835–847.
- [190] I. Jun, Benchmark Study for Energy Deposition by Energetic Electrons in Thick Elemental Slabs: Monte Carlo Results and Experiments, *IEEE Trans. Nucl. Sci.* 50 (2003) 1732–1739.
- [191] J. Sempau, J. M. Fernández-Varea, E. Acosta, F. Salvat, Experimental benchmarks of the Monte Carlo code PENELOPE, *Nucl. Instr. and Meth. B* 207 (2003) 107–123.
- [192] V. N. Ivanchenko (For Geant4 Collaboration), Geant4: physics potential for instrumentation in space and medicine, *Nucl. Instr. and Meth. A* 525 (2004) 402–405.
- [193] J. F. Carrier, L. Archambault, L. Beaulieu, Validation of GEANT4, an object-oriented Monte Carlo toolkit, for simulations in medical physics, *Med. Phys.* 31 (2004) 484–492.
- [194] O. Kadri, V. N. Ivanchenko, F. Gharbi, A. Trabelsi, GEANT4 simulation of electron energy deposition in extended media, *Nucl. Instr. and Meth. B* 258 (2007) 381–387.
- [195] M. J. Berger, J. S. Coursey, M. A. Zucker, J. Chang, ESTAR, stopping-power and range tables for electrons, <http://physics.nist.gov/PhysRefData/Star/Text/ESTAR.html>, accessed July 2008.

- [196] G. H. Miller, G. J. Lockwood, Calorimetric determination of beam energy, *IEEE Trans. Nucl. Sci.* 22 (1975) 1072–1075.
- [197] J. S. Coursey, D. J. Schwab, R. A. Dragoset, Atomic Weights and Isotopic Compositions, version 2.4.1, <http://physics.nist.gov/PhysRefData/>, 2005.
- [198] E. S. M. Ali, D. W. O. Rogers, Benchmarking EGSnrc in the kilovoltage energy range against experimental measurements of charged particle backscatter coefficients, *Phys. Med. Biol.* 53 (2008) 1527–1543.
- [199] F. Verhaegen, R. Symonds-Taylor, H. H. Liu, A. E. Nahum, Backscatter towards the monitor ion chamber in high-energy photon and electron beams: charge integration versus Monte Carlo simulation, *Phys. Med. Biol.* 45 (2000) 3159–3170.
- [200] J. Pérez-Calatayud, F. Ballester, M. A. Serrano, J. L. Lluch, E. Casal, V. Carmona, Dosimetric characteristics of backscattered electrons in lead, *Phys. Med. Biol.* 45 (2000) 1841–1849.
- [201] F. Verhaegen, Interface perturbation effects in high-energy electron beams, *Phys. Med. Biol.* 48 (2003) 687–705.
- [202] J. C. L. Chow, G. N. Grigorov, Monte Carlo simulation of backscatter from lead for clinical electron beams using EGSnrc, *Med. Phys.* 35 (2008) 1241–1250.
- [203] J. C. L. Chow, A. M. Owrangi, Solid Water as phantom material for dosimetry of electron backscatter using low-energy electron beams: A Monte Carlo evaluation, *Med. Phys.* 36 (2009) 1587–1594.
- [204] J. C. L. Chow, A. M. Owrangi, Depth dependence of electron backscatter: An energy spectral and dosimetry study using Monte Carlo simulation, *Med. Phys.* 36 (2009) 594–601.
- [205] S. H. Cho, W. D. Reece, Monte Carlo calculations of the dose backscatter factor for monoenergetic electrons, *Phys. Med. Biol.* 44 (1999) 13–26.
- [206] S.-W. Lee, W. D. Reece, Dose backscatter factors for selected beta sources as a function of source, calcified plaque and contrast agent using Monte Carlo calculations, *Phys. Med. Biol.* 49 (2004) 583–599.

- [207] A. Martignano, L. Menegotti, A. Valentini, Monte Carlo investigation of breast intraoperative radiation therapy with metal attenuator plates, *Med. Phys.* 34 (2007) 4578–4584.
- [208] T. Oshima, Y. Aoyama, T. Shimozato, M. Sawaki, T. Imai, Y. Ito, Y. Obata, K. Tabushi, An experimental attenuation plate to improve the dose distribution in intraoperative electron beam radiotherapy for breast cancer, *Phys. Med. Biol.* 54 (2009) 3491–3500.
- [209] A. Lechner, M. G. Pia, M. Sudhakar, Validation of Geant4 Low Energy Electromagnetic Processes Against Precision Measurements of Electron Energy Deposition, *IEEE Trans. Nucl. Sci.* 56 (2009) 398–416.
- [210] M. Vilches, S. García-Pareja, R. Guerrero, M. Anguiano, A. M. Lallena, Multiple scattering of 13 and 20 MeV electrons by thin foils: A Monte Carlo study with GEANT, Geant4, and PENELOPE, *Med. Phys.* 36 (2009) 3964–3970.
- [211] B. A. Faddegon, I. Kawrakow, Y. Kubyshev, J. Perl, J. Sempau, L. Urban, The accuracy of EGSnrc, Geant4 and PENELOPE Monte Carlo systems for the simulation of electron scatter in external beam radiotherapy, *Phys. Med. Biol.* 54 (2009) 6151–6163.
- [212] J. W. Martin, J. Yuan, S. A. Hoedl, B. W. Filippone, D. Fong, T. M. Ito, E. Lin, B. Tipton, A. R. Young, Measurement of electron backscattering in the energy range of neutron β decay, *Phys. Rev. C* 68 (2003) 055503–1.
- [213] J. W. Martin, J. Yuan, M. J. Betancourt, B. W. Filippone, S. A. Hoedl, T. M. Ito, B. Plaster, A. R. Young, New measurements and quantitative analysis of electron backscattering in the energy range of neutron β -decay, *Phys. Rev. C* 73 (2006) 015501.
- [214] A. Lechner, M. G. Pia, M. Sudhakar, Validation of Geant4 low energy physics models against electron energy deposition and backscattering data, in: *IEEE Nuclear Science Symposium Conference Record*, Honolulu, HI, 2007, pp. 2001–2007.
- [215] K. Amako et al., Geant4 and its validation, *Nucl. Phys. B (Proc. Suppl)* 150 (2006) 44–49.
- [216] G. J. Lockwood, G. H. Miller, J. A. Halbleib, Electron Energy and Charge Albedos - Calorimetric Measurement vs Monte Carlo Theory, Technical Report, SAND80-1968 UC-34a, 1987. Available

at <http://prod.sandia.gov/techlib/access-control.cgi/1980/801968.pdf>.

- [217] G. J. Lockwood, G. H. Miller, J. A. Halbleib, Simultaneous integral measurement of electron energy and charge albedos, *IEEE Trans. Nucl. Sci.* 22 (1975) 2537–2542.
- [218] T. Tabata, Backscattering of Electrons from 3.2 to 14 MeV, *Phys. Rev.* 162 (1967) 336–347.
- [219] R. Ito, P. Andreo, T. Tabata, Reflection of electrons and photons from solids bombarded by 0.1- to 100-MeV electrons, *Rad. Phys. Chem.* 42 (1993) 761–764.
- [220] T. Tabata, P. Andreo, K. Shinoda, Fractional energies of backscattered electrons and photon yields by electrons, *Rad. Phys. Chem.* 54 (1999) 11–18.
- [221] E. Benedito, J. M. Fernández-Varea, F. Salvat, Mixed simulation of the multiple elastic scattering of electrons and positrons using partial-wave differential cross-sections, *Nucl. Instr. and Meth. B* 174 (2001) 91–110.
- [222] Y. Kirihara, Y. Namito, H. Iwase, H. Hirayama, Monte Carlo simulation of Tabata’s electron backscattering experiments, *Nucl. Instr. and Meth. B* 268 (2010) 2384–2390.
- [223] J. A. Halbleib, W. H. Vandevender, TIGER, A One-Dimensional Multilayer Electron/Photon Monte Carlo Transport Code, *Nucl. Sci. Eng.* 57 (1975) 94–95.
- [224] J. A. Halbleib, T. A. Melhorn, ITS: The Integrated TIGER Series of Coupled Electron/Photon Monte Carlo Transport Codes, Technical Report, SAND84-0573, 1984. Available at <http://prod.sandia.gov/techlib/access-control.cgi/1984/840573.pdf>.
- [225] S. M. Seltzer, M. J. Berger, Bremsstrahlung spectra from electron interactions with screened atomic nuclei and orbital electrons, *Nucl. Instr. and Meth. B* 12 (1985) 95–134.
- [226] S. M. Seltzer, M. J. Berger, Bremsstrahlung energy spectra from electrons with kinetic energy 1 keV–10 GeV incident on screened nuclei and orbital electrons of neutral atoms with $Z = 1$ –100, *At. Data and Nucl. Data Tables* 35 (1986) 345–418.

- [227] M. Krämer, O. Jäkel, T. Haberer, G. Kraft, D. Schardt, U. Weber, Treatment planning for heavy-ion radiotherapy: physical beam model and dose optimization, *Phys. Med. Biol.* 45 (2000) 3299–3317.
- [228] F. Sommerer, K. Parodi, A. Ferrari, K. Poljanc, W. Enghardt, H. Aiginger, Investigating the accuracy of the FLUKA code for transport of therapeutic ion beams in matter, *Phys. Med. Biol.* 51 (2006) 4385–4398.
- [229] I. Pshenichnov, I. Mishustin, W. Greiner, Neutrons from fragmentation of light nuclei in tissue-like media: a study with the GEANT4 toolkit, *Phys. Med. Biol.* 50 (2005) 5493–5507.
- [230] I. Pshenichnov, I. Mishustin, W. Greiner, Comparative study of depth-dose distributions for beams of light and heavy nuclei in tissue-like media, *Nucl. Instr. and Meth. B* 266 (2008) 1094–1098.
- [231] S. Kameoka et al., Dosimetric evaluation of nuclear interaction models in the Geant4 Monte Carlo simulation toolkit for carbon-ion radiotherapy, *Radiol. Phys. Technol.* 1 (2008) 183–187.
- [232] L. Sihver, D. Schardt, T. Kanai, Depth-Dose Distributions of High-Energy Carbon, Oxygen and Neon Beams in Water, *Jpn. J. Med. Phys.* 18 (1998) 1–21.
- [233] E. Haettner, H. Iwase, D. Schardt, Experimental fragmentation studies with ^{12}C therapy beams, *Radiat. Prot. Dosimetry* 122 (2006) 485–487.
- [234] F. Bloch, Zur Bremsung rasch bewegter Teilchen beim Durchgang durch Materie, *Ann. Phys.* 408 (1933) 285–320.
- [235] S. P. Ahlen, Z_1^7 stopping-power formula for fast heavy ions, *Phys. Rev. A* 17 (1978) 1236–1239.
- [236] J. C. Ashley, R. H. Ritchie, W. Brandt, Z_1^3 Effect in the Stopping Power of Matter for Charged Particles, *Phys. Rev. B* 5 (1972) 2393–2397.
- [237] ICRU (International Commission on Radiation Units and Measurements), ICRU Report 49: Stopping Powers and Ranges for Protons and Alpha Particles, Bethesda, MD, 1993.
- [238] J. F. Ziegler, J. P. Biersack, U. Littmark, The Stopping and Range of Ions in Solids, volume 1 of *The Stopping and Range of Ions in Matter*, Pergamon, New York, 1985.

- [239] W. Brandt, M. Kitagawa, Effective stopping-power charges of swift ions in condensed matter, *Phys. Rev. B* 25 (1982) 5631–5637.
- [240] W. M. Yao, Review of particle physics, *J. Phys. G* 33 (2006) 1.
- [241] R. M. Sternheimer, R. F. Peierls, General Expression for the Density Effect for the Ionization Loss of Charged Particles, *Phys. Rev. B* 3 (1971) 3681–3692.
- [242] B. Rossi, *High-Energy Particles*, Prentice-Hall Inc., New York, 1952.
- [243] H. Paul, A. Schinner, Judging the reliability of stopping power tables and programs for heavy ions, *Nucl. Instr. and Meth. B* 2009 (2003) 252–258.
- [244] H. Paul, New developments in stopping power for fast ions, *Nucl. Instr. and Meth. B* 261 (2007) 1176–1179.
- [245] H. Paul, A. Schinner, An empirical approach to the stopping power of solids and gases for ions from ${}^3\text{Li}$ to ${}^{18}\text{Ar}$, *Nucl. Instr. and Meth. B* 179 (2001) 299–315.
- [246] H. Paul, A. Schinner, An empirical approach to the stopping power of solids and gases for ions from ${}^3\text{Li}$ to ${}^{18}\text{Ar}$, Part II, *Nucl. Instr. and Meth. B* 195 (2002) 166–174.
- [247] H. Paul, <http://www.exphys.uni-linz.ac.at/stopping>, accessed Jan 2010.
- [248] J. F. Ziegler, <http://srim.org/>, accessed Jan 2010.
- [249] P. Sigmund, A. Schinner, Binary theory stopping theory for swift heavy ions, *Europ. Phys. J. D* 12 (2000) 425–434.
- [250] P. Sigmund, A. Schinner, Binary theory of electronic stopping, *Nucl. Instr. and Meth. B* 195 (2002) 64–90.
- [251] P. L. Grande, G. Schiwietz, Convolution approximation for the energy loss, ionization probability and straggling of fast ions, *Nucl. Instr. and Meth. B* 267 (2009) 859–863.
- [252] P. L. Grande, G. Schiwietz, Convolution approximation for swift Particles (CasP), version 4.1. Available at http://www.helmholtz-berlin.de/people/gregor-schiwietz/casp_en.html, accessed Jan 2010.

- [253] H. Paul, The mean ionization potential of water, and its connection to the range of energetic carbon ions in water, *Nucl. Instr. and Meth. B* 255 (2007) 435–437.
- [254] P. Andreo, On the clinical spatial resolution achievable with protons and heavier charged particle radiotherapy beams, *Phys. Med. Biol.* 54 (2009) N205–N215.
- [255] H. Paul, A comparison of recent stopping power tables for light and medium-heavy ions with experimental data, and applications to radiotherapy dosimetry, *Nucl. Instr. and Meth. B* 247 (2006) 166–172.
- [256] D. Emfietzoglou, R. Garcia-Molina, I. Kyriakou, I. Abril, H. Nikjoo, A dielectric response study of the electronic stopping power of liquid water for energetic protons and a new I -value for water, *Phys. Med. Biol.* 54 (2009) 3451–3472.
- [257] D. Schardt, P. Steidl, M. Krämer, U. Weber, K. Parodi, S. Brons, Precision Bragg-Curve Measurements for Light-Ion Beams in Water, GSI Scientific Report 2007, GSI-Gesellschaft f. Schwerionenforschung, 2008.
- [258] H. Paul, Some New Results on Stopping Power for Fast Ions, in: F. E. McDaniel, B. L. Doyle (Eds.), *AIP Conference Proceedings*, volume 1099, pp. 251–254.
- [259] L. Sihver, D. Mancusi, Present status and validation of HIBRAC, *Rad. Measur.* 44 (2009) 38–46.
- [260] U. Weber, Volumenkonforme Bestrahlung mit Kohlenstoff-Ionen zur Vorbereitung einer Strahlentherapie, Ph.D. thesis, University of Kassel, 1998.
- [261] H. Geissel, C. Scheidenberger, P. Malzacher, J. Kunzendorf, ATIMA program. Available at <http://www-linux.gsi.de/~weick/atima/>, accessed Jan 2010.
- [262] K. K. Gudima, S. G. Mashnik, V. D. Toneev, Cascade-exiton model of nuclear reactions, *Nucl. Phys. A* (1983) 329–361.
- [263] K. Niita, S. Chiba, T. Maruyama, T. Maruyama, H. Takada, T. Fukahori, Y. Nakahara, A. Iwamoto, Analysis of the (N, xN') reactions by quantum molecular dynamics plus statistical decay model, *Phys. Rev. C* 52 (1995) 2620–2635.

- [264] K. Niita, T. Maruyama, Y. Nara, S. Chiba, A. Iwamoto, Development of JQMD (Jaeri Quantum Molecular Dynamics) Code, Nippon Genshiryoku Kenkyujo JAERI,Data,Code (1999).
- [265] T. Koi, M. Asai, D. H. Wright, K. Niita, Y. Nara, K. Amako, T. Sasaki, Interfacing the JQMD and JAM Nuclear Reaction Codes to Geant4, SLAC-PUB-9978, 2003.
- [266] A. Lechner, M. G. Pia, Effect of Normalization Algorithms on the Analysis of Bragg Peak Profiles, IEEE Trans. Nucl. Sci. 55 (2008) 3544–3549.
- [267] I. Pshenichnov, A. Botvina, I. Mishustin, W. Greiner, Nuclear fragmentation reactions in extended media studied with Geant4 toolkit, Nucl. Instr. and Meth. B 268 (2009) 604–615.
- [268] T. Toshito for the NIRS-HIMAC P152 collaboration, Validation of nuclear reaction models in Geant4 for the purpose of carbon ion radiotherapy, in: Nuclear Science Symposium Conference Record, 2007. NSS '07. IEEE, volume 3, pp. 2078–2080.
- [269] J. Berkowitz, Atomic and molecular photoabsorption: Absolute total cross sections, Academic Press, San Diego, 2002.
- [270] E. Rietzel, D. Schardt, T. Haberer, Range accuracy in carbon ion treatment planning based on CT-calibration with real tissue samples, Radiat. Oncol. 2 (2007) 14–22.

Acknowledgements

First of all, I would like to thank my supervisor at CERN, Dr. Jürgen Knobloch, for his guidance, encouragement and exceptional support throughout the years.

I would like to express my sincere gratitude to my supervisor Prof. Dr. Hannes Aiginger and Dr. Karin Poljanc at the Vienna University of Technology for their advices and much appreciated support throughout my doctoral studies and their kind help in various matters. I am especially thankful for their help in establishing the first contact with CERN.

I am very grateful to Dr. Vladimir Ivanchenko for many discussions and valuable advices concerning Monte Carlo models in Geant4. I am also thankful to many other colleagues in the Geant4 Collaboration for their help and support during my time as collaboration member. Special thanks also to the CERN IT-GS-DMA section for hosting me during my time as a doctoral student.

I also would like to thank Dr. Maria Grazia Pia for her guidance throughout the initial part of my doctoral studies.

I am very grateful for all friendships which have evolved during my time at CERN.

A ma chère Aurélie que je remercie pour son soutien indéfectible à chaque étape de ce travail.

Schlussendlich, möchte ich mich bei meinen Eltern für ihre unermessliche Unterstützung während meines Studiums und meiner Doktorarbeit bedanken. Ohne Euch wäre dies alles nicht möglich gewesen.

Geneva, December 1, 2011.

Curriculum vitae

Lechner Anton
Mankerstrasse 5,
3232 Bischofstetten,
Austria

E-mail: Anton.Lechner@cern.ch

Date of birth: October 24, 1980

Nationality: Austrian

Education

- | | |
|-------------------|---|
| 10/2006 – Present | Vienna University of Technology, Vienna, Austria
Doctoral student in Technical Physics. <ul style="list-style-type: none">• Thesis at CERN, Geneva, Switzerland on the validation of Monte Carlo physics models for radiotherapy applications. |
| 08/2003 – 05/2004 | Umeå University, Umeå, Sweden
Exchange student program. |
| 10/2000 – 06/2006 | Vienna University of Technology, Vienna, Austria
Undergraduate studies in Technical Physics. Final examination passed with distinction. <ul style="list-style-type: none">• Specialization in radiation physics, with focus on simulations and medical applications. |

- Diploma thesis at ARC Seibersdorf research GmbH, Seibersdorf, Austria on Monte Carlo-based dosimetry in Targeted Radionuclide Therapy.

Working experience

- 10/2010 – Present CERN, Geneva, Switzerland
Fellowship with main focus on LHC beam-machine interaction studies based on particle shower calculations.
- 06/2006 – 10/2006 ARC Seibersdorf research GmbH, Seibersdorf, Austria
Health Physics Division
Development of analysis software for simulations.
- 07/2004 – 11/2004 EPCOS AG, Munich, Germany
Surface Acoustic Wave Components, R & D department
Internship in computational physics: development of routines to calculate acoustic bulk waves in surface acoustic wave (SAW) devices.